Rheinland-Pfälzische Technische Universität Kaiserslautern Landau

Vom Fachbereich Mathematik
der Rheinland-Pfälzischen Technischen Universität Kaiserslautern-Landau
zur Verleihung des akademischen Grades
Doktor der Naturwissenschaften (Doctor rerum naturalium, Dr. rer. nat.)
genehmigte Dissertation

Analysis and Modeling of Fiber-based Microstructures

DE-386

Verfasser:in:	Alex Keilmann
Erstgutachterin:	Prof. Dr. Claudia Redenbach
Zweitgutachter:	Dr. Petr Dokladal (HDR)
Abgabedatum:	30.04.2026
Datum der Disputation:	07.07.2026

II

Abstract

A material's physical behavior depends on its microstructure. In a fibrous material, the fiber directions and inter-fiber contacts have a strong influence on physical properties such as heat flow or stiffness. The material's microstructure can be quantified via, e.g., analysis of computed tomography (CT) images. To improve the material's physical behavior regarding such properties of interest, in-silico simulations provide an efficient and sustainable alternative to purely experimental approaches.

In this thesis, I study and develop methods for analysis and modeling of fibrous materials on multiple scales. In particular, I work with multiple materials made from fibers: Sheet molding compounds (SMC), which are commonly used in the automotive industry, a wood fiber insulation material for sustainable buildings, and a nonwoven that is studied for a biomedical application. First, I study the accuracy of estimation methods for fiber directions in CT images as well as registration and image similarity measures for multimodal images. Then, I extend the Altendorf-Jeulin model, an established stochastic geometrical method to simulate interacting fibers, so that one can additionally calculate and increase the inter-fiber contacts. Finally, I fit multiple models to the insulation material and compare their results of physics simulations.

Zusammenfassung

Die Mikrostruktur von Materialien beeinflusst deren physikalisches Verhalten. Bei Materialien aus Fasern haben Faserrichtungen oder Kontakte zwischen Fasern starken Einfluss auf die Steifigkeit oder die Wärmeleitfähigkeit des Materials. Um diese Materialien hinsichtlich ihres Verhaltens zu charakterisieren, werden Mikrostruktureigenschaften bspw. durch Analyse von Computertomographie-Bildern (CT-Bildern) quantifiziert. Die Mikrostruktur kann anhand von Computersimulationen in Bezug auf physikalische Eigenschaften optimiert werden. Dieses Vorgehen stellt eine nachhaltige Alternative zu rein experimentellen Ansätzen dar.

In dieser Arbeit untersuche ich Methoden zur Analyse und Modellierung von Materialien aus Fasern auf zwei Skalen. Insbesondere wende ich sie auf mehrere Materialien an: Sheet Molding Compounds (SMC), welche von hohem Interesse in der Automobilindustrie sind, ein Dämmstoff aus Holzfasern für nachhaltigeres Bauen und ein Vliesstoff für eine biomedizinische Anwendung. Motiviert durch diese Anwendungen untersuche ich die Genauigkeit von Methoden zur Faserrichtungsschätzung aus CT-Bildern. Anschließend vergleiche ich deren Ergebnisse mit denen eines anderen Bildgebungsverfahrens. Hierzu registriere ich die Bilder anhand eines selbst entwickelten Index für Bildähnlichkeit speziell für Richtungsdaten. Zur Simulation von Fasern erweitere ich das Altendorf-Jeulin-Modell, einen etablierten Algorithmus in der stochastischen Geometrie, um interagierende Fasern zu simulieren. Meine Erweiterung erlaubt die Berechnung und Erhöhung der Anzahl an Kontakten zwischen Fasern. Abschließend fitte ich verschiedene Modelle für den Dämmstoff und betrachte, wie sie Ergebnisse der physikalischen Simulation beeinflussen.

Acknowledgements

This work was funded by the German Federal Ministry of Education and Research (Grant Agreement No: 05M22UKA), the German Research Foundation DFG within SPP 2311 (Grant Agreement No: 465242756), and the French-German doctoral college "Mathematische Bildverarbeitung". I thank Markus Kronenberger and Michael Godehardt, Fraunhofer Institute for Industrial Mathematics (ITWM), for their support with the MAVIlib library and access to the ITWM Beehive Cluster. I also thank Stefan Rief and Christian Leithäuser (ITWM) for running simulations of thermal and radiative conductivity as well as stiffness simulations on my fiber models. Further thanks to Akila Kulathilake and Konstantin Hauch (RPTU) for image pre-processing of scaffold images, and to Kai Nikolaus (RPTU) for doing the CT Scans of the TomoScope images in Section 5.1.2.2.

I am deeply grateful to my supervisors Claudia Redenbach and Katja Schladitz for their guidance and training. I gratefully acknowledge François Willot for the opportunity of a research stay at the Center of Mathematical Morphology (CMM) in Fontainebleau, France.

My PhD time was significantly shaped by the work groups I have been associated with. Special thanks to Tin Barišin (ITWM), Antoine Bottenmueller (CMM), Emily Ewers (RPTU), Chiara Fend (RPTU), Thomas Langrognet (CMM), Valentin Penaud–Polge (CMM), and Jelena Zaninović (ITWM).

Contents

Abstract | Zusammenfassung **III**

1 Introduction **1**

2 Preliminaries **3**

2.1 Directional Statistics . . . 3

2.1.1 Coordinate Systems . . . 4

2.1.2 Mean Direction . . . 6

2.1.3 Uniform Distribution . . . 7

2.1.4 Von Mises-Fisher Distribution . . . 8

2.1.5 Angular Central Gaussian Distribution . . . 9

2.2 Stochastic Geometry . . . 12

2.2.1 Random Sets . . . 12

2.2.2 Random Measures and Point Processes . . . 13

2.2.2.1 The Poisson Process . . . 15

2.2.3 The Boolean Model . . . 15

2.2.4 Poisson Line Process . . . 18

3 Analysis of Fiber-Based Microstructures **21**

3.1 Polarization Imaging and Computed Tomography . . . 22

3.2 Fiber Orientation Estimation . . . 25

3.2.1 Structure Tensor . . . 26

3.2.2 Hessian Matrix . . . 27

3.2.3 Maximal Response of Anisotropic Gaussian Filters . . . 27

3.2.4 Experimental Validation Study . . . 28

3.2.4.1 Setup . . . 29
3.2.4.2 Results . . . 30
3.2.5 Application to Sheet Moulding Compounds . . . 32
3.3 Image Similarity Measures for Multimodal Data . . . 35
3.3.1 Image Registration of 2D Orientation Data . . . 35
3.3.2 Comparison of Layerwise Orientation Distributions . . . 37
3.3.3 Results . . . 38
3.4 Discussion . . . 40

4 Modeling Fiber-based Microstructures 45
4.1 Literature Review . . . 45
4.2 Altendorf-Jeulin Model . . . 47
4.2.1 Formalizing the Fiber System . . . 48
4.2.2 Force-biased Packing . . . 50
4.2.3 Extension to Endless Fibers . . . 52
4.3 Fiber Bundles in the Altendorf-Jeulin-Model . . . 53
4.3.1 Bundle Generation . . . 53
4.3.2 Bundle Packing . . . 56
4.3.2.1 Voxelization . . . 58
4.4 Extending the Altendorf-Jeulin Model to Inter-fiber Contact . . . 59
4.4.1 Analytical Description for Fiber Contact . . . 59
4.4.1.1 Algorithmic Notions of Contact and Closeness . . . 60
4.4.2 Contact Force . . . 62
4.4.3 Synopsis of the Contact Packing Scheme . . . 63
4.4.4 Implementational Details . . . 64
4.5 Experimental Validation . . . 66
4.5.1 Experimental Setup . . . 66
4.5.2 Representative Volume Element and Runtime . . . 67
4.5.3 Contact Intensity Achieved Depending on the Interaction Distance . . . 70
4.5.4 Achieved Contact Intensity Compared to Toll's Formula . . . 71

4.5.5 Accuracy Results . . . 76
4.5.6 Sensitivity of the Threshold Parameter t . . . 81
4.6 Discussion and Conclusion . . . 82

5 Applications of Fiber Models 85
5.1 Nonwoven Scaffolds . . . 85
5.1.1 Material & Imaging . . . 86
5.1.2 Image Segmentation . . . 88
5.1.2.1 SkyScan . . . 88
5.1.2.2 TomoScope . . . 88
5.1.3 Local Direction Estimation and Distribution Fit . . . 90
5.1.4 Geometric Fiber Model . . . 93
5.1.5 Discussion and Outlook . . . 94
5.2 Wood-fiber Insulation Boards . . . 95
5.2.1 Estimation of Fiber Length, Single Fiber Thickness, and Fiber Bundle Thickness . . . 95
5.2.2 Geometric Fiber Models . . . 98
5.2.3 Thermal Simulation . . . 99
5.2.4 Discussion . . . 102
5.3 Impact of Model Decisions . . . 103
5.3.1 Model Selection . . . 103
5.3.2 RVE Study . . . 105
5.3.3 Results . . . 107
5.3.4 Discussion . . . 108

6 Conclusion 113

List of Tables 130

List of Figures 138

A Appendix to Section 4.5 139
A.1 Parameter combinations . . . 139

A.2 Fitted Model for the Representative Volume Element 140
A.3 Validation Plots 141

B Appendix to Section 5.1 **147**

C Appendix to Section 5.2 **151**

List of Publications **155**

Academic Curriculum Vitae | Akademischer Lebenslauf **157**

Chapter 1

Introduction

The topic of this thesis is inspired by applications in material science. In this field, fiber-based microstructures are highly relevant as the fibers' shape and arrangement significantly influence the physical behavior of the material. In particular, the orientation of fibers, their inter-fiber contact, and the volume fraction of the fiber system are known to strongly impact physical behavior such as thermal conductivity or mechanical behavior [1]–[4]. Materials of interest are often characterized by analyzing material images of various modalities. Based on the characterization, parametric fiber models can be built. Systematic variation of parameters combined with physical simulations on the models allows for finding improved material compositions. The advantage of such a procedure is that it is often faster, cheaper, and easier to control than purely experimental approaches [5].

In this thesis, we study the analysis of computed tomography (CT) images of fibers and model fibers geometrically as input for physical simulation tools. This work is largely inspired by applications to the following materials:

- Sheet moulding compounds (SMC), which is a fiber-based material that is of high relevance in the automotive industry due to its light weight and customizable behaviour (Chapter 3);
- nonwoven scaffolds in a biomedical application (Chapter 5.1);
- wood-fiber insulation boards, whose insulation behavior we aim to improve as a type of climate action (Chapter 5.2).

The methodological advances of this thesis are divided into advances in image analysis (Chapter 3) and advances in fiber models (Chapter 4). In Chapter 3, we study the performance of methods estimating fiber orientations from CT images in the case of low resolution and low contrast. Subsequently, we compare fiber orientation data of SMC achieved through orientation estimation from CT images on the one hand, and orientation images taken with a polarization camera on the other hand. To compare the results of both image modalities, we develop a novel image similarity measure for orientation data. In Chapter 4, we suggest a method that is able to model fiber bundles, as they occur in wood-fiber insulation boards; further, we successfully develop a fiber model that explicitly models inter-fiber contact and allows to increase the amount of contacts parametrically as to study the influence of the contact in physical simulations accurately.

Turning to applications, we showcase our research on nonwoven scaffolds in Chapter 5.1 to show the pipeline from CT images to synthetic geometry models. Chapter 5.2 presents our research on improving the insulation of wood-fiber insulation boards; this gives an example for a pipeline from data-driven modeling to physical simulation tools, where we systematically vary parameters with the goal of improving the insulation boards' performance. Chapter 5.3 is a comparison of the different fiber models presented in this thesis that are applicable when modeling wood fibers. The comparison criterion is here the influence on physical simulations, namely thermal conductivity and stiffness. With this chapter, we show the relevance and advantages of the developed models above.

For each chapter, we will indicate the publication status of the presented research and, where it is relevant, the contribution of coauthors. For code written in Python or R, we occasionally used the LLM GPT o4-mini [6] to get a first template on reading data, cleaning it, and plotting it nicely. We also used it for better readability after writing the original code. In either case, we verified the code for correctness. The data and code used in this thesis have either been published along with the previous publications or can be provided upon reasonable request. In the next chapter, will we shortly state the mathematical foundations of this thesis.

Chapter 2

Preliminaries

Let $d, k, m, n \in \mathbb{N}$ and ν_d the Lebesgue-measure in $\mathbb{R}^d$ in this chapter. $B_d(x, r)$ describes the ball in $\mathbb{R}^d$ with center $x \in \mathbb{R}^d$ and radius $r > 0$. For $x \in \mathbb{R}^d$ and $A, B \subset \mathbb{R}^d$, we define

- the translation of A by x as

$$x + A = A + x = \{x + a : a \in A\} \tag{2.0.1}$$

- the reflection of A as

$$\check{A} = \{-a : a \in A\} \tag{2.0.2}$$

- the Minkowski-addition $\oplus$ of two sets A, B as

$$A \oplus B = \{a + b : a \in A, b \in B\}, \tag{2.0.3}$$

see Chiu et al. [7]. In this thesis, we will treat angles and inverse trigonometric functions in degrees.

2.1 Directional Statistics

The orientation of fibers in a material has a major influence on the material's physical behavior. Therefore, we are interested in describing it statistically and modeling it stochastically. This section introduces coordinate systems for orientational data. Subsequently, we describe pitfalls of calculating a mean value as well as appropriate

formulae. Finally, we introduce probability distributions on the sphere, namely the uniform distribution, the von Mises-Fisher distribution, and the angular central Gaussian distribution. Each of them will be used for fiber modeling in later sections. For more details, the introductory books by Mardia & Jupp [8] and Fisher et al. [9] provide a comprehensive overview of directional statistics. Pewsey & García-Portugués [10] published a review on recent advances and Mardia [11] describes the historical development of the field. Throughout this thesis, we will use the terms "direction" and "orientation" interchangeably.

2.1.1 Coordinate Systems

In directional statistics, we treat data on the sphere

$$S^p = \{x \in \mathbb{R}^{p+1} : x^T x = 1\}, \quad p \in \mathbb{N}. \tag{2.1.1}$$

For $p = 1$, this refers to circular data, see Fig. 2.1.1, as we will handle in Chapter 3; for $p = 2$, this refers to directions in 3D space as we will handle in Chapter 4 and 5. For fiber orientations, the choice between x and $-x$ is ambiguous. Therefore, it is more meaningful to consider them as axial data, i.e., x and $-x$ encoding the same fiber orientation. So axial data is restricted to

$$S^p_+ = \{x \in \mathbb{R}^{p+1} : x^T x = 1, x_{p+1} \geq 0\}, \tag{2.1.2}$$

the upper hemisphere [11].

Apart from unit vectors in Euclidean space, directional data is often encoded in polar coordinates. For circular data, that is an angle in $(0, 360°)$, which can be calculated from unit vectors as

$$\theta = \begin{cases} \cos^{-1}(x_1), & \text{if } x_2 \geq 0 \\ 360° - \cos^{-1}(x_1), & \text{if } x_2 < 0 \end{cases}, \tag{2.1.3}$$

see Fig. 2.1.1; reversely,

$$x = (\cos(\theta), \sin(\theta))^T. \tag{2.1.4}$$

For a point $x \in S^2$, polar coordinates (θ, ϕ) relative to $(0, 0)$ are described by a colatitude $0° \leq \theta \leq 180°$, so the angle between x and the axis $(0, 0, 1)^T$, and a

longitude $0° \leq \phi < 360°$, the angle between the projection of x onto the x_1-x_2-plane and the axis $(1,0,0)^T$ (anti-clockwise), see Fig. 2.1.1. For axial data, θ takes values in $[0, 90°)$. More specifically, the polar coordinates (θ, ϕ) are transformed to $x \in S^2$ as

$$x = (\sin(\theta)\cos(\phi), \sin(\theta)\sin(\phi), \cos(\theta))^T; \tag{2.1.5}$$

reversely, $x \in S^2$ is transformed into polar coordinates as

$$\theta = \cos^{-1}(x_3), \quad \phi = \begin{cases} \tan^{-1}(\frac{x_2}{x_1}), & \text{for } x_1 \neq 0 \\ 0 & \text{otherwise} \end{cases}. \tag{2.1.6}$$

In pseudocode, we will denote these transformations as PolarToS2 and S2ToPolar, resp.

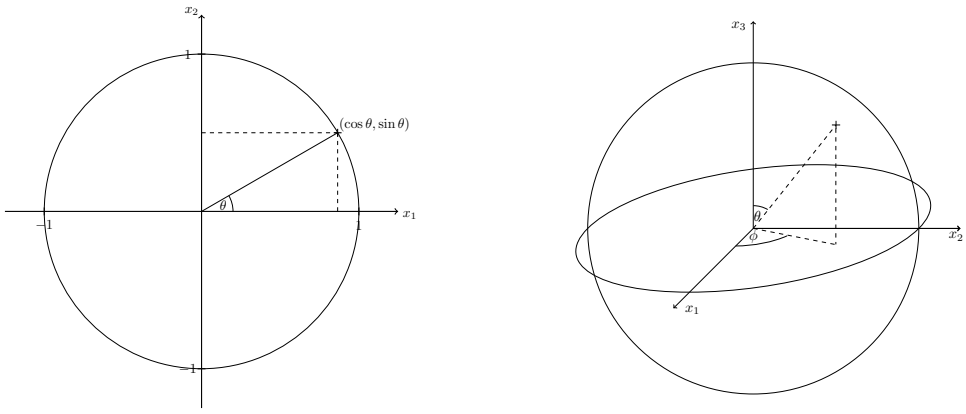

Figure 2.1.1: Sketches of polar coordinates in 2D (left) and 3D (right).

To describe polar coordinates (θ, ϕ) relative to the direction (θ_0, ϕ_0), use the rotation matrix

$$M(\theta_0, \phi_0) := \begin{pmatrix} \cos(\theta_0)\cos(\phi_0) & \cos(\theta_0)\sin(\phi_0) & -\sin(\theta_0) \\ -\sin(\phi_0) & \cos(\phi_0) & 0 \\ \sin(\theta_0)\cos(\phi_0) & \sin(\theta_0)\sin(\phi_0) & \cos(\theta_0) \end{pmatrix}. \tag{2.1.7}$$

Then, the relative polar coordinates (θ', ϕ') are described implicitly by

$$\begin{pmatrix} \sin(\theta')\cos(\phi') \\ \sin(\theta')\sin(\phi') \\ \cos(\theta') \end{pmatrix} = M(\theta_0, \phi_0) \begin{pmatrix} \sin(\theta)\cos(\phi) \\ \sin(\theta)\sin(\phi) \\ \cos(\theta) \end{pmatrix}. \tag{2.1.8}$$

2.1.2 Mean Direction

The mean value of directional data should be calculated carefully. For example, consider the directions $\alpha_1 = 60°$, $\alpha_2 = 30°$, and $\alpha_3 = 330°$ in polar coordinates in 2D. They are depicted in Fig. 2.1.2a together with their arithmetic mean of 130°. Rotating the x_1-axis yields a transformation of the polar coordinates. Let the coordinate system be rotated by 40° as in Fig. 2.1.2b. Then, the same data set has the coordinates $\alpha_1' = 20°, \alpha_2' = 350°$, and $\alpha_3' = 290°$. This yields the arithmetic mean of 220°, which corresponds to 260° in the original coordinate system. When considering a mean direction, however, we require a direction that is consistent under coordinate transformation.

A mean direction which is consistent under rotation of the polar coordinate system is given by the center of mass $(\bar{C}, \bar{S})$ as

$$\bar{C} = \frac{1}{n}\sum_{j=1}^{n}\cos\theta_j, \qquad \bar{S} = \frac{1}{n}\sum_{j=1}^{n}\sin\theta_j \tag{2.1.9}$$

for angles $\theta_j, j = 1, ..., n \in \mathbb{N}$. Then, the mean angle is given by

$$\bar{\theta} = \begin{cases} \arctan(\bar{S}/\bar{C}), & \text{if } \bar{C} \leq 0 \\ \arctan(\bar{S}/\bar{C}) + 180°, & \text{otherwise.} \end{cases} \tag{2.1.10}$$

For our exemplary dataset, such calculation yields 21°, see Fig. 2.1.2c. Alternatively, the polar coordinates can be transformed into unit vectors $x_1, ..., x_n \in S^1$. Then, the mean direction is given by $\bar{x} = \frac{\sum_{i=1}^{n} x_i}{\|\sum_{i=1}^{n} x_i\|}$ if $\|\sum_{i=1}^{n} x_i\| \neq 0$ [8].

For axial data in 2D, similar formulae for the mean direction hold up. Whereas non-axial direction data is periodic regarding 360°, axial data is periodic regarding 180°. To utilize the periodicity of trigonometric functions, we double angles when calculating the center of mass $(\bar{C}_a, \bar{S}_a)$ as

$$\bar{C}_a = \frac{1}{n}\sum_{j=1}^{n}\cos 2\theta_j, \qquad \bar{S}_a = \frac{1}{n}\sum_{j=1}^{n}\sin 2\theta_j \tag{2.1.11}$$

for angles $\theta_j, j = 1, ..., n \in \mathbb{N}$. Then, the mean angle is given by

$$\bar{\theta} = \begin{cases} \frac{1}{2}\arctan(\bar{S}_a/\bar{C}_a), & \text{if } \bar{C}_a \leq 0 \\ \frac{1}{2}\arctan(\bar{S}_a/\bar{C}_a) + 180°, & \text{otherwise,} \end{cases} \tag{2.1.12}$$

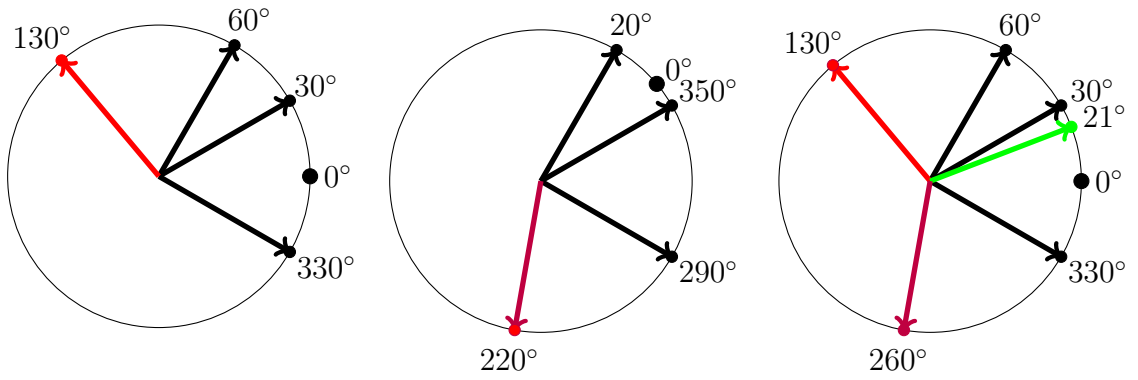

(a) Calculating the arithmetic mean of angles (wrong).

(b) Calculating the arithmetic mean of angles after coordinate rotation (wrong).

(c) Comparison of correctly and wrongly calculated mean directions.

Figure 2.1.2: Illustration of pitfalls when calculating the mean direction.

see [8].

Considering directions in $3D$, the mean direction can analogously be calculated as $\bar{x} = \frac{\sum_{i=1}^{n} x_i}{\| \sum_{i=1}^{n} x_i \|}$ if $\| \sum_{i=1}^{n} x_i \| \neq 0$ for $x_1, ..., x_n \in S^2$. For axial data, the eigendecomposition of the fiber orientation tensor needs to be calculated. For more details, see Fisher et al. [9].

2.1.3 Uniform Distribution

The most basic distribution to be defined on the sphere is the uniform distribution, where each direction is "equally likely to be sampled". It has the density

$$f(\theta) = \frac{1}{2\pi} \tag{2.1.13}$$

on the circle and

$$f(\theta, \phi) = \frac{1}{4\pi} \tag{2.1.14}$$

on the sphere S^2 [8]. Algorithm 1 provides pseudo-code on how to generate pseudo-random numbers/directions following the uniform distribution. Here and in the following, $r \sim \text{Distr}$ indicates that a number r is generated from a pseudo-random number generator following the distribution Distr. $\text{Unif}(a, b), a, b \in \mathbb{R}$ denotes the real-valued uniform distribution on the interval $[a, b]$.

Algorithm 1 Pseudo-random Directions in 3D Polar Coordinates Following the Uniform Distribution

$\theta \sim \text{Unif}(0, 360)$

$r \sim \text{Unif}(-1, 1)$

$\phi = \arccos(r)$

return (θ, ϕ)

2.1.4 Von Mises-Fisher Distribution

The von Mises-Fisher distribution $\text{vMF}(\mu, \kappa)$ is an exponential directional distribution on S^p. The direction $\mu \in S^p$ indicates the mean direction, whereas κ is a concentration parameter. The vMF-distribution has the density

$$f(x) = c_p(\kappa) \exp(\kappa \mu^T x), \quad x, \mu \in S^2, \kappa \geq 0 \tag{2.1.15}$$

with normalization constant

$$c_p(\kappa) = \frac{\left(\frac{\kappa}{2}\right)^{\frac{p-1}{2}}}{(2\pi)^{\frac{p+1}{2}} I_{\frac{p-1}{2}}(\kappa)}. \tag{2.1.16}$$

and $I_{\frac{p-1}{2}}$ the modified Bessel function of the first kind and order $\frac{p-1}{2}$. Fig. 2.1.3 shows density plots for different κ on S^2. For $\kappa = 0$, the von Mises-Fisher distribution is a uniform distribution. For higher κ, the fibers are more concentrated around the direction μ. Moreover, one can observe that the vMF distribution is symmetric around μ. Algorithm 2 describes the simulation of a vMF distribution in S^2 [8], [10].

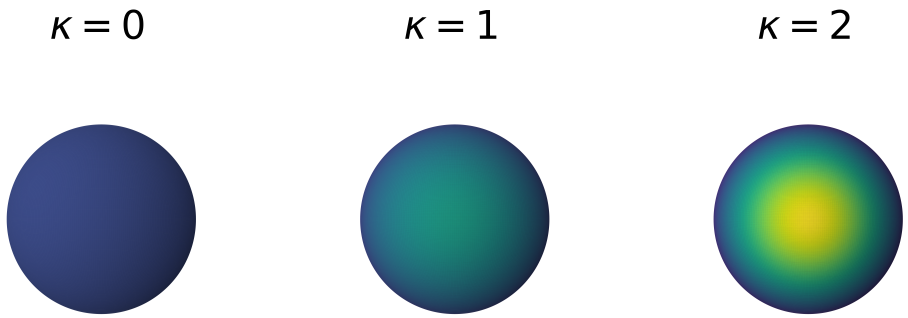

Figure 2.1.3: Density plots for the von Mises-Fisher distribution on the sphere S^2 for varying κ. The mean μ (if existent) is directed out of the paper plane.

Algorithm 2 Pseudo-random Directions in 3D Polar Coordinates Following the von Mises-Fisher Distribution

Require: $\mu \in S^2, \kappa > 0$

$\phi \sim \text{Unif}(0, 360)$

$r_1 \sim \text{Unif}(0, 1)$

$r_2 = -\log(r_1(1 - \exp(-2\kappa)) + \exp(-2\kappa))$

$\theta = 2 \arcsin\left(\sqrt{\frac{r_2}{2\kappa}}\right)$

$x = \text{PolarToS2}(\theta, \phi)$

$x_\mu = M(\text{S2ToPolar}(\mu))x$

return $\text{S2ToPolar}(x_\mu)$

The von Mises-Fisher distribution can also be made multivariate [10]. Usually, this is defined on the torus or cylinder. Yet, for the curvature of fibers, its multivariate version on the sphere is of interest [12]. The multivariate von Mises-Fisher $\text{mvMF}(\mu', \kappa_1, \mu'', \kappa_2)$ is defined as the univariate von Mises-Fisher distribution with $\kappa = |\kappa_1\mu' + \kappa_2\mu''|$ and $\mu = \frac{\kappa_1\mu' + \kappa_2\mu''}{\kappa}$. Table 2.1.1 presents its density for varying κ_1, κ_2.

2.1.5 Angular Central Gaussian Distribution

A common distribution to model axial data is the angular central Gaussian (ACG) distribution. The density of this distribution model on the unit sphere in $\mathbb{R}^3$ is given by

$$f_A(x) = \frac{1}{4\pi|\det A|^{\frac{1}{2}}}(x^T A^{-1} x)^{-\frac{3}{2}}, \quad x \in \mathbb{S}^2. \tag{2.1.17}$$

A is always a symmetric positive-definite matrix. The ACG distribution can be interpreted as the distribution of the direction of a $\mathcal{N}_3(0, A)$-distributed random vector or, alternatively, as the distribution of a random point uniformly distributed on the ellipsoid $x : x^T A^{-1} x = 1$. Therefore, it can be simulated as shown in Algorithm 3. The maximum likelihood estimate for the ACG parameter matrix A can be calculated using the fixed-point algorithm proposed by Tyler [13].

A special case of the ACG distribution is the Schladitz distribution [14] with anisotropy parameter $\beta > 0$. Its density $f_\beta(x) = f_A(x)$ with $A = \text{diag}(1, 1, \beta^{-2})$

Table 2.1.1: The density of the multivariate von Mises-Fisher distribution with concentration parameters κ_1, κ_2 and $\mu' = (1,0,0)^T$ and $\mu'' = (0,1,0)^T$. For each plot, yellow indicates the maximum of the density. Hence, the plots do not use the same color scale for the sake of visibility.

	$\kappa_1 = 1$	$\kappa_1 = 10$	$\kappa_1 = 100$
$\kappa_2 = 1$	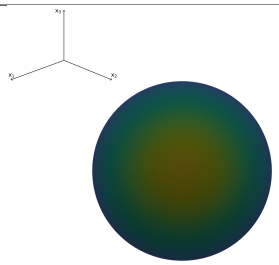	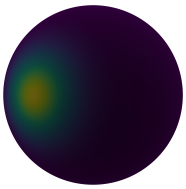	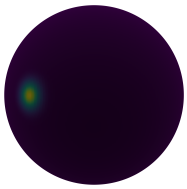
$\kappa_2 = 10$	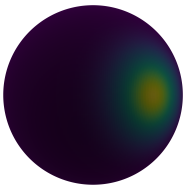	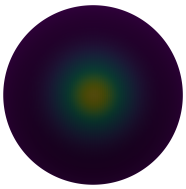	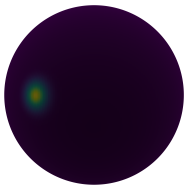
$\kappa_2 = 100$	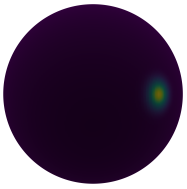	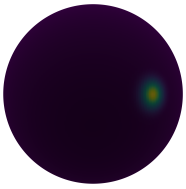	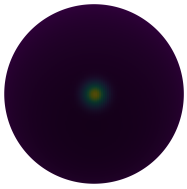

Its density w.r.t. polar coordinates (θ, ϕ) is given by

$$f_\beta(\theta,\phi) = \frac{1}{4\pi} \frac{\beta \sin\theta}{(1+(\beta^2-1)\cos^2\theta)^{\frac{3}{2}}}, \quad \theta \in [0,\pi), \phi \in [0,2\pi). \tag{2.1.18}$$

For β close to 0, this distribution generates directions that are mostly aligned with the z-direction; $\beta = 1$ corresponds to the uniform distribution on the unit sphere; $\beta \gg 1$ results in girdle distributions with directions that are concentrated around

Algorithm 3 Pseudo-random Directions in 3D Polar Coordinates Following the ACG Distribution

Require: $A \in \mathbb{R}^3$ symmetric positive definite

$r \sim \mathcal{N}(0, I_3)$

$L = \text{chol}(A)$ Cholesky-decomposition $A = LL^T$

$r \leftarrow Lr$

return S2ToPolar$\left(\frac{r}{\|r\|}\right)$

the equator, see Fig. 2.1.4.

Pseudo-random directions following the Schladitz distribution can be sampled more simply than with a Cholesky decomposition, as shown in Algorithm 4. The Schladitz distribution is defined such that its mean direction is aligned with the z-axis; for a different mean direction, its samples can be rotated, see Section 2.1.1. Franke et al. [15] propose to estimate the parameter β using a maximum-likelihood estimator.

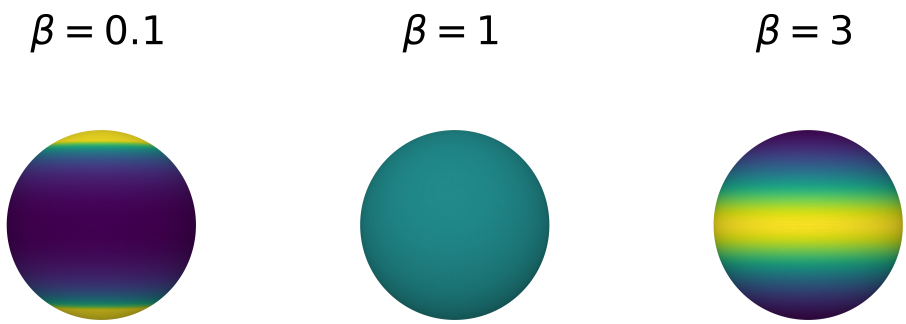

Figure 2.1.4: Plot of the Schladitz-distribution for varying parameters β.

Algorithm 4 Pseudo-random Directions in 3D Polar Coordinates Following the Schladitz Distribution

Require: $\beta > 0$

$r \sim \text{Unif}(-1, 1)$

$\xi = \frac{r^2}{\sqrt{r^2 - r^2\beta^2 + \beta^2}}$

$\theta = \arccos(\xi)$

$\phi \sim \text{Unif}(0, 360)$

return (θ, ϕ)

2.2 Stochastic Geometry

Stochastic geometry studies random variables that are set-valued or measure-valued in order to answer geometric probability questions. In this section, we introduce its basic concepts: random sets and random measures. Based on these concepts, we define the Boolean model and the Poisson line process, the most basic models for a fiber system. We follow the books by Schneider & Weil [16] and Ohser & Schladitz [17] very closely (up to citation). We omit proofs on any of the stated properties (including well-definedness) as they are given in [16].

In the following, we are working on a locally compact topological space E with countable base. One example for E is $E = \mathbb{R}^3$, the space where we model fibers later on.

2.2.1 Random Sets

As random sets are characterized by their intersections with subsets of E, we introduce the following notation.

Definition 2.2.1 Let $\mathcal{C}, \mathcal{F}$, and $\mathcal{G}$ be the systems of compact, closed, and open subsets of E, respectively, each including the empty set $\emptyset$. For sets $A, A_1, ..., A_m \subset E$, we define

$$\mathcal{F}^A = \{F \in \mathcal{F} : F \cap A = \emptyset\} \tag{2.2.1}$$

$$\mathcal{F}_A = \{F \in \mathcal{F} : F \cap A \neq \emptyset\} \tag{2.2.2}$$

$$\mathcal{F}^A_{A_1,...,A_m} = \mathcal{F}^A \cap \mathcal{F}_{A_1} \cap ... \cap \mathcal{F}_{A_m}, \quad m = 0, 1, ..., \tag{2.2.3}$$

where we put $\mathcal{F}^A_{A_1,\dots,A_m} = \mathcal{F}^A$ for $m = 0$.

We equip $\mathcal{F}$ with the following topology.

Definition 2.2.2 (Topology of Closed Convergence)

The *topology of closed convergence* (also known as *Fell topology* or *hit-and-miss topology*) on $\mathcal{F}$ is the topology generated by

$$\{\mathcal{F}^C : C \in \mathcal{C}\} \cup \{\mathcal{F}_G : G \in \mathcal{G}\}. \tag{2.2.4}$$

The corresponding σ-algebra $\mathcal{B}(\mathcal{F})$ of Borel sets of $\mathcal{F}$ is generated by either of the systems

$$\{\mathcal{F}^C : C \in \mathcal{C}\}, \{\mathcal{F}_C : C \in \mathcal{C}\}, \{\mathcal{F}^G : G \in \mathcal{G}\}, \text{ or } \{\mathcal{F}_G : G \in \mathcal{G}\}. \tag{2.2.5}$$

Now, we have all the tools ready to define a random closed set.

Definition 2.2.3 (Random Closed Set) Let $(\Omega, \mathcal{A}, \mathbb{P})$ a probability space. A *random closed set* in E is an $\mathcal{F}$-valued random variable, i.e., an $(\mathcal{A}, \mathcal{B}(\mathcal{F}))$-measurable map $\Xi : \Omega \to \mathcal{F}$.

2.2.2 Random Measures and Point Processes

We define random measures based on a measurable space of measures.

Definition 2.2.4 Let $M = M(E)$ be the set of all Borel measures η on E which are locally finite, that is, satisfy $\eta(C) < \infty$ for all $C \in \mathcal{C}$. Let $\mathcal{M}$ be the smallest σ-algebra such that $\eta \mapsto \eta(C), C \in \mathcal{C}$ is measurable.

Definition 2.2.5 (Random Measure)

Let $(\Omega, \mathcal{A}, \mathbb{P})$ a probability space. A *random measure* η on E is an M-valued random variable, i.e., a measurable map from $(\Omega, A, \mathbb{P})$ into the measurable space $(M, \mathcal{M})$ of locally finite measures on E.

Definition 2.2.6 (Stationarity)

A random measure η as defined above is *stationary* if η and $\eta + x$ have the same distribution for all $x \in \mathbb{R}^d$.

Analogously to the expected value in real-valued random variables, we use the intensity measure for random measures.

Definition 2.2.7 (Intensity Measure)

The intensity measure of the random measure η on E is defined by

$$\Lambda(A) = \mathbb{E}\eta(A), \quad A \in \mathcal{B}. \tag{2.2.6}$$

If η is stationary, its intensity measure Λ is invariant under translations. If Λ is locally finite, then

$$\Lambda = \lambda\nu_d, \quad \lambda \in [0, \infty), \tag{2.2.7}$$

where λ is called the *intensity* of η.

A special case of random measures are those on "discrete values", meaning, based on counting measures. These are called point processes.

Definition 2.2.8 (Counting Measures)

A *counting measure* on E is a measure $\phi \in M$ with $\phi(A) \in \mathbb{N}_0 \cup \{\infty\}$ for all $A \in \mathcal{B}$. Let N be the set of all (locally finite) counting measures on E. By $\mathcal{N}$ we then denote the trace σ-algebra of $\mathcal{M}$ on N.

Definition 2.2.9 (Point Process)

A random measure ϕ which is almost surely concentrated on N is called a *point process* (in E). ϕ is called *simple* if $\phi(\{x\}) \leq 1$ for all $x \in E$ almost surely.

A simple point process ϕ can be identified with its support $\text{supp}(\phi)$, which is a random set, see Schneider & Weil [16]. Hence, we can use $\phi(\{x\}) = 1$ and $x \in \phi$ for $x \in E$ synonymously. This also justifies the name point process for random counting measures.

2.2.2.1 The Poisson Process

The most basic point process is the Poisson process. It is defined in $\mathbb{R}^d$ as follows.

Definition 2.2.10 (Poisson Process)

Let ϕ be a stationary simple point process on $E = \mathbb{R}^d$. If:

- the number of points $\phi \cap A$ observed in a bounded Borel set $A \in \mathcal{B}(E)$ is Poisson distributed with parameter $\lambda\nu_d(A)$:

$$\mathbb{P}(\phi(A) = k) = e^{-\lambda\nu_d(A)} \frac{(\lambda\nu_d(A))^k}{k!}; \tag{2.2.8}$$

  and

- the numbers of points $\phi \cap A_i$ observed in disjoint sets $A_i \in \mathcal{B}(E), i = 1, ..., n$ are independent,

then ϕ is called a *Poisson process* on E with *intensity* λ.

The intensity λ describes how many points are expected to be found in a unit volume, i.e. $\Lambda([0,1]^d) = \mathbb{E}(\phi([0,1]^d)) = \lambda\nu_d([0,1]^d) = \lambda$. To simulate a Poisson process on the computer, the random point generation is performed on a compact window $W \subset \mathbb{R}^d, \nu_d(W) > 0$.

Algorithm 5 Poisson Process Simulation

Require: $\lambda \geq 0$, simulation window $W \subset \mathbb{R}^d$

Sample number of points $n \sim Poiss(\lambda\nu_d(W))$

Generate $x_1, ..., x_n \sim \text{Unif}(W)$ independently

2.2.3 The Boolean Model

As stated above, the Boolean model serves as one of the simplest models for fiber systems. It is based on the basic concepts of the Poisson process and random compact sets. Its following definition is adapted from Ohser & Schladitz [17].

Definition 2.2.11 (Boolean Model)

Let $\Phi = \{x_0, x_1, ...\}$ be a Poisson process in $\mathbb{R}^d$ (the *germs*) with intensity $\lambda > 0$. Let $X_i, i = 0, 1, ...$ be a sequence of independent and identically distributed (i.i.d.) random, compact and convex sets (the *grains*) with the center of the circumscribed sphere in the origin and non-empty interior. In particular, they are independent of the Poisson process Φ. Then $\Xi = \bigcup_{i=0}^{\infty} (x_i + X_i)$ is called the *Boolean model* with *typical grain* X_0.

A common setup to model fibers with a Boolean model is to use cylinders as grains, where the height of the cylinder is significantly longer than its base [18]. Fig. 2.2.1 shows an example rendering of such setup. A strong advantage of the Boolean model is its fast and efficient simulation as the grains can be sampled independently.



Figure 2.2.1: Rendering of a Boolean Model realizations with cylinders as grains.

Algorithm 6 shows the pseudocode for generating a Boolean model. Direct implementation of this algorithm will lead to edge effects, hence, it is necessary to implement additional *edge treatment*. A simple solution is *plus-sampling*: For $X_0 \subset B_d(0, R)$ for some $R > 0$, instead of sampling on the simulation window W, sample on $W \oplus [0, R]^d$. Considering now only $W \subset W \oplus [0, R]^d$, W does not show

Algorithm 6 Boolean Model Simulation

Require: $\lambda \geq 0$, simulation window $W \subset \mathbb{R}^d$

Sample number of germs $n \sim Poiss(\lambda \nu_d(W))$

Generate n uniformly distributed points $x_1, ..., x_n \in W$

Generate n grains X_i following the grain distribution

Place $x_i + X_i$ in W for all i

edge effects; see Fig. 2.2.2a for a sketch in $\mathbb{R}^2$. Another solution is periodization of the window. Here, we simulate the Boolean model on W; however, we continue it periodically in $\mathbb{R}^d$; see Fig. 2.2.2b for a sketch in $\mathbb{R}^2$. Similarly to plus-sampling, considering only W, this removes edge effects [7].

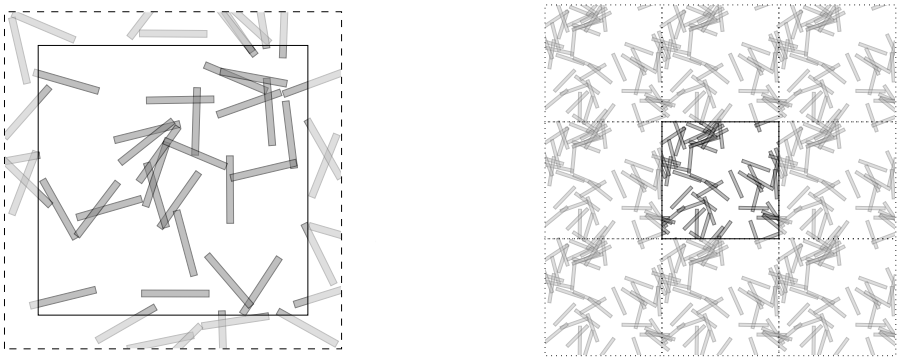

(a) Sketch of plus-sampling. (b) Sketch of periodization.

Figure 2.2.2: Sketches of edge treatment for Boolean models of cylinders.

The Boolean model is well-studied due to its simple analytical description. This entails a plethora of analytical results [7], [16]. Here, we will solely present formulae on the expected volume fraction and the number of intersections between cylinders, as we will need them throughout this thesis. The expected volume fraction V_V depends on the intensity of the Poisson process λ and the expected volume $\bar{V}$ of the typical grain X_0 by

$$V_V = 1 - \exp\{-\lambda \bar{V}\} \tag{2.2.9}$$

and is often referred to as one of Miles' formulae [7], [16], [17].

The expected number of intersections $\bar{n}_0$ depends on the cylinders' direction

distribution ψ, their radius r and length ℓ as

$$\bar{n}_0 = 2\lambda \left(\ell^2 r f_\psi + \pi \ell r^2 g_\psi + \pi \ell r^2 \right), \tag{2.2.10}$$

where

$$f_\psi = \int_{S^2} \int_{S^2} |p \times p'| \psi(p') \psi(p) \, dp' \, dp \tag{2.2.11}$$

$$g_\psi = \int_{S^2} \int_{S^2} |p \cdot p'| \psi(p') \psi(p) \, dp' \, dp, \tag{2.2.12}$$

as shown by Toll [19], [20]. Note that $\bar{n}_0$ is also called the "mean number of crossings per fiber" or the "mean number of grains that hit the typical grain". The formula corresponds to the more general formula $\bar{n}_0 = \lambda \mathbb{E}\left[\nu_d(X_0 \oplus \check{X}_0)\right]$, where X_0 is the typical grain [7].

2.2.4 Poisson Line Process

When fibers are much longer than the observation window, it may be useful to model them as infinite fibers instead. A naive approach is to exchange the cylinders in the Boolean model for infinite cylinders; Chiu et al. [7] explain the pitfall of this approach. Instead, Poisson lines are generated and their dilation constitutes the fiber model, see Fig. 2.2.3b. We define them following Chiu et al. [7] and Ambartzumian [21].

In 2D, directed lines can be represented on the cylinder

$$C^* = \{(\cos\alpha, \sin\alpha, p) \in \mathbb{R}^3 : p \in \mathbb{R}, \alpha \in (0, 2\pi]\}, \tag{2.2.13}$$

where α represents the line direction w.r.t. the x_1-axis and p is the (signed) distance of the line to the origin, see Fig. 2.2.3a. For undirected lines, this reduces to the half-cylinder

$$C = \{(\cos\alpha, \sin\alpha, p) \in \mathbb{R}^3 : p \in \mathbb{R}, \alpha \in (0, \pi]\}. \tag{2.2.14}$$

(Undirected) Poisson lines are then defined as a Poisson point process on C. They are characterized by their line density L, which is the expected length of lines in a unit area, and the orientation distribution ψ [7].

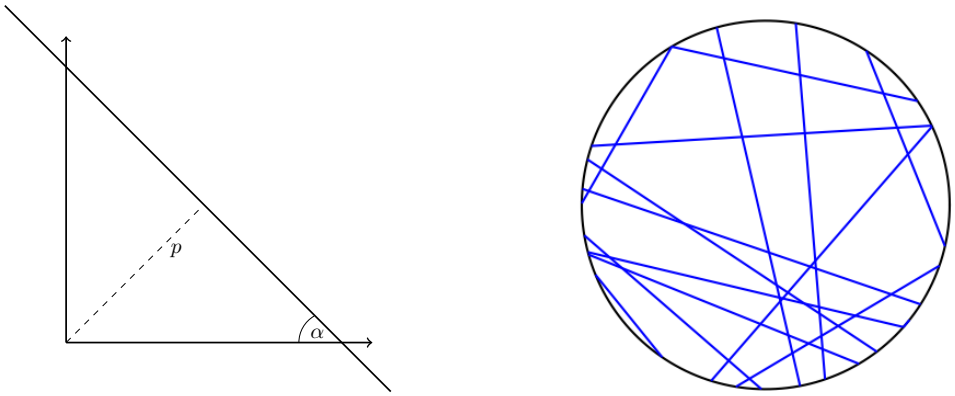

(a) Sketch of the representation of Poisson lines.

(b) Realization of Poisson lines (generated using [22]).

Figure 2.2.3: Poisson Line Process in 2D.

Defining the Poisson line process in 3D is trickier as its definition is not as illustrative as in the 2D-case [21]. We define a line as the tuple (u, v), where $u \in \mathbb{R}^3$ is the direction vector and $v \in \mathbb{R}^3$ a position vector such that the line can be represented as $l(t) = v + tu, t \in \mathbb{R}$. More specifically, $u \in S^2$, and the position v is a point in the tangent plane $t(u)$ to S^2 at u. This way, for its simulation in a ball $B_3(0, \frac{\sqrt{3}}{2})$, we simulate $u \sim \psi$. In order to sample a point $v \in t(u)$, we calculate the orthogonal unit vectors v_1, v_2 spanning the tangent space and the random vector $(r_1, r_2) \sim \text{Unif}\left(B_2(0, \frac{\sqrt{3}}{2})\right)$ in 2D. Then $v = u + r_1 v_1 + r_2 v_2$. To simulate the Poisson line process in a window $W = [0, w]^3$, we consider lines cutting the unit window $W' = [-0.5, 0.5]^3 \subset B_3(0, \frac{\sqrt{3}}{2})$, which we subsequently scale and translate.

Just like in the 2D case, the Poisson line process in 3D depends on the line density L and the orientation distribution ψ. For the simulation, however, it is easier to transform the line density to the expected number of lines $\gamma(L)$ (in the enclosing ball), sample the number of lines $n \sim Poiss(\gamma(L))$, and simulate n lines. Chiu et al. [7] provide a general formula for $\gamma(L)$ for the case $\psi = \text{Unif}(S^2)$. The pseudocode is given in Algorithm 7.

Algorithm 7 Poisson Line Process Simulation in a 3D window

Require: $L \geq 0$, direction distribution ψ, simulation window $W = [0, w]^3$

$n \sim Poiss(\gamma(L))$

for i in 1, ..., n **do**

Generate direction $(\theta, \phi) \sim \psi$

Generate $(r_1, r_2) \sim \text{Unif}\left(B_2(0, \sqrt{3}/2)\right)$

$u = \text{PolarToS2}(\theta, \phi)$

$v = w(M(\theta, \phi)(r_1, r_2, 0)^T + u + (\frac{1}{2}, \frac{1}{2}, \frac{1}{2})^T)$

if the line (u, v) does not intersect with W **then**

discard the line (u, v)

end if

end for

Chapter 3

Analysis of Fiber-Based Microstructures

Physical properties of fibrous materials highly depend on the orientations of their fibers. In particular, sheet molding compounds of carbon fibers (*C-SMC*) are a type of material consisting of stacked layers of fibers. In the automotive industry, C-SMC are of high interest due to their versatile behavior such as light weight, high stiffness, and strength, which is determined by their fiber direction distribution [3]. Hence, it is of high interest to estimate fiber directions using imaging methods.

Computed tomography (CT) imaging combined with certain image processing tools is an established method to estimate fiber directions from C-SMC materials as it generally allows to resolve the thin carbon fibers even on the inside of the material. However, it depends on access to a CT, which is both expensive in terms of time and money. Moreover, CT imaging of C-SMC is challenging due to the high fiber volume fraction and the low difference in X-ray absorption of fiber and matrix material. It also allows for only a small field-of-view for a sufficiently high resolution due to carbon fibers being extremely thin. This means that rather small samples have to be cut from the material, thus making the otherwise non-destructive method of CT imaging rather destructive, and necessitating many scans for sufficient representativity of the studied samples.

As an alternative, polarization imaging has the potential to measure fiber orientations of a C-SMC specimen: It measures the angle of linear polarization (AOLP)

reflected by the carbon fibers, which is directly related to the fiber orientation. AOLP measurement is possible thanks to a special on-pixel polarization filter sensor, patented by the Fraunhofer Institute for Integrated Circuits [23]–[26] and later commercialized by Sony in 2018. This method has the advantage of being cheap and easy to use in real-time, so it comes in handy during the manufacturing process without the need to prepare samples specifically. However, it only allows for imaging of the outer layers of the C-SMC material and is not sufficiently validated yet.

The work presented in this chapter has already been published in Keilmann et al. [27] and Duhovic et al. [28], where also details on the engineering application can be found. The work in Section 3.1 was performed by Miro Duhovic and Dominic Schommer; this section and Section 3.4 were written cooperatively with all coauthors. The corresponding data is hosted on Zenodo (`https://doi.org/10.5281/zenodo.13862632`). We start by presenting the samples and imaging methods we employed. In Section 3.2, we study possible methods to estimate the fiber orientation from CT images. In Section 3.3, we develop a suitable image similarity measure to compare the results of the CT images and the polarization images to each other. Finally, we discuss our results and conclude the chapter.

3.1 Polarization Imaging and Computed Tomography

We consider images of C-SMC materials from different manufacturers: The material SMCarbon® 24 CF50-12K and CF50-3K by POLYNT Composites Germany GmbH, and LyondellBasell's Quantum AMC®85593 and Quantum AMC®85590. Both consist of carbon fiber rovings with a length of 25 mm within a vinyl ester resin. Please refer to the original paper [28] for details on the specimens and their preparation. We imaged each specimen with the two modalities – a polarization camera and an X-ray microscope. First, the front and back of the specimen were scanned using the polarization camera VCXU-50MP by Baumer GmbH with an exposure time of 20 ms and a pixel spacing of approximately 0.21 mm. The 3D CT scans were carried out on an Xradia 520 Versa, manufactured by Carl Zeiss Mikroskopie GmbH. Scanning

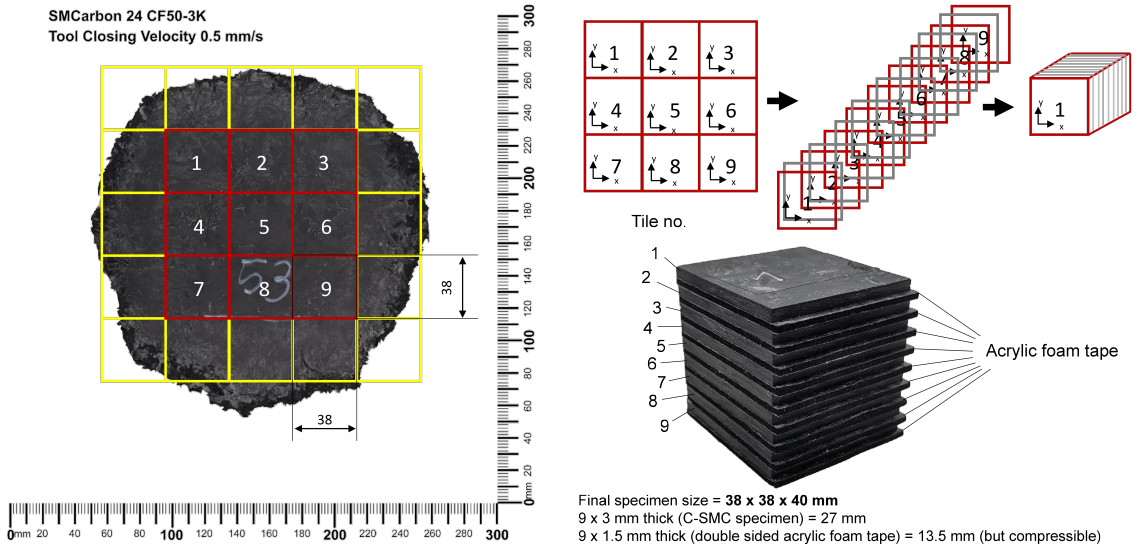

Figure 3.1.1: 3D CT scan sample preparation.

carbon fibers with an X-ray microscope is generally challenging because they provide little contrast to the resin. Moreover, both high resolution and a large field of view are necessary to reliably validate the polarization camera images. Hence, the Xradia 520 Versa is well-suited for resolving and visualizing carbon fibers due to its high resolution and ability to provide phase contrast. An illustrative example of one of the eight specimens is shown in Fig. 3.1.1. The scan quality could have only been improved using synchrotron radiation, which was outside the scope of this work.

Given the substantial difference between the in-plane dimensions and the thickness of the specimen, scanning the specimen as is would result in considerable variation in the distances the X-ray beams have to pass through the material, leading to a significant loss of scan quality. To address this issue, the sample was divided into 38 mm × 38 mm cut-outs using a Mutronic DIADISC 6200 precision saw with a cutting blade thickness of 2.5 mm. These cut-outs were then rearranged to achieve a cuboid shape of the specimen as shown in Fig. 3.1.1. Smaller cut-outs would have yielded a higher resolution with higher contrast. However, this would also have resulted in either a smaller area to be scanned, or in more cutting borders, which are a considerable source of error. Due to their undefined shape, we omitted the cut-outs at the edge areas of the specimen and stacked only the center areas 1-9 into a nearly cubic cuboid. In order to facilitate the identification of individual tiles in

the subsequent CT image, they were separated by double-sided acrylic foam adhesive tape.

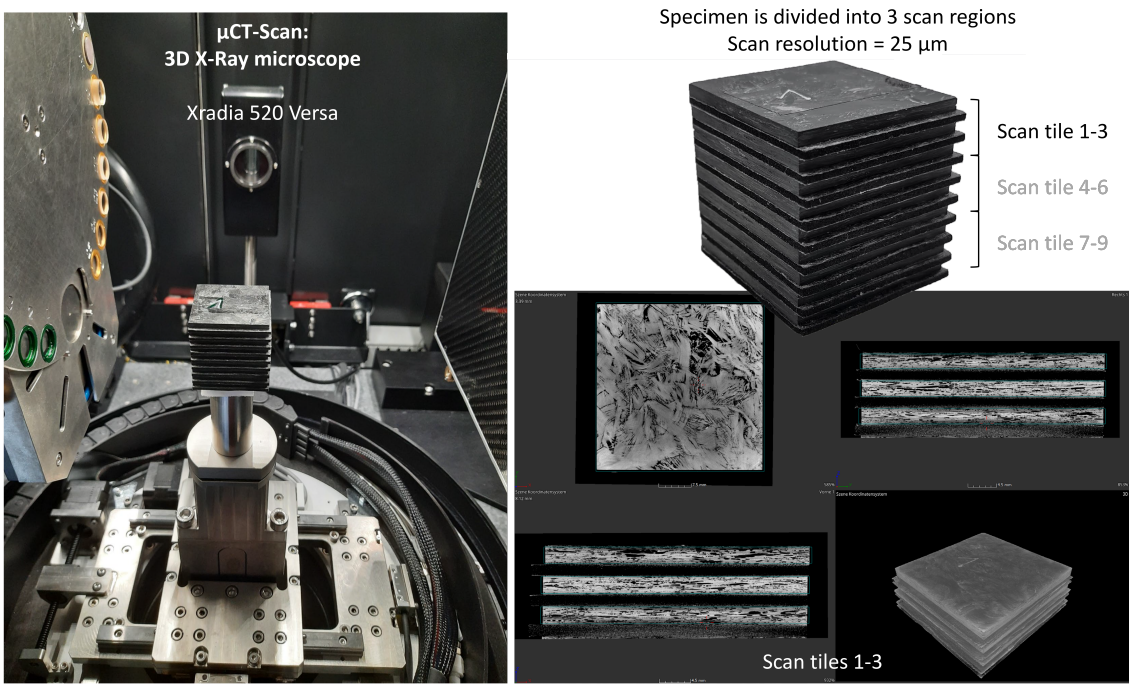

Figure 3.1.2: Left: Positioning of the C-SMC specimen in the scanning chamber of the Xradia 520 Versa 3D X-ray microscope. Right: µCT scan of the stacked tiles 1-3 of specimen 53.

To ensure optimal scan quality for the entire specimen, the nine tiles were scanned separately in groups of three, as shown in Fig. 3.1.2. Each scan covered a field of view measuring 76 mm × 48 mm, with nominal resolution (pixel size) 25 µm. Operating at 5 W power and a voltage of 60 keV, each scan involves 3 201 projections. During a brief exposure time of 2 sec per projection, a total of 20 individual images were captured at 0.1 s intervals and were averaged subsequently. Due to the phase contrast exploited here, matrix material and carbon yield a good gray value contrast for specimen 53, shown in Fig. 3.1.2. The matrix material is coded as low pixel values, i.e., dark, whereas the carbon fibers are coded as high pixel values, i.e., light. Notably, the light strands in the figure are not single fibers but fiber rovings. There is nearly no contrast or edge information within the fiber rovings, as the voxel size is larger than the fiber diameter. Note that we will therefore not directly calculate the local fiber orientation but the local sub-roving orientation. Given that neighboring fibers

must be fairly aligned due to the dense packing of fiber rovings, we can safely assume sub-roving orientations to correspond to local fiber orientations. For the sake of brevity, we will refer to the sub-roving orientation as the fiber orientation in the following. The same holds true for polarization imaging.

Moreover, the contrast is significantly lower for other specimens, see e.g. Fig. 3.3.2. Yet, we can estimate the fiber orientations accurately from the CT scans using the maximal response of anisotropic Gaussian filters [29], as we will discuss in the following.

3.2 Fiber Orientation Estimation

A fundamental concept in computer vision is scale-space theory. It describes at which scale image operations need to be performed to obtain information on the objects contained in the image. The foundation of scale space theory are isotropic Gaussian filters due to specific filter properties. Moreover, they can be implemented easily, performing fast computation. Hence, Gaussian filters are commonly used to perform differentiation on an image w.r.t. the appropriate scale [30]. Anisotropic Gaussian filters, on the other hand, give a handle on orientation as well as scale, which makes them the cornerstones of orientation space theory [31]. Anisotropic Gaussian filters have been employed for denoising images [32], [33] as they can be adapted to image structures and, hence, preserve edges.

Most established methods for estimating fiber directions are based on gradients such as calculating the image's Hessian matrix [17], [34], [35] or the second-moment matrix of the image's gradient, called the structure tensor [36]–[38]. In both methods, the local fiber directions result from the eigendecomposition of the respective matrix. Another method estimates fiber orientations using a filter bank of anisotropic Gaussian filters. More specifically, local fiber directions can be estimated by the direction of the maximal response of anisotropic Gaussian filters that are aligned along a given set of directions [29], [39]. In the following, we formalize all three methods and test their accuracy.

To define a Gaussian filter, consider an axis-aligned Gaussian kernel with standard

deviations $\sigma_1 > \sigma_2 > 0$ centered in the origin, i.e.,

$$g_{\sigma_1,\sigma_2}(x_1, x_2) = \frac{1}{\sqrt{2\pi}\sigma_1} \exp\left(-\frac{1}{2}\frac{x_1^2}{\sigma_1^2}\right) \cdot \frac{1}{\sqrt{2\pi}\sigma_2} \exp\left(-\frac{1}{2}\frac{x_2^2}{\sigma_2^2}\right), \tag{3.2.1}$$

$x_1, x_2 \in \mathbb{R}$. Its contour lines are axis-aligned ellipses with half-axis ratio $\omega = \sigma_2/\sigma_1$. We now rotate the kernel to get $g_{\sigma_1,\sigma_2,\theta}$, whose major half axis points in direction $\nu = (\cos(\theta), \sin(\theta))^{\mathbf{T}}$ for $\theta \in [0, \pi)$. Formally,

$$g_{\sigma_1,\sigma_2,\theta}(x_1, x_2) = \frac{1}{\sqrt{2\pi}\sigma_1} \exp\left(-\frac{1}{2}\frac{(\boldsymbol{x}^T\boldsymbol{\nu})^2}{\sigma_1^2}\right) \frac{1}{\sqrt{2\pi}\sigma_2} \exp\left(-\frac{1}{2}\frac{(\boldsymbol{x}^T\boldsymbol{\nu}^{\perp})^2}{\sigma_2^2}\right), \tag{3.2.2}$$

where $x = (x_1, x_2) \in \mathbb{R}^2$ and $\nu^{\perp} = (-\sin(\theta), \cos(\theta))^T$.

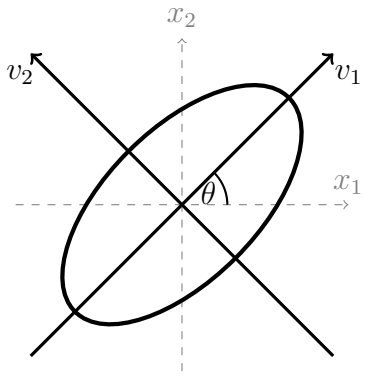

Figure 3.2.1: The Gaussian ellipse, i.e., contour line of the Gaussian function with major axis v_1 and minor axis v_2.

Fig. 3.2.1 illustrates the anisotropic Gaussian kernel. Throughout this thesis, we employ the implementation by Keilmann et al. [27]. The isotropic Gaussian kernel $g_\sigma := g_{\sigma,\sigma}$ is a special case of its anisotropic version and does not need such decomposition.

3.2.1 Structure Tensor

For the image f, the gradient ∇f describes directions in f as it is aligned with the fiber's surface normal, which in turn is orthogonal to the fiber direction. Further convolution with a Gaussian kernel allows for direction estimation that is robust against noise.

The structure tensor is defined as

$$S_{\sigma,\rho} = g_\rho * \left(\nabla(f * g_\sigma) \cdot \nabla(f * g_\sigma)^T\right) \tag{3.2.3}$$

with suitable smoothing parameters $\sigma, \rho > 0$ as denoted in Wirjadi et al. [40] and proposed by Haglund [36]. Its eigenvector corresponding to the smallest eigenvalue describes the local fiber direction.

As argued and done by Krause et al. [38] and Wirjadi et al. [40], we set $\sigma = r$ for a fiber radius of r. This choice was empirically confirmed by Pinter et al. [41]. The parameter ρ is less impacted by the size of the underlying structure. Hence, we use a constant $\rho = 6.0$, as was found optimal by Pinter et al. [41].

3.2.2 Hessian Matrix

The image's Hessian matrix

$$H_\sigma = \nabla\nabla^T(f * g_\sigma) \tag{3.2.4}$$

with smoothing parameter $\sigma > 0$ describes image curvature, which is minimal along the fiber direction. Therefore, the local fiber direction is determined by the Hessian's eigenvector corresponding to the smallest eigenvalue. Analogous to the structure tensor, we set $\sigma = r$ following Wirjadi et al. [40] and Pinter et al. [41].

3.2.3 Maximal Response of Anisotropic Gaussian Filters

To filter an image of fibers for directions, imitate the elongated shape of a fiber with the d-dimensional anisotropic Gaussian (function) g_θ. Its parameters give a handle on the orientation, length, and diameter for the fiber model [42]. The filter response $(g_\theta * f)(\boldsymbol{x})$ to the image f is maximal when θ matches the local fiber direction in the point $x \in \Xi$, where Ξ is the fiber system. Therefore, one can find the direction ν that maximizes the filter response for each $x \in \Xi$ [40]:

$$\nu(x) = \underset{\theta \in S^1_+}{\operatorname{argmax}} (g_\theta * f)(\boldsymbol{x}) \tag{3.2.5}$$

$\nu(x)$ is estimated by calculating the convolution $(g_\theta * f)(x)$ for a finite set of directions that covers S^1_+ as evenly as possible [43]. Hereafter, we will call this the *MR method*.

The method's accuracy is mainly influenced by the parameter σ_2, which we will set to $r/2$ in the following. This is motivated by the 2σ rule for the normal

distribution, which says that approximately 95% of the data points are within two standard deviations of the mean [44]. Hence, a correctly aligned filter kernel g_θ that is centered within the fiber covers the fiber's thickness with 95% of its weight when $\sigma_2 = r/2$, where r is the fiber's radius. Pixels that are further away than $2\sigma_2$ are barely taken into account. This ensures that the filter response is maximal when the 2-dimensional Gaussian filter kernel is aligned with the fiber: A much larger variance might take too many pixels outside of the fiber into account, while a much smaller variance results in filter kernels whose main mass is concentrated in an elliptical region that is thinner than the fibers. In this case, the ellipse might fit inside the fiber for several angles θ, which makes it harder to accurately detect the direction for which the maximum is attained. The parameter σ_1 corresponds to the elongation of the fiber. We observed that it has rather little influence on the estimation accuracy. Yet, it should hold $\sigma_1 < \ell/4$, where ℓ is the fiber length, analogous to the argument above, and the Gaussian kernel should still be clearly elongated.

3.2.4 Experimental Validation Study

Wirjadi et al. [40] compared the structure tensor and the Hessian matrix to other methods for orientation estimation based on 3D images of single synthetic fibers and identified them as the most accurate. Pinter et al. [41] further investigated their accuracy on images of multiple fibers, finding the structure tensor to be comparably more robust.

In their comparison, Wirjadi et al. [40] and Pinter et al. [41] both identified the Maximal Response (*MR*) method as robust to noise but suffering from the trade-off between runtime and accuracy in 3D. However, there are use cases where the image quality is too low for methods based on local gray-value derivatives on the one hand, and where, due to the production process, the fibers are known to be oriented in a 2D subspace anyway. This holds, for instance, true for µCT images of sheet molding compounds (SMC), a material where reinforcing fibers lie within a plane. Then, only 2D images have to be analyzed, similarly to stereological approaches. In 2D, the MR method is less restricted regarding runtime and even outperforms other methods due to its robustness with respect to low image contrast [43]. To our knowledge,

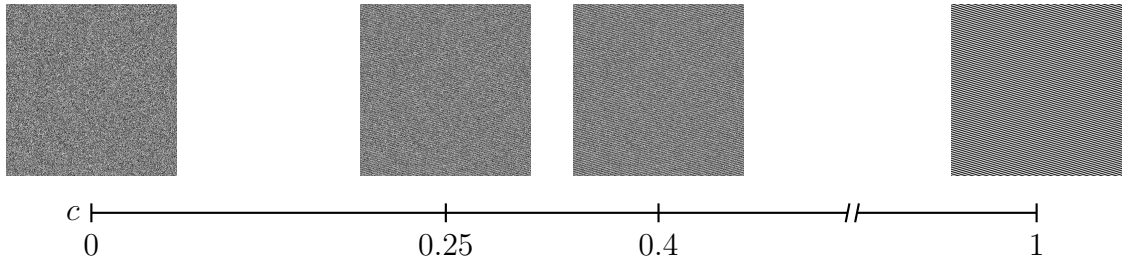

Figure 3.2.2: Visualization of the experimental data set for varying contrast c see Eq. 3.2.7.

however, the high performance of the MR method on SMC data has not been studied systematically yet.

Hence, we study the accuracy of the MR method and the gradient methods for SMC materials specifically. For this, we set up experiments on a synthetic image of a fiber bundle with low resolution. We add noise and imitate varying levels of contrast between the noise and the fiber bundles. Such a setup allows to compare estimated directions with a ground truth. In addition, we show that the experimental results translate to real-world data.

3.2.4.1 Setup

We evaluate the MR method on synthetic images with known constant fiber orientation. The design of the images is inspired by our application example. There, bundles of nearly parallel thin fibers form the main building block of the microstructure. The synthetic images shall mimic the fiber system within one such bundle.

Given an image of size 512 $\times$ 512 pixels, a width parameter w, and an angle θ, we define an image $F_{\theta,w}$ by setting

$$F_{\theta,w}(x,y) = \frac{\sin(x\sin(\theta) + y\cos(\theta))}{2w} + \frac{1}{2}. \tag{3.2.6}$$

For each $\theta = 0°, 1°, 2°, ..., 179°$ and $w = 1, 2$, we generate such an image. These gray-value images represent idealized fiber bundles with known fiber direction and a radius of $r = \pi w/2$ pixels. Note that we choose a significantly smaller radius than Wirjadi et al. [40] and Pinter et al. [41], who use cylinders with a radius of at least 2.5 voxels. Our choice is again inspired by our application images.

As background noise, we generate images B of size 512×512 with pixels sampled from the uniform distribution in $[0, 1]$.

To model images of varying contrast between background and fiber, we consider images of the form

$$(1 - c)B + cF_{\theta,w} \quad \text{for} \quad c \in [0, 1], \tag{3.2.7}$$

see Fig. 3.2.2. The MR method is applied as described below, which yields a mean absolute angular error $MAAE$ w.r.t. the known fiber direction. For comparison, we additionally apply the algorithm to images preprocessed by a median filter of size 3×3. This is motivated by the fact that smoothing with median filters is a typical preprocessing step for real image data.

The MAAE is determined as follows. The synthetic fiber image $F_{\theta,w}$ is binarized with a threshold of 0.75. The resulting image serves as a mask to include only pixels within fiber cores.

Further, we want to make sure that we only estimate the estimating bias and do not confound it with a sampling bias, i.e., lower or higher sampling probability for certain directions. For example, in an image, one can place more fibers and longer fibers in diagonal directions than in the horizontal and vertical direction. Therefore, we only evaluate pixels within a circle around the image's center. In order to avoid boundary effects, the circle radius is set to 206 pixels.

For each realization B, we are interested in the maximum of the MAAE over all θ per method. We run the MR method with $\sigma_1 = 20.0, \sigma_2 = 0.75w \approx r/2$, the structure tensor with $\sigma = r,\ \rho = 6.0$ and the Hessian matrix with $\sigma = r$ as argued in the methods' sections.

3.2.4.2 Results

Fig. 3.2.3 shows the mean error for unfiltered images and the standard deviations for 50 noise realizations. The structure tensor is affected by low contrast for both $r = \pi/2, \pi$ and is outperformed by the MR method. The Hessian matrix is not able to match the performance of the other methods, see Fig. 3.2.3.

Applying a median filter to noisy images is a common preprocessing step to get rid of noise while preserving edges. However, the errors are considerably larger than

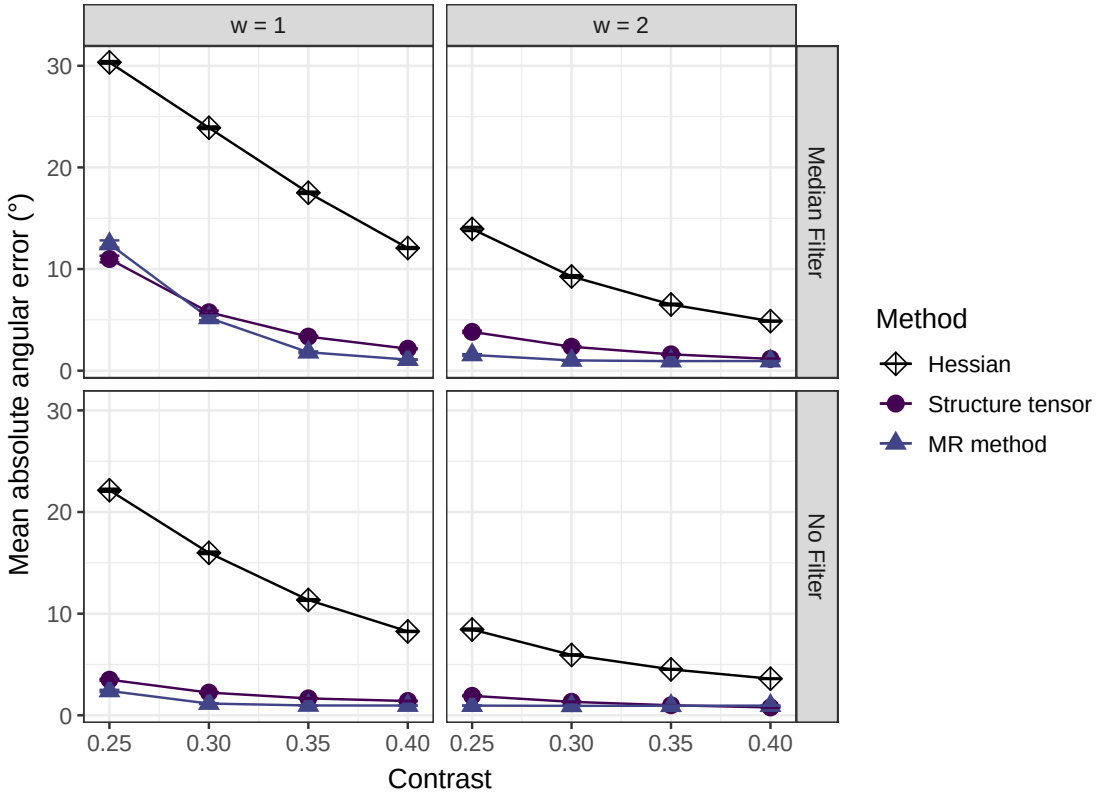

Figure 3.2.3: Error plot for the experimental setup where orientation estimation methods are applied to synthetic fibers that are overlayed with noise. The x-axis depicts the contrast c between noise and the synthetic fibers, see Eq. 3.2.7. The y-axis depicts the MAAE: For each contrast, method, filter condition and fiber diameter and noise image, the maximal angular error was calculated over the fiber directions $\theta = 0°, ..., 179°$. Then, the mean was taken over all 50 noise images. The mean is depicted as a point symbol, the standard deviation is depicted with bars. Note, however, that the standard deviations are small and therefore the bars delimiting the interval are in most cases covered by the symbol for the mean value.

for unfiltered images as direction information is lost by the undirected median filter, see Fig. 3.2.3.

3.2.5 Application to Sheet Moulding Compounds

Due to the production process of SMC, the fibers lie within a plane. Hence, estimating the fiber orientations based on 2D image slices is sufficient. For that purpose, we preprocess the CT images using the software MAVI [45]: We crop the images to obtain one subvolume per tile. We rotate each such image such that the tile surface is aligned with the image's x-y-plane. The fiber orientations are then computed for each x-y-slice of the rotated images.

We process the image slices using ToolIP [46]. First, we equalize gray values by applying a mean filter with mask size 49 and subtracting the result from the original image. Next, we estimate the fiber orientation by applying the MR method as implemented by Keilmann et al. [27], where we employ cubic interpolation. We use the variances $\sigma_1 = 25.0, \sigma_2 = 2.0$ for the Gaussian filters since these are the most accurate variances determined in [27] that can still imitate the shape of a fiber. We restrict the possible orientations to $\theta = 0°, 1°, ..., 179°$. Note that we omit $\theta = 180°, 181°, ..., 359°$ as the choice between θ and $\theta + 180°$ is ambiguous for fibers. For the sake of consistency when comparing the three methods for fiber orientation estimation, we apply the structure tensor and the Hessian matrix with $\sigma = 4.0$ and $\rho = 6.0$.

In order to exclude orientation measurements that are not well-defined, we threshold the response with Niblack's method [47] using a window size of $w = 4\sigma_2$ following Schladitz et al. [43], and the threshold 0.6. In addition, we exclude components of the mask that are very small, i.e. we erode the mask with a square of size 3×3 pixels, then exclude connected components with a size smaller than 100 pixels, and dilate the mask with the same square again.

Like Schladitz et al. [43], we exclude all pixels that are $2\sigma_1$ close to the image border. Finally, we stitch the results of the top layers of the tiles back together, padding areas that were excluded or not scanned (see Fig. 3.1.1).

Despite there barely being any contrast within the fiber bundles, the MR algorithm

provides a fairly accurate estimation of fiber directions, whereas the gradient-based methods are struggling, see Fig. 3.2.4.

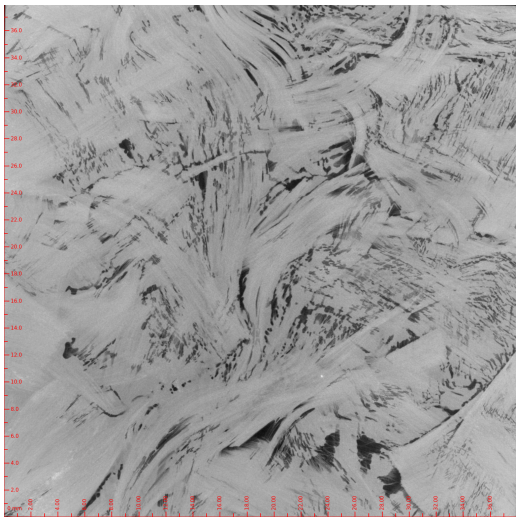

(a) Original slice, gray-values are spread for improved visibility.

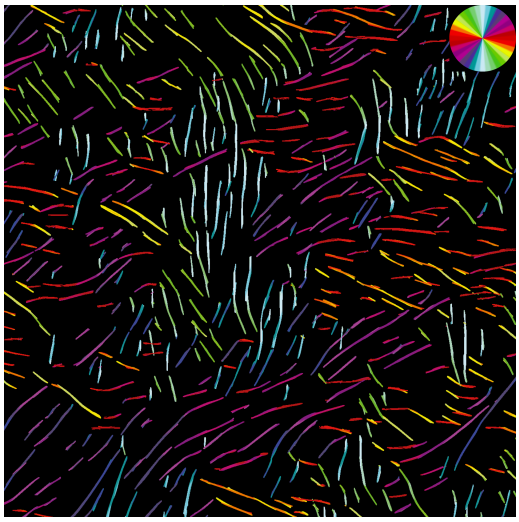

(b) Result using the MR method.

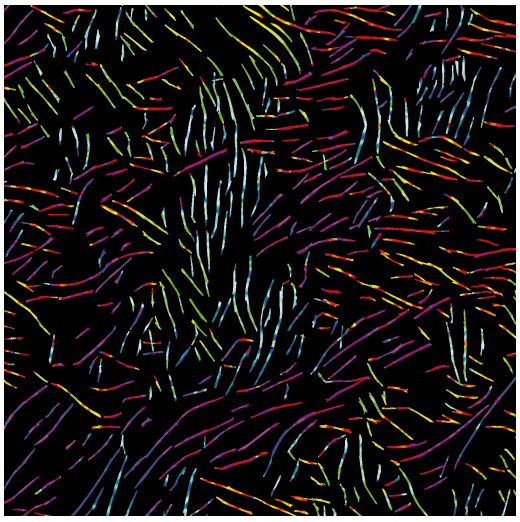

(c) Result using the structure tensor.

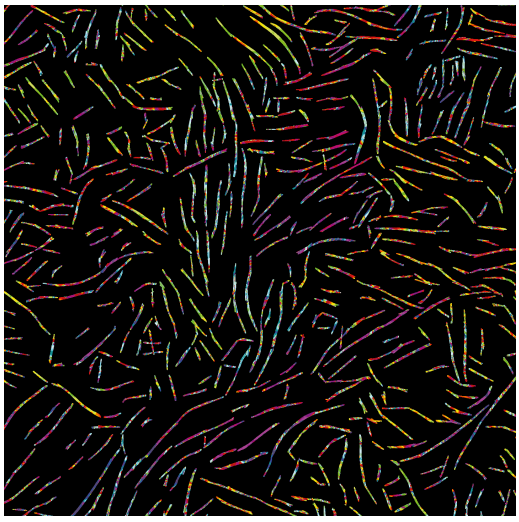

(d) Result using the Hessian matrix.

Figure 3.2.4: Direction estimation of SMC with carbon fibers. The directions are color-coded, see color wheel at the top-right side.

3.3 Image Similarity Measures for Multimodal Data

3.3.1 Image Registration of 2D Orientation Data

To validate the orientation measurement via polarization imaging using the MR results, we first need to align the images from both modalities. This means that pixels showing the same point in the specimen have to be identified in both images. This procedure is called registration [48]. First, we explain how the polarization and CT images are related. Then, we introduce the needed measure for image similarity, which we later also use for validating the polarization images. Subsequently, we formalize our registration process, and finally, introduce deviation categories for validation.

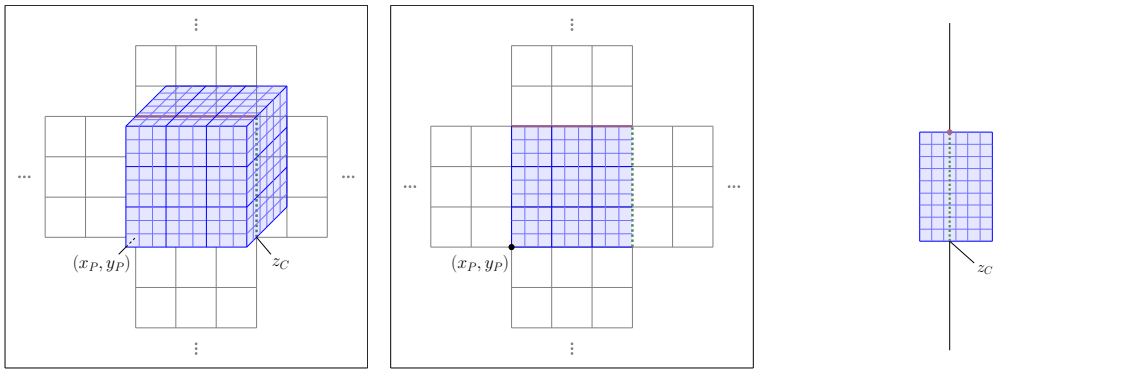

(a) Schematic visualization of the full registration process.

(b) Schematic visualization of registration w.r.t. the x-y-position.

(c) Schematic visualization of registration w.r.t. the z-slice.

Figure 3.3.1: Schematic visualization of the registration process. The polarization image is depicted in black-white, whereas the CT image is depicted in shades of blue. For reference between depictions, one shared image edge is depicted in red and another one in dashed green.

Fig. 3.3.1 illustrates the registration process for our CT and polarization images: The polarization image covers only the top or bottom surface of the specimen, yet its whole extent. It has a size of $1\,232 \times 1\,028$ pixels, and its pixel indices are denoted as x_p, y_p. The CT images, on the other hand, cover the whole depth of the specimen,

but only for a specific tile of the specimen. They have a size of $1\,520 \times 1\,520 \times z$ voxels where z varies due to the varying thickness of the specimen. However, with a voxel edge length of 25 µm, the CT images have a far higher resolution than the polarization images whose pixels have an edge length of 210 µm. For comparability, we downscale the x-y-slices by a factor of 8.4 with the new pixels being assigned the mean of pixel values within the mask. Remember that angles cannot be averaged in a straightforward way, see Section 2.1. The downscaling yields image slices of size 172×172 pixels. We denote the voxel indices of the downscaled image slices as x_c, y_c, z_c.

To register the CT and the polarization images, we need to align the CT image correctly with the corresponding position (x_P, y_P) in the polarization image on the one hand. On the other hand, we need to find the x-y-slice z_C in the CT image which depicts the surface. For both the registration process and the validation later on, image similarity has to be quantified. We base the similarity measure on the mean absolute error (MAE).

To take the periodicity of angles into consideration [8], we appropriately adapt the usual formulas of the MAE to the mean angular deviation (MAD) as follows: We calculate the deviation map between the polarization image p and the slice-wise MR result c based on the CT scan as

$$m(x_c, x_p, y_c, y_p, z_c) = \begin{cases} |p(x_p, y_p) - c(x_c, y_c, z_c)|, & \text{if } |p(x_p, y_p) - c(x_c, y_c, z_c)| \leq 90° \\ 180° - |p(x_p, y_p) - c(x_c, y_c, z_c)|, & \text{otherwise.} \end{cases}$$

To calculate the MAD, we take the mean of the deviation map m over every pixel within the mask M when placing the mask at position (x_P, y_P):

$$\mathrm{MAD}(x_P, y_P, n_x, n_y, z_c) = \frac{1}{n_x n_y} \sum_{x_c=0, y_c=0}^{n_x, n_y} \mathbb{1}_{(x_c, y_c) \in M} m(x_c, x_c + x_P, y_c, y_c + y_P, z_c)$$

for a CT image of size $n_x \times n_y$, so in our case $n_x, n_y = 172$. Note that $x_P < 1\,232 - n_x, y_P < 1\,028 - n_y$ to ensure valid pixel indices of the polarization image. Note that the MAD is a generalization of the MAAE in Section 3.2, which allows for different image masks.

We first register the downscaled MR result and the polarization image visually for each tile by overlaying the images and moving them in relation to each other,

until they seem well aligned. This gives us the indices x'_P, y'_P, z'_C. Next, we precisely register them brute-force by minimizing the MAD. More specifically, we calculate

$$(x''_P, y''_P, z''_C) = \underset{\substack{x_P \in [x'_P-25, x'_P+25], \\ y_P \in [y'_P-25, y'_P+25], \\ z_c \in [0,15]}}{\operatorname{argmin}} \operatorname{MAD}(x_P, y_P, n_x, n_y, z_c).$$

Subsequently, for each pixel (x_c, y_c), we pick the slice z'''_C of the MR result that minimizes the MAD w.r.t. the registered polarization image:

$$z'''_C = \underset{z_c \in [0,15]}{\operatorname{argmin}} m(x_c, x_c + x''_P, y_c, y_c + y''_P, z_c)$$

This provides a way of mimicking possible shine-through effects in polarization imaging.

For each specimen, we report the MAD after registration, i.e. $\operatorname{MAD}(x''_P, y''_P, n_x, n_y, z'''_C)$. Moreover, we combine both the results for the upper and lower surface of the specimen. Note that for the lower surface, the polarization image has to be mirrored regarding its position and angular pixel value, and for the CT images, the lowest slices must be used. Additionally, we present the area fraction of the following deviation categories w.r.t. the MAD map:

- Very low: $[\ 0°,\ 5°)$
- Low: $[\ 5°, 10°)$
- Fair: $[10°, 20°)$
- High: $[20°, 90°]$

3.3.2 Comparison of Layerwise Orientation Distributions

In this section, we aim to determine how much information on the orientation distribution for the whole specimen is lost when using only surface images. We expect the material to have the same orientation distribution throughout all layers due to the manufacturing process. As the orientation distribution is critical for the material's physical behavior, we validate this expectation.

For this, we compare the histograms of interior image slices with the surface image slices as registered in Section 3.3.1. We select the central image slice for each material layer for LyondellBasell's materials, yielding 4 equidistant image slices. As the Polynt material has 8 material layers, we analogously select the central image slice for every other layer to ensure comparability. The histograms are derived from the local fiber orientation values as the fiber rovings are not clearly distinguishable anyway.

Instead of the raw histograms, we present the kernel density estimates of the orientation distribution using Sheather & Jones' method [49] with a factor of 2 to estimate the bandwidth and the Gaussian kernel for smoothing. For periodicity treatment, we extend the histogram to $(-180°, 360°)$ by replicating the original values.

3.3.3 Results

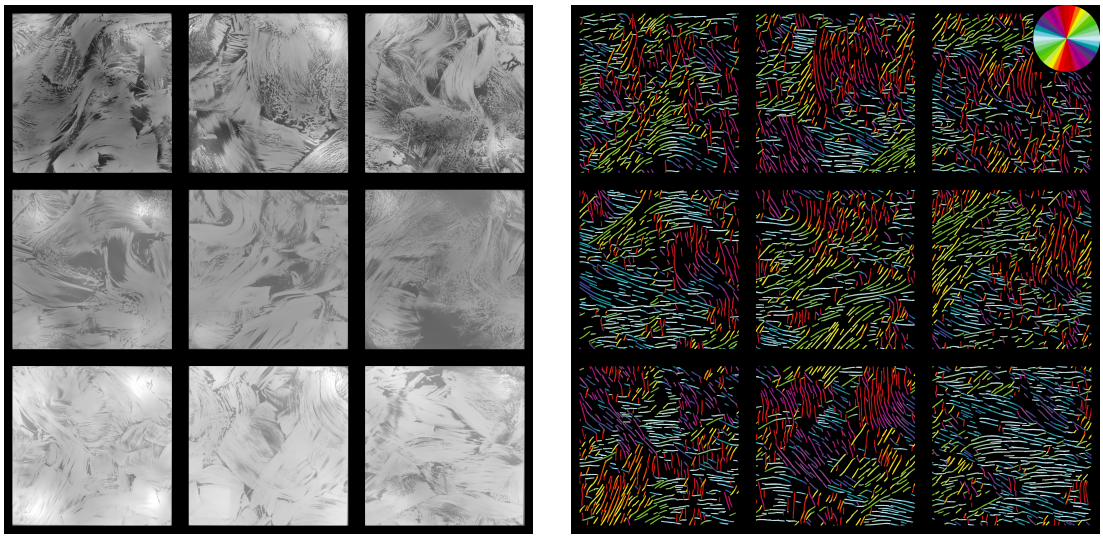

(a) Spread slices of the µCT scans stitched together.

(b) Fiber orientations after applying the MR method to the µCT scans (dilated for better visibility).

Figure 3.3.2: Surface layer of specimen 19 (µCT scans).

In order to validate the polarization images on µCT scans, we first calculated the local fiber orientations from the µCT images using the MR method. The µCT

images are inevitably of low resolution and low contrast since we aimed at a large field of view. Nevertheless, the MR method yields fairly robust results, see Fig. 3.3.2.

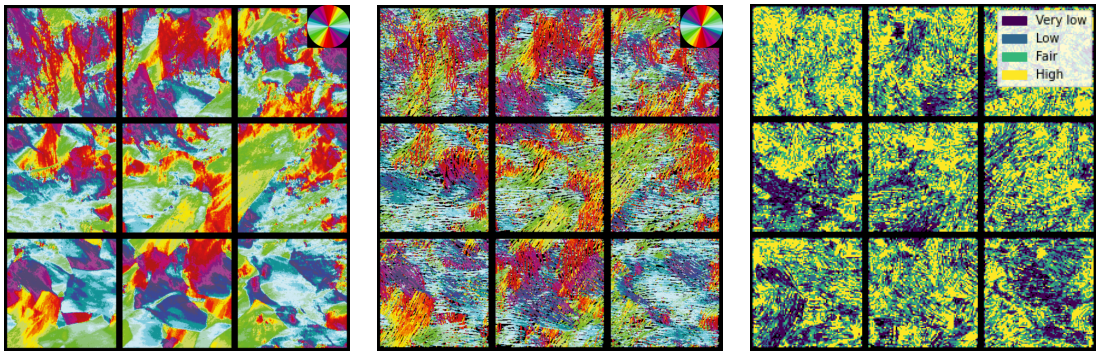

(a) Results of the polarization camera after registration.

(b) MR results (downsampled µCT) after registration.

(c) Deviation plot between polarization images and MR results.

Figure 3.3.3: Results of the top layer from specimen 19 for both imaging modalities.

Next, we registered the downsampled MR results and the polarization images. As can be seen in Fig. 3.3.3, the images seem well-matched and appear remarkably similar. Note though that the color wheel covers 10° per color. A substantial area features deviations above 20° as the plot in Fig. 3.3.3c reveals. We calculated the exact deviation areas and the MAD for all specimens and listed them in Table 3.3.1. The MAD was consistently around 20° and well over half the area was estimated with a deviation below 20°. Remarkably, in around a quarter of the area, deviation was found to be very low.

To address the question of how representative the surface layers are of the whole specimen, we estimated the densities of the orientation distribution, see Section 3.3.2, for the surface layers and 4 interior layers. From Fig. 3.3.4, it can be seen that the fiber orientation distribution was considerably similar for both surface and interior layers. However, this might not be generalizable to all C-SMC materials as this behavior will depend on the production process.

Caution should also be taken when deciding on the size of the sample. For example, we chose the tile size slightly larger than the roving length. Thus, a tile's orientation histogram was dominated by the behavior of the few rovings that are

Table 3.3.1: Mean angular deviation (MAD) and area fractions of deviation categories for the surface layers of each specimen.

Specimen	MAD	Very low	Low	Fair	High
19	18.33°	0.32	0.17	0.19	0.32
33	21.28°	0.26	0.15	0.20	0.40
53	21.13°	0.27	0.16	0.19	0.39
66	23.02°	0.23	0.15	0.19	0.43
86	23.74°	0.23	0.15	0.19	0.44
97	21.68°	0.25	0.15	0.19	0.40
120	26.60°	0.17	0.12	0.19	0.52
131	25.95°	0.18	0.13	0.19	0.50

observed in the field of view. So in this case, the surface layers were not representative of the whole sample, as can be seen in Fig. 3.3.5. Fortunately, this is just a statistical problem, which we eluded by using the histograms of the whole specimen layers. This means we chose our sample large enough to be statistically representative of the material's orientation distribution. Further plots are provided in the supplementary material `https://doi.org/10.5281/zenodo.13862632`.

3.4 Discussion

Imaging C-SMC is a challenging task due to the similar physics of carbon fibers and resin, resulting in low contrast images. Hence, polarization imaging is an attractive alternative as it can differentiate fibers and resin due to the fiber's polarization properties. Moreover, none of the established methods are applicable for inline quality inspection, whereas polarization imaging is fast, cheap, and yields a large field of view. Yet to our knowledge, it has only been validated for uni- and bidirectional carbon material [23], [50], [51]. Since SMC material is multidirectional and, thus, more complex, we validated polarization imaging with CT imaging on C-SMC materials

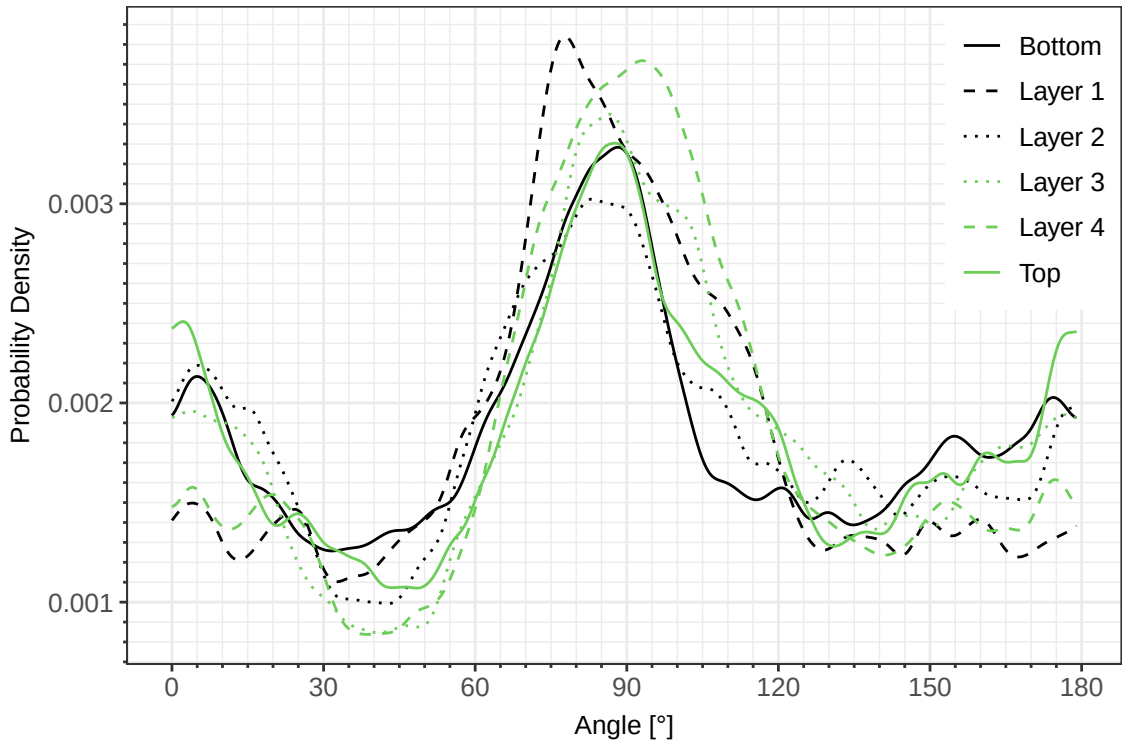

Figure 3.3.4: Kernel density estimates for the fiber orientation distribution of specimen 19 (all 9 tiles combined), calculated from its µCT scans. See Section 3.3.2 for the difference between the orientation distribution as shown here and the local orientation as shown in Fig. 3.3.3a

which are commercially available.

For the samples considered, we observed an encouraging visual similarity between both imaging modalities. However, we identified a considerable mean deviation between the orientations from the polarization images and those estimated from CT images of up to 25°. Although computed tomography is an established method, its results should be taken with a grain of salt: The scans struggle with the contrast between fibers and resin within the rovings due to the similar and low X-ray absorption contrasts of carbon and the polymer and due to the partial volume effect, both causes amplifying each others effect. The partial volume effect is particularly prominent as the voxel edge length of 25 µm exceeds the thickness of an individual carbon fiber by far. Nevertheless, some scans do reveal nicely the fiber rovings and these in turn can be distinguished nicely from the polymer matrix, see Fig. 3.1.2. Moreover, the

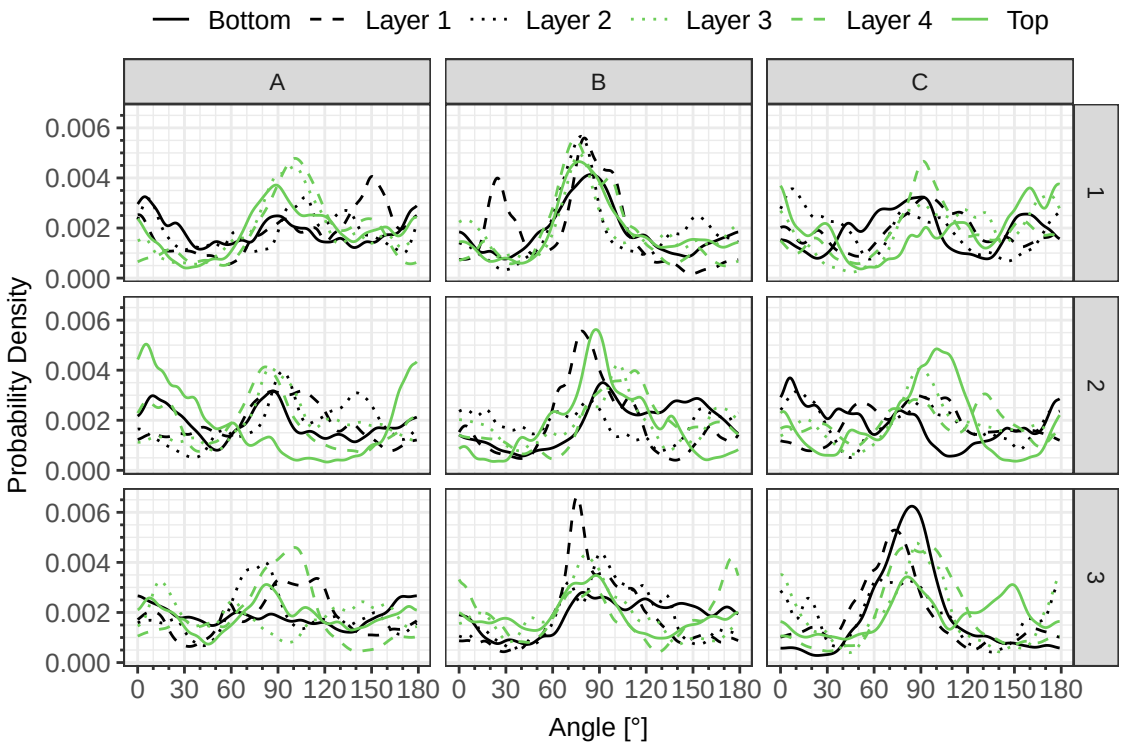

Figure 3.3.5: Kernel density estimates for the fiber orientation distributions of the individual tiles of specimen 19, calculated from its µCT scans. See Section 3.3.2 for the difference between the orientation distribution as shown here and the local orientation as shown in Fig. 3.3.3a

MR method succeeds in estimating fiber orientation in spite of the low gray value contrast within rovings.

Even polarization imaging is not able to perfectly differentiate between fibers and resin: Atkinson et al. [23] identified specular reflection of the resin as one possible cause of error. This might also explain the error range observed in this work: Resin-rich regions or regions where the carbon fibers are further below the surface of the specimen than others might be subject to larger errors due to the optical properties of the resin. In such areas, the polarized light ray and the angle of polarization might undergo some distortion as the ray passes through the resin before being registered by the camera's pixel sensor. This hypothesis could be validated by analyzing the local fiber area fraction in the slices and comparing it to the deviation plot in Fig. 3.3.3c. In addition, specimens of varying fiber volume fraction (in this

work, all specimens had an overall constant fiber weight fraction of 50%) could be analyzed to prove or disprove this hypothesis. Whereas the underlying mechanisms and sources of error for CT imaging are well studied [52], there exist only a few studies for polarization imaging [23], [50], [51], [53]. For example, it is yet unknown whether polarization imaging records only the uppermost fibers of the material or whether shine-through artifacts exist, which would explain differences between CT and polarization imaging. Hence, further work is planned to investigate its artifacts in more depth. The results are thus seen as encouraging as these artifacts could be corrected for or possibly even used to describe other properties of the material such as optical surface quality.

Further research opportunities include the development of a fair comparison method between both imaging modalities: Since C-SMC surface layers are not perfectly planar, it was tricky to identify the uppermost layer in the CT scans. Still, the minimum over surface-adjacent layers yielded fairly good results. Moreover, image processing of angular data is rather rare, including metrics for image comparison. In this chapter, we adapted the established mean absolute error (MAE) to the more appropriate mean angular deviation (MAD), taking into account the periodicity of angles. Although the MAE and the analogous mean squared error (MSE) are simple and well-explainable signal fidelity measures, they often fail to capture human perception of similarity [54]. A similar, well-researched problem is the analysis of diffusion tensor images, which also incorporate orientation information. Such tensors also need to be normalized [55], [56]. However, the difference measures used in this context are less intuitive than the MAE. Besides, different from angles, tensors provide information on the strength of orientation (anisotropy). Eventually, developing or adapting more sophisticated methods to angular data was outside the scope of this thesis.

Chapter 4

Modeling Fiber-based Microstructures

In this chapter, we study algorithmic methods of generating non-overlapping fiber geometries. We start with a literature review in Section 4.1, proceed with the introduction of the fiber model by Altendorf & Jeulin [57], see Section 4.2, and adapt this method for fiber bundles, see Section 4.3. In Section 4.4, we extend the Altendorf-Jeulin model to inter-fiber contacts, and evaluate its performance in Section 4.5. Section 4.6 closes this chapter with a discussion.

Parts of this chapter have already been published [58], in particular Section 4.1, Section 4.4, and Section 4.6. Section 4.2 was extended by Section 4.2.3 for this thesis. Section 4.5 was extended by the error measure mean absolute angular error (MAAE), another test case, and a test in Section 4.5.4.

4.1 Literature Review

Existing fiber models can be differentiated into models without fiber interaction and those with interaction. Models without interaction usually model single fibers independently of each other, which is why the fibers may intersect. Models with interaction, on the other hand, model the fiber position or shape depending on the rest of the fiber system, usually to avoid any intersection. Such fiber systems are called hardcore fiber systems.

The simplest model without interaction is the Boolean model [7], [16], [17]. Here, objects such as cylinders mimic the fibers and are placed independently following a Poisson point distribution, as defined in Section 2.2.3. A similarly classic approach is to dilate a Poisson line process, so that the dilated lines mimic endless fibers [59], see Section 2.2.4.

Fiber systems including a curvature can be achieved by using a random walk. Such a model was introduced by Wirjadi [60] and further extended to endless fibers [61]. For smoother fiber shapes, Faessel et al. [62] connect points of a random walk with splines, and Townsend et al. [63] place Bezier curves between points. As more general approaches, Gaiselmann et al. [64] proposed a germ-grain process combined with an autoregressive model; Weber et al. [65], [66] proposed modeling fibers copula-based.

Turning now to hardcore fiber systems, their simulation algorithms can generally be categorized into two distinct approaches, the sequential approach and the collective rearrangement approach. In sequential approaches, fibers are added sequentially to the fiber system such that they do not intersect. In collective rearrangement, the fibers are generated simultaneously and may intersect in the initial configuration. In a subsequent step, their intersections are removed.

One of the first models to achieve a hardcore system is the random sequential adsorption (RSA) model. Here, elements such as straight cylinders are generated independently following a given distribution on length, radius, and/or orientation. These elements are placed iteratively into the existing system if they do not cause any intersections. Otherwise, they are resampled. However, these models allow for rather low volume fractions [67], [68]. There are several variations and extensions of the original RSA approach, such as allowing fibers to "grow" until they intersect other fibers [69]. This allows for higher volume fractions up to 22.5 % at the cost of less control over the length distribution.

Sedimentation models [70]–[73] usually describe fiber systems that are obtained by fibers subsequently falling on top of each other. They can achieve higher volume fractions up to 80 %. However, their fiber direction distributions are roughly limited to the plane.

When collective rearrangement approaches remove intersections, they calculate

the direction and amount of object displacement based on forces, which in turn are modeled on the basis of physics laws. In an early collective rearrangement approach, a fiber system is generated and, afterwards, fiber intersections are removed depending on the solution of a differential equation. It allows simulation of packings of spherocylinders [74] or ball chains [75]. Schneider and colleagues [76]–[81] transformed this approach into an optimization problem, including curved fibers. In addition, they found that the algorithm performs better when fibers are added to the system sequentially. Venkateshan et al. [72] and Klar et al. [82], [83] propose sedimentation models with collective rearrangement using differential equations.

As another subcategory of collective rearrangement approaches, force-biased approaches are inspired by molecular dynamics. Salnikov et al. [84] propose such a model for cylinders and spheres; Bezrukov & Stoyan [85] introduce a force-biased model for ellipsoids. Altendorf & Jeulin [57] extend this approach to more complex fiber shapes: They consider fibers as ball chains that are generated by a random walk. To remove intersections, repulsion forces act on overlapping balls. To maintain the fibrous structure, recovery forces act between neighboring balls of a chain. Moreover, the recovery forces preserve a prescribed fiber curvature. This approach was extended by Easwaran [61] for infinite fibers and fiber bundles; Chapelle et al. [86] improve the model's runtime by using spherocylinders instead of balls. Note that the molecular dynamics approach is also not limited to collective rearrangement approaches - Kumar et al. [87] develop a fiber model based on the movement paths of charged particles, which are introduced sequentially.

4.2 Altendorf-Jeulin Model

The fiber model by Altendorf & Jeulin [57] specifies a force-biased packing of fibers that are modeled as ball chains. Its starting configuration of fibers is obtained by simulating the fibers independently by a random walk in a closed cubic window $W = [0, w_1] \times [0, w_2] \times [0, w_3]$ with periodic boundary conditions. To preserve the periodic boundary conditions, we use the periodic equivalent d_P of the Euclidean

distance. For $x, x' \in \mathbb{R}^3$ and $i \in \{1, 2, 3\}$, let

$$\Delta_i(x, x') = x'_i - x_i + p_i w_i \quad \text{s.t. } p_i = \underset{p \in \mathbb{Z}}{\operatorname{argmin}} |x'_i - x_i + p w_i| \tag{4.2.1}$$

Then, $d_P(x, x') = \|\Delta(x, x')\|_2$ is the periodic distance function and

$$v_P(x, x') = \frac{\Delta(x, x')}{\|\Delta(x, x')\|_2} \tag{4.2.2}$$

the corresponding direction of the vector between two points.

After the random walk, the fibers may intersect but follow given distributions regarding model features such as fiber size and direction. The force-biased packing removes the intersections, while keeping the model features approximately intact. Note that this packing scheme can also be applied to fiber systems that were generated differently, e.g., with a different random walk [88]. In the following, we will recap the main features of the algorithm.

4.2.1 Formalizing the Fiber System

In the initial fiber system, a single fiber $\mathcal{F} = \{b_1, ..., b_l\}$ is modeled as a chain of l overlapping balls $b_i = (x_i, \mu_i, r), i = 1, ..., l$, of radius r and center $x_i \in \mathbb{R}^3$. In addition, we record the current direction $\mu_i \in S^2$ of the random walk. More precisely, $\mu_i = x_i - x_{i-1}$ is the direction between the last ball and the current ball for $i > 1$; for the start of the random walk in $i = 1$, μ_i indicates the main direction of the whole fiber. In this paper, the radius r of the balls and the chain length l are constant for the sake of simplicity, but they can be randomized (see also [57]). Note that the fiber length ℓ will typically differ from the chain length l.

The point $x_1 \in \mathbb{R}^3$ denotes the starting point of a fiber and can be sampled from a uniform distribution on W. The fiber's main direction $\mu_1 \in S^2$ is sampled from a Schladitz distribution [14] with anisotropy parameter $\beta > 0$. The direction μ_{i+1} is generated following the mvMF$(\mu_1, \kappa_1, \mu_i, \kappa_2)$-distribution. This defines the new position $x_{i+1} = x_i + \frac{r}{2}\mu_{i+1}$. Hence, κ_1 should indicate the reliability of the random walk to the main fiber direction μ_1 and κ_2 the reliability to the last direction μ_i. In other words, κ_1 and κ_2 determine how wavy the fiber can become, see Table 4.2.1.

At the end of the random walk, the fiber is rotated such that its main fiber direction $\bar{\mu} := \frac{x_l - x_1}{\|x_l - x_1\|_2}$ equals μ_1 [57]. In the original implementation, the fibers are

Table 4.2.1: Fibers generated by the Altendorf-Jeulin model for different concentration parameters κ_1, κ_2.

	$\kappa_1 = 1$	$\kappa_1 = 10$	$\kappa_1 = 100$
$\kappa_2 = 1$	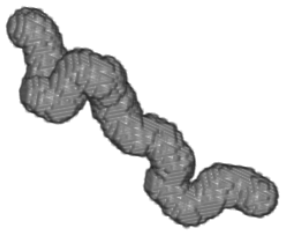		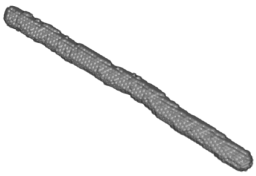
$\kappa_2 = 10$	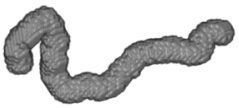	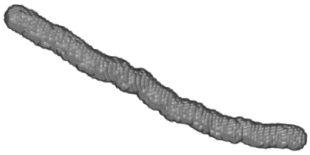	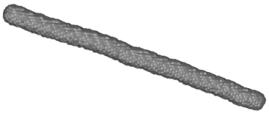
$\kappa_2 = 100$	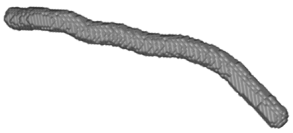	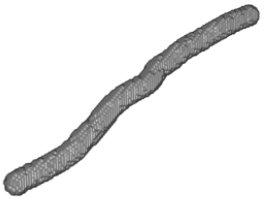	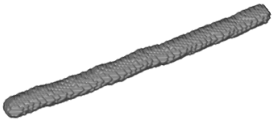

prepacked using a modified version of RSA [12], [67]: Iteratively, the starting point of each fiber is randomly assigned for a given number of trials. The fiber is eventually placed at the position of minimal overlap compared to the other trials. Other than RSA, overlap is not avoided completely, just reduced. This later improves runtime, as fewer intersections must be removed during force-biased packing.

The total fiber system is specified by a graph $\mathcal{S} = (\mathcal{B}_S, \mathcal{F}_S)$, where the node set

$$\mathcal{B}_S = \{b_{1,1}, b_{2,1}, ..., b_{l,1}, b_{1,2}, ..., b_{l,n}\} \tag{4.2.3}$$

contains the balls of the n fibers, and the undirected edge set

$$\mathcal{F}_S = \{\{b_{i,j}, b_{i+1,j}\} | i \in \{1, ..., l-1\}, j \in \{1, ..., n\}\} \tag{4.2.4}$$

contains the connections between the balls as specified by the random walk. As a

consequence, the connected components of $\mathcal{S}$ are equivalent to the fibers. We indicate that balls $b, c \in \mathcal{B}_S$ belong to the same fiber by writing $b \sim_F c$.

4.2.2 Force-biased Packing

To remove the initial fiber intersections, the force-biased packing by Altendorf & Jeulin [57] applies repulsion forces to overlapping balls, see Fig. 4.2.1a. Afterwards, recovery forces restore each fiber's connectedness and features, see Fig. 4.2.1b. This process is repeated iteratively until the forces are small enough.

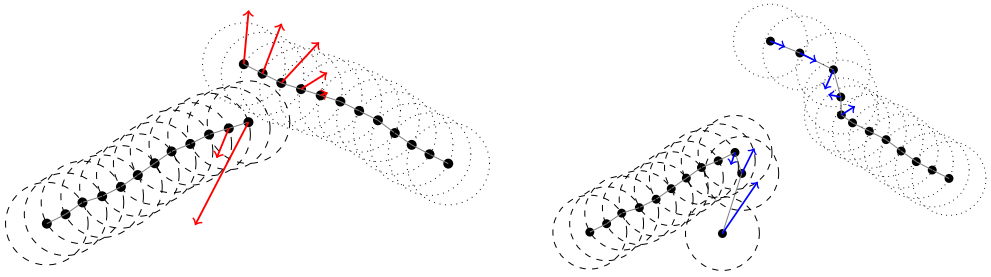

(a) Sketch of repulsion forces acting on intersecting fibers.

(b) Sketch of recovery forces acting on corrupted fibers.

Figure 4.2.1: Sketches of forces in the Altendorf-Jeulin model.

The repulsion force acts on the intersecting balls and moves them apart. An exception pose balls that are "close" within the same fiber as they are designed to overlap: Due to the distance of $\frac{r}{2}$ between subsequent positions in the ball chain, balls inevitably intersect if they are connected by a path consisting of ≤ 4 edges. To allow some room for fiber curvature, Altendorf & Jeulin suggested excluding ball pairs from the repulsion force that are connected by a path of length ≤ 5. For brevity, $b \sim_5 c$ implies that there exists a path of length ≤ 5 between b and c, whereas $b \nsim_5 c$ denotes that such a path does not exist.

In the hardcore case, the strength of the repulsion force F_r depends on the amount of intersection of the balls via

$$I(b, c) = \max\left(0, 2r - d_P(x_b, x_c)\right). \tag{4.2.5}$$

Let the softcore ratio $\tau \in [0, 1]$ describe the amount of intersection allowed, so two ball centers must have at least the distance $2(1 - \tau)r$. Thus, $\tau = 0$ models the

hardcore case, while $\tau = 1$ allows for arbitrary overlap. Then, I generalizes to

$$I_\tau(b,c) = \max\left(0, 2(1-\tau)r - d_P(x_b, x_c)\right). \tag{4.2.6}$$

Its direction is $v(b,c) = v_P(x_b, x_c)$, yielding

$$F_r(b,c) = \mathbb{1}_{b \nsim_5 c} \frac{I_\tau(b,c)}{2} v(b,c). \tag{4.2.7}$$

There are two recovery forces, which only act between neighboring balls within a single fiber: The spring force F_s keeps the ball spacing within the chains intact, whereas the angle force F_a preserves the fibers' bending. The spring force's strength between balls $b, c \in \mathcal{B}_S$ with $\{b,c\} \in \mathcal{F}_S$ depends on their distance, or, more precisely, on the deviation from their initial distance $\frac{r}{2}$:

$$\alpha_d(b,c) = \frac{r}{2} - |x_b - x_c|. \tag{4.2.8}$$

Due to the fibers' chainlike structure, the spring force easily causes ripple effects. In order to reduce them, it further incorporates a smoothing factor that depends on the function α_d, namely

$$f_{\alpha_s,\alpha_e}(\alpha) := \begin{cases} 0, & \text{for } \alpha < \alpha_s \\ \frac{1}{2} - \frac{1}{2}\cos\left(\frac{|\alpha|-\alpha_s}{\alpha_e-\alpha_s}\pi\right), & \text{for } \alpha_s \le \alpha \le \alpha_e \\ 1, & \text{for } \alpha_e < \alpha \end{cases} \tag{4.2.9}$$

for α_s, α_e, see Fig. 4.2.2. For the special case of $\alpha_s = \alpha_e = 0$, we use $f_{0,0}(\alpha) := \mathbb{1}_{\mathbb{R}^+}(\alpha)$.

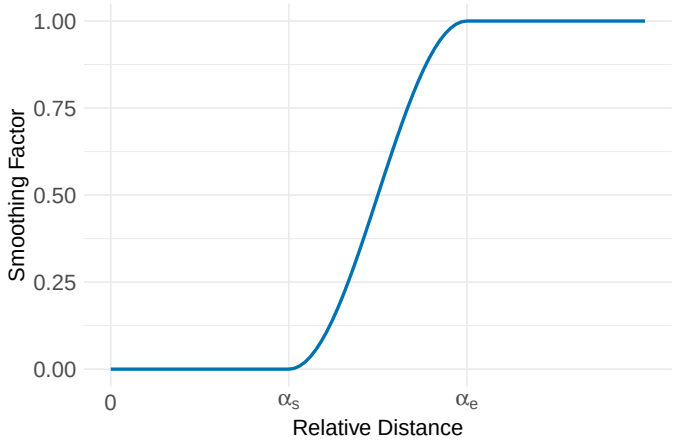

Figure 4.2.2: Plot of the smoothing factor for $0 < \alpha_s < \alpha_e$.

The spring force is then

$$F_s(b,c) = f_{\alpha_s,\alpha_e}\left(2\frac{|\alpha_d(b,c)|}{r}\right)\alpha_d(b,c)v(b,c). \tag{4.2.10}$$

Choose $0 \leq \alpha_s \leq \alpha_e < 1$ as the argument of f_{α_s,α_e} is a relative distance to the initial distance of $r/2$ between b and c, see Section 4.2. Due to the smoothing factor, the force is set to 0 if $\alpha_d(b,c) < \frac{r\alpha_s}{2}$, which keeps the ripple effects of the force on the system small.

The angle force $F_a(b)$ is dependent on the required displacement of balls to preserve the fibers' local curvature. Consequently, it depends on the balls' direct neighbors, just like the spring force. As its definition is rather technical, we refer the reader to the original article [57].

Taken all together, the total force acting on a single ball $b \in \mathcal{B}_S$ is

$$F_{\text{total}}(b) = \sum_{\substack{c \in \mathcal{B}_S \\ c \neq b}} F_r(b,c) + \rho\left(F_a(b) + \sum_{\{b,c\}\in\mathcal{F}_S} F_s(b,c)\right), \tag{4.2.11}$$

where $\rho \in [0,1]$ modulates the composition of repulsion and recovery forces. All parameter choices in this chapter are described and justified in Section 4.4.4.

4.2.3 Extension to Endless Fibers

For some materials, e.g., nonwovens, the fibers are so long in comparison to the observation window W that it is more reasonable to model them as infinite fibers. Easwaran [61] adapted the Altendorf-Jeulin model to endless fibers as follows.

The fibers' position and direction μ_0 are sampled following a Poisson line process, see Section 2.2.4. The ball chain of each fiber is then generated by starting two random walks at the corresponding lines' midpoint $x_0 \in \mathbb{R}^3$ w.r.t. the observation window. One random walk is defined by $x_{i+1} = x_i + \frac{r}{2}\mu_{i+1}$, where the direction μ_{i+1} is generated following the mvMF$(\mu_0, \kappa_1, \mu_i, \kappa_2)$-distribution for $i = 1, ..., l_f$. The random walk stops when it reaches a border of the observation window W. The other random walk is analogously defined, yet in the direction of $-\mu_0$. After both random walks, the fiber is rotated such that its main fiber direction $\bar{\mu}$ equals μ_0.

The total fiber system is then specified as $\mathcal{S}_e = (\mathcal{B}_{S,e}, \mathcal{F}_{S,e})$, where the node set

$$\mathcal{B}_{S,e} = \{b_{-l_{b1},1}, b_{-l_{b1}+1,1}, ..., b_{l_{f1},1}, b_{-l_{b2},2}, ..., b_{l_{fn},n}\} \tag{4.2.12}$$

contains the balls of the n fibers, and the undirected edge set

$$\mathcal{F}_S = \{\{b_{i,j}, b_{i+1,j}\} | j \in \{1, ..., n\}, -l_{bj} \leq i \leq l_{fj}\}\,. \tag{4.2.13}$$

For Poisson lines, periodic boundary conditions are not possible. Therefore, the Euclidean distance function instead of its periodic equivalent is used during packing. To keep boundary effects at bay, the observation window must be extended by at least the fiber thickness. Following Easwaran [61], we implement an extension by 100 units/voxels at each boundary, as this surely exceeds all used values for the fiber thickness in this thesis.

4.3 Fiber Bundles in the Altendorf-Jeulin-Model

The original Altendorf-Jeulin model initially places the fibers independently of each other. In some materials, however, fibers appear in bundles. Nonwovens, for example, can consist of fibers in strands, which may even wrap around each other. The model extension by Easwaran et al. [61] places fibers within a bundle close to each other, removing intersections in a packing step. Gaiselmann et al. [88] place fibers within a bundle parallely, thus avoiding any intersections between them.

Whereas it is possible in nonwovens that fibers pierce through a strand, this is impossible in wood fiber bundles - wood fibers are stiff and appear mostly parallel and tightly packed within a grid structure when they form a bundle, see Fig. 4.3.1. This case is not fully covered by the model extensions described above. We have to ensure parallel and tight packing both during initial fiber generation and during packing. In the following, we propose methods for such bundle generation and force-biased packing by extending the original Altendorf-Jeulin model.

4.3.1 Bundle Generation

Let a bundle $\mathcal{F}_B = \mathcal{F}_{B,1,1} \cup \mathcal{F}_{B,2,1} \cup \cdots \cup \mathcal{F}_{B,n_1,1} \cup \mathcal{F}_{B,1,2} \cup \cdots \cup \mathcal{F}_{B,n_1,n_2}$ consist of $n_1 \cdot n_2$ fibers $\mathcal{F}_{B,j,k}, j = 1, ..., n_1, k = 1, ..., n_2$ in a grid structure with n_1 fibers in

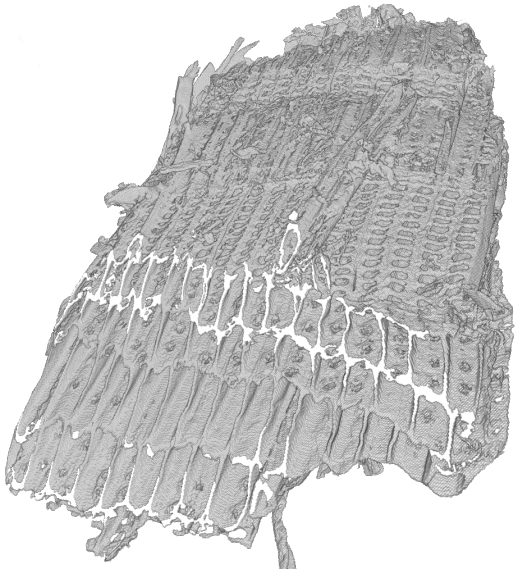

Figure 4.3.1: Reference image of a wood fiber bundle.

direction v_1 and n_2 fibers in direction v_2. The bundle's main direction $\mu_{B,0}$ is the main direction of all its fibers.

For the first fiber $\mathcal{F}_{B,1,1}$, the starting point is $x_{B,1,1,1}$. The position of its subsequent balls $x_{B,1,1,m}, m = 2, ..., l$, follows the random walk as described for the Altendorf-Jeulin model [57]. The fiber $\mathcal{F}_{B,j,k}$ can be considered a displaced copy of $\mathcal{F}_{B,1,1}$, so

$$x_{B,j,k,m} = x_{B,1,1,m} + 2jrv_1 + 2krv_2. \tag{4.3.1}$$

A sketch can be found in Fig. 4.3.2. Note that this definition is by far more meaningful for relatively straight fibers. For highly curvy fibers, the curvature of neighboring fibers would need to be adapted for a smooth, non-overlapping appearance. The set of all balls in bundles is called $\mathcal{B}_{\text{Bundles}}$. In contrast, the set of all balls in single fibers is called $\mathcal{B}_S$. The set of all bundles is called $\mathcal{S}_{Bundles}$.

To generate such a fiber model with bundles, first, the positions of the bundles are sampled using RSA of cylinders. This way, intersections between bundles are avoided. To achieve a higher packing density, RSA of cuboids is possible too, yet at the cost of higher runtime. Next, the fibers of the bundles are inscribed into their corresponding cylinders. Lastly, single fibers are generated with the same process as in the Altendorf-Jeulin model, which allows them to fill empty space between

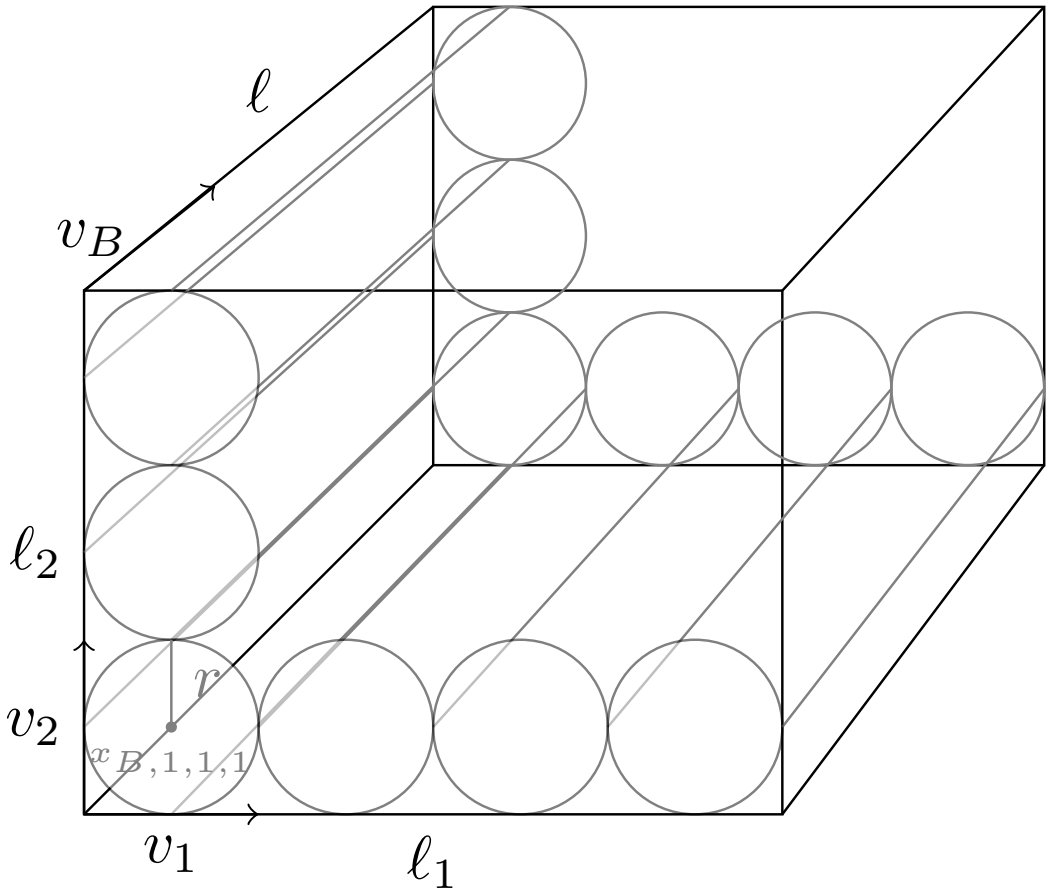

Figure 4.3.2: Sketch of a fiber bundle with 4 fibers along ℓ_1 and 3 fibers along ℓ_2. The remaining 6 fibers are omitted for better visibility.

bundles.

More precisely, let the RSA process place cylinders following a length distribution Ψ_ℓ, a radius distribution Ψ_r, and an orientation distribution Ψ_v. Let cylinder C_B be placed using this RSA process and have length ℓ_B, radius r_B, direction v_B, and center x_B. In the following, we simplify the fiber bundle's shape to a cuboid as we assume close to straight fibers. Moreover, the fibers also have length ℓ_B, and direction $\mu_{B,1,1,1} = \mu_{B,0} = v_B$. Since the largest square to be inscribed in a circle has edge length $\sqrt{2}r_B$, we calculate the number of fibers along edge ℓ_1 as $n_1 = \lfloor \frac{\sqrt{2}r_B}{2r} \rfloor$. The number of fibers along edge ℓ_2, we sample as $n_2 \sim \mathrm{Unif}\,(1, n_1)$. Hence, we set

$$x_{B,1,1,1} = x_B - (n_1 v_1 + n_2 v_2) r - \frac{\ell}{2} v_B. \tag{4.3.2}$$

4.3.2 Bundle Packing

Naively, one could now apply the iterative force-biased of the Altendorf-Jeulin model. This would successfully remove intersections between fibers; however, a single fiber $\mathcal{F}$ piercing through a fiber bundle $\mathcal{F}_B$ would conflict with the bundle's tight structure even if it does not intersect with another fiber itself. Considering the wood fiber bundle in Fig. 4.3.1, this would mean that the fibers would form a hole between them where a single fiber can go through. Considering the usual growth of trees, this behavior is highly unlikely. Therefore, it is necessary to adapt the repulsion force such that the intersection of fibers and bundles is removed too.

The force-biased packing by Altendorf-Jeulin [57] benefits from calculating intersections between balls, as these are very simple to calculate locally and thus allow for fast computation. Due to the cuboidal shape of bundles, however, their repulsion force cannot be calculated from the local overlap of balls. Instead, we need to consider the repulsion force in the context of the whole bundle to make sure the fiber is pushed out of the whole bundle. More precisely, we calculate the repulsion force between a ball c of F and a cuboid B describing the bundle $\mathcal{F}_B$.

Let the ball of fiber $\mathcal{F}$ with center $x_{\mathcal{F},m}$ intersect with the bundle $\mathcal{F}_B$ with center x_B. The local direction of the fiber F here is defined as the random walk direction $\mu_{\mathcal{F},m}$. The shortest path out of the bundle corresponds to the bundle's edge directions. However, pushing the ball along $\mu_{\mathcal{F},m}$ may not remove intersections, as this may simply split the fiber apart, which is counteracted by the recovery force. Hence, we exclude the edge direction of the bundle that aligns the most with $\mu_{\mathcal{F},m}$. More precisely, we exclude $\operatorname{argmax}\{\mu_{B,0}^T\mu_{\mathcal{F},m}, v_1^T\mu_{\mathcal{F},m}, v_2^T\mu_{\mathcal{F},m}\}$. The remaining edge lengths and directions are called ℓ_1', ℓ_2' and v_1', v_2', respectively. For illustration, see Fig. 4.3.3.

The vector length to push the fiber ball out of the bundle in direction $v_i', i = 1, 2$ is

$$\ell_i'' = r + \frac{\ell_i'}{2} - |d_\Delta v_\Delta^T v_i'|, \tag{4.3.3}$$

where $d_\Delta = d_P(x_B, x_{\mathcal{F},m}), v_\Delta = v_P(x_B, x_{\mathcal{F},m})$ are the periodic distance and direction between x_B and $x_{\mathcal{F},m}$. To find the shortest path out of the bundle, find $j =$

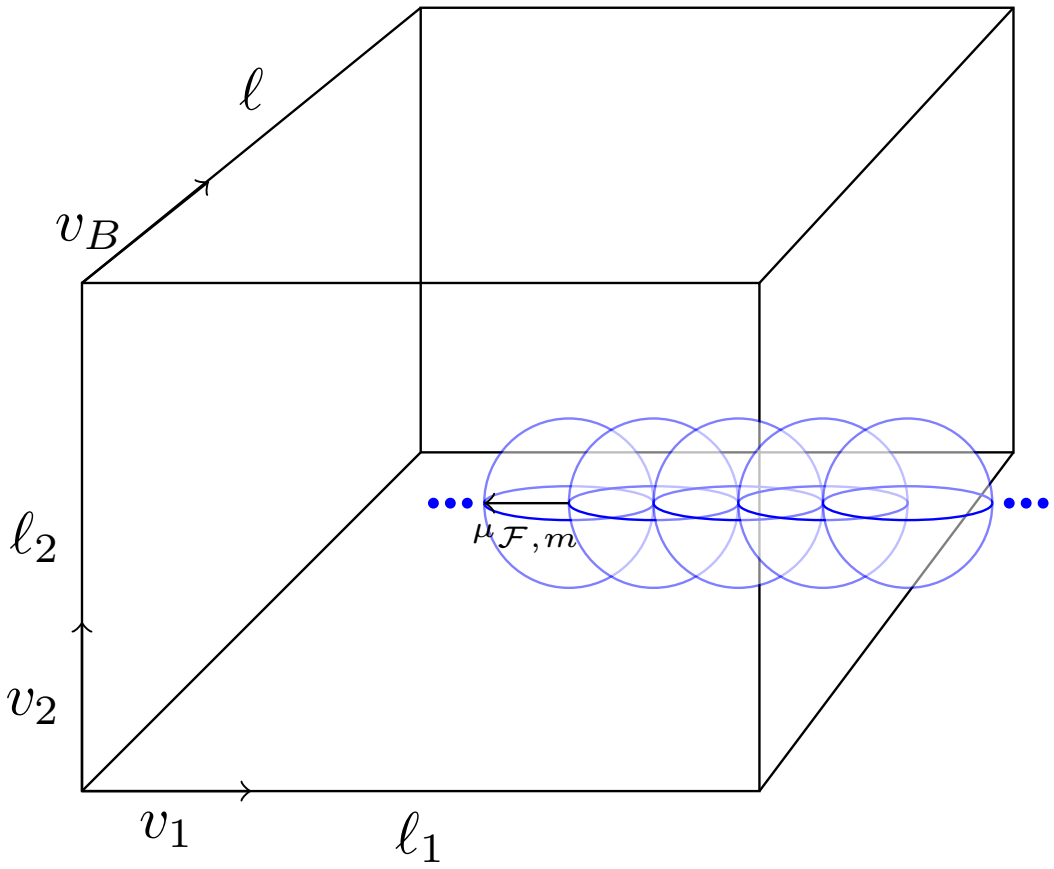

Figure 4.3.3: Sketch of a cuboidal bundle and a fiber part. The fiber direction $\mu_{\mathcal{F},m}$ is close to v_1, so packing forces will act along v_2 or v_B. Note that the remaining fiber balls are omitted for better visibility.

$\text{argmax}_i\{\ell_i''\}$. So the force between a bundle $\mathcal{F}_B$ of cuboid B and a ball $c \in \mathcal{B}_S$ is

$$F_b(\mathcal{F}_B, c) = \begin{cases} \mathbb{1}_{B\cap c\neq\emptyset}\ell_j''v_j', & \text{for } v_\Delta^T v_j' < 0 \\ -\mathbb{1}_{B\cap c\neq\emptyset}\ell_j''v_j', & \text{otherwise} \end{cases} \tag{4.3.4}$$

Taken all together, the total force acting on a single ball $c \in \mathcal{B}_S$ is

$$F_{\text{total}}(c) = \sum_{\substack{d\in\mathcal{B}_S \\ c\neq d}} F_r(c,d) + \rho\left(F_a(c) + \sum_{\{c,d\}\in\mathcal{F}_S} F_s(c,d)\right) + \sum_{\mathcal{F}_B\in\mathcal{S}_{\text{Bundles}}} F_b(\mathcal{F}_B, c). \tag{4.3.5}$$

4.3.2.1 Voxelization

Fig. 4.3.1 shows a bundle of hollow fibers with a rather square-ish cross-section. This shape occurs naturally and is due to the trees' biology: The tunnel is called a *lumen*. This is where the water and nutrients are transported within the tree. The rectangular cross-section ensures that the fibers are packed densely with no further cavities apart from the lumen, whose size is maximized [89].

We incorporate this in the voxelization of the packed fiber model: Instead of balls, we draw cubes of the size such that the original ball is inscribed. To account for the lumen, we draw a tunnel cube with a prescribed wall thickness. The tunnel must be oriented in the local direction of the ball chain, and the rotation of the cube around the longitudinal axis must be consistent within a fiber. For the sake of simplicity, we keep the rotation constant within a fiber, but we sample the cube rotation for each fiber from a uniform distribution $\mathrm{Unif}(0, \pi/2)$.

This approach to modeling the rectangular shape of fibers' cross-sections does not take into account that fibers grow in a more rectangular shape during winter months (also called late-wood) [89], or that the fibers may get torn and squished during the production process. In addition, by taking the actual fiber shape only into consideration after packing the fibers and fiber bundles, we may create an overlap at the cubes' corners of single fibers. However, modifying the Altendorf-Jeulin model to chains of cuboids instead of balls may come at a high computational cost: Intersection calculations are slower than for balls, and the removal of intersections can not only happen through translation, but also through the rotation of cuboids. At this point, though, it is not clear how big the impact of this inaccuracy is. With this in mind, we will study the impact of model decisions on several physical properties in Section 5.3.

4.4 Extending the Altendorf-Jeulin Model to Inter-fiber Contact

In various applications, not only the (lack of) fiber intersections but also the contact between fibers is of interest. For example, inter-fiber contact areas influence the thermal conductivity of fiber systems [1], [4]. Friction, adhesion, and wear along contact points [2] are an essential feature of entangled mechanical networks [90] such as textiles [91]. They must be taken into account to model the significant strain rates and hysteresis phenomena observed in many industrial compaction processes [92]. Micromechanical models, pioneered by Wyk [93], have established non-trivial scaling laws for the effective mechanical response as a function of the fiber density and for the number of contact points with respect to the fiber volume fraction [94].

A common approach [1], [62], [95] to model contact between fibers is the explicit transformation of fiber intersections into contact areas, thus dropping the hardcore condition. Implicitly, Altendorf & Jeulin's force-biased packing [57] achieves the same. However, it has not yet been thoroughly researched how to model inter-fiber contact parametrically.

For cellular fiber networks, i.e., fibers that are connected at their endpoints, inter-fiber contact is modeled more explicitly. Deogekar et al. [96] model them as stochastic Voronoi networks with a connectivity parameter, which is constant for each network. Huisman et al. [97] randomly change the topology using a Monte Carlo minimization scheme. In their earlier work [98], they employ a force-biased approach in which fiber endpoints within a certain distance attract each other. The network topology, especially the number of contact points, is controlled via the force strength.

4.4.1 Analytical Description for Fiber Contact

To incorporate contact in the fiber packing, we extend Altendorf & Jeulin's [57] fiber packing by an additional force, the contact force F_c. This force will be applied to balls that are close enough to establish contact. Before properly defining F_c, we need to specify what it means that two fibers are in contact.

4.4.1.1 Algorithmic Notions of Contact and Closeness

Let the balls $b, c \in \mathcal{B}_S$ belong to different fibers, i.e., $b \nsim_F c$, then

- b and c intersect if $|x_b - x_c| < 2r$.
- b and c are in (perfect) contact if $|x_b - x_c| = 2r$.
- b and c are d-close for $d \geq 0$ if $|x_b - x_c| \leq 2r + d$, denoted as $b \overset{d}{\sim} c$.

These relations are depicted in Fig. 4.4.1.

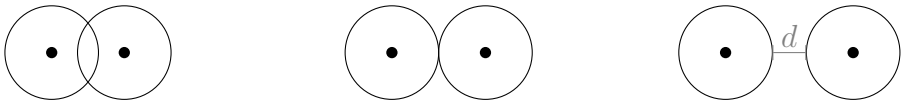

(a) Intersecting balls. (b) Balls in perfect contact. (c) d-close balls.

Figure 4.4.1: Sketch for the degrees of closeness on the level of balls.

Based on this contact notion, we can define a graph $\mathcal{C}_d = (\mathcal{B}_S, \mathcal{E}_d)$ that describes the d-closeness between the fibers with the undirected edge set

$$\mathcal{E}_d = \left\{ \{b, c\} | b, c \in \mathcal{B}_S, b \nsim_F c, \text{ and } b \overset{d}{\sim} c \right\}. \tag{4.4.1}$$

In Fig. 4.4.2, the blue lines depict the set $\mathcal{E}_0$, that is, ball pairs in perfect contact.

Apart from the contact on the level of balls, we are also interested in the contact on the level of fibers. As shown in Fig. 4.4.2, one contact area between fibers may consist of multiple ball pairs that are in contact. Using only the contact notion on the level of balls would therefore be counterintuitive as it confounds the number of ball pairs with the number of fibers. Moreover, it is dependent on the balls' size, and one ball may be in contact with more than one other ball. As a solution, we understand the contact area between two fibers as the ball chain sections where their balls are in contact. Since the ball chains are described by the edges in $\mathcal{F}_S$, it seems natural to extend $\mathcal{E}_d$ by the balls' incident edges w.r.t. $\mathcal{F}_S$. In Fig. 4.4.2, they are depicted by red lines. To formalize this concept, we extend the edge set $\mathcal{E}_d$ as follows:

$$\bar{\mathcal{E}}_d = \mathcal{E}_d \cup \{ \{b, c\} \in \mathcal{F}_S | \exists a \in \mathcal{B}_S \text{ s.t. } \{b, a\} \in \mathcal{E}_d \vee \{a, c\} \in \mathcal{E}_d \}. \tag{4.4.2}$$

A connected component of the graph $\bar{\mathcal{E}}_d$ may contain more than two fibers; these we call *clots* to discriminate them from (pairwise) contact areas between two fibers. By counting the connected components, we will later report the number of contacts per unit volume as estimator for the contact intensity, as well as the number of contacts and the number of clots per fiber as estimators of the contact and clot density, respectively.

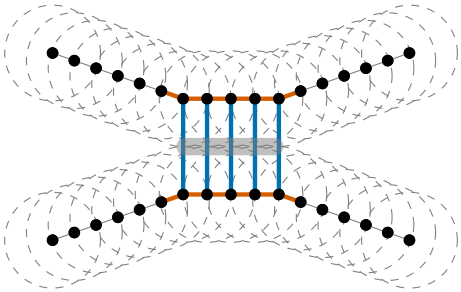

Figure 4.4.2: Sketch for the contact areas between fibers. Blue indicates the contact between balls as described by $\mathcal{E}_0$. Red indicates the ball chain sections creating the contact as described by $\bar{\mathcal{E}}_0 \backslash \mathcal{E}_0$. The gray area indicates the intuitive contact area.

Now that we have introduced a notion to quantify contact and closeness in the Altendorf-Jeulin model, we can turn to creating more contact. To do so, we identify suitable balls, to which we later apply the contact force. In the style of Huisman et al. [98], we identify such balls depending on their closeness: The balls $b, c \in \mathcal{B}_S, b \nsim_F c$, are *contact candidates* w.r.t. the *interaction distance* $\varepsilon > 0$ if $b \overset{\varepsilon}{\sim} c$. The set of contact candidates w.r.t. the interaction distance ε is then $\mathcal{E}_\varepsilon$. We deliberately include balls that are already in contact as contact candidates since these are supposed to stay in contact.

However, applying the contact force to all contact candidates in $\mathcal{E}_\varepsilon$ may be computationally expensive for a large ε. The forces might even be conflicting (see Fig. 4.4.3). Therefore, we reduce the contact candidates to a "shortlist" S_ε, such that every ball belongs to at most one candidate pair per fiber pair. To achieve faster convergence, we keep the edge in the shortlist that has the minimal distance compared to incident edges. To formalize this, we define the set of incident edges

$$\mathcal{I}_\varepsilon(\{b, c\}) = \{\{d, e\} \in \mathcal{E}_\varepsilon | e \sim_F c\} \cup \{\{c, e\} \in \mathcal{E}_\varepsilon | e \sim_F b\}. \tag{4.4.3}$$

This set contains all edges in $\mathcal{E}_\varepsilon$ that belong to the node b or the node c. If there exists an edge $\{b, c\} \in \mathcal{E}_\varepsilon$, then $\mathcal{I}_\varepsilon(\{b, c\})$ consists of all its incident edges. We define the shortlist as

$$\mathcal{S}_\varepsilon = \left\{ \{b, c\} \in \mathcal{E}_\varepsilon | \{b, c\} = \underset{\{d,e\} \in \mathcal{I}_\varepsilon(\{b,c\})}{\operatorname{argmin}} \|d - e\| \right\}. \tag{4.4.4}$$

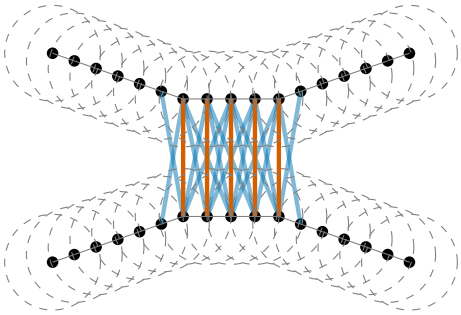

Figure 4.4.3: Sketch for the contact candidates (indicated by blue lines) and shortlist (indicated by red lines) for the interaction distance $\varepsilon = \frac{3}{4}r$.

4.4.2 Contact Force

We extend Altendorf & Jeulin's [57] fiber packing by one more force, namely the *contact force* F_c. It exists between two shortlisted contact candidates $\{b, c\} \in \mathcal{S}_\varepsilon$. We aim to move the balls such that they are in perfect contact, i.e.

$$|x_b - x_c| = 2r, \tag{4.4.5}$$

so the force depends on the difference between the ideal and actual distance. Further, there is no force necessary when the balls are already intersecting. With this, we define the *effective distance*

$$d_E(b, c) := \max(0, d_P(x_b, x_c) - 2r). \tag{4.4.6}$$

Note that d_E differs from I, which we introduced for the repulsion force in Section 4.2, by exchanging subtrahent and minuend, which makes them complementary: Whereas the repulsion force pushes intersecting balls apart until they are at most in contact, the contact force draws balls together until they are at least in contact.

In analogy to the repulsion force, the contact force has the direction $v(c,b)$. Hence, we propose the contact force

$$F_c(b,c) = \frac{1}{2} d_E(b,c) v(c,b) \tag{4.4.7}$$

for $\{b,c\} \in \mathcal{S}_\varepsilon$.

In some applications, such as nanotube composites, fibers start to interact before being in physical contact [99]. In this case, it makes sense to consider d_c-close balls as being in contact for a given contact distance $d_c > 0$. Consequently, the balls $b, c \in \mathcal{B}_S, b \nsim_F c$ are contact candidates w.r.t. the interaction distance $\varepsilon > 0$ if $|x_b - x_c| \leq 2r + d_c + \varepsilon$. One can reason similarly when discretizing the fiber system, e.g. for voxelized images. There, depicting distances below the voxel size is usually impossible.

For a contact distance $d_c > 0$, we have additional leeway for balls to be considered in contact without intersection. It seems natural to use $\max(0, d_P(x_b, x_c) - (2r + d_c))$ as the effective distance, thus only aiming for d_c-closeness instead of perfect contact. However, this also lowers the force strength and may consequentially lead to slower convergence. Therefore, we incorporate the smoothing factor f_{0,d_c} as introduced for the recovery force in Section 4.2. In total, we generalize the contact force to

$$F_c(b,c) = \frac{f_{0,d_c}\left(d_E(b,c)\right)}{2} d_E(b,c) v(c,b) \tag{4.4.8}$$

for $(b,c) \in \mathcal{S}_\varepsilon$.

4.4.3 Synopsis of the Contact Packing Scheme

In our contact packing scheme, we first run the regular force-biased packing by Altendorf & Jeulin [57]. This way, the fiber system is already (nearly) free of intersections and thus possesses lower inherent forces. If this system does not have the desired amount of inter-fiber contacts yet, we increase the contact by applying the packing incorporating the contact force. We explain this modified packing scheme in the following. A pseudocode is provided in Algorithm 8.

In the first step of our contact-modified fiber packing, we identify contact candidates $\mathcal{E}_\varepsilon$ for a given interaction distance $\varepsilon > 0$, which we then reduce to the

shortlist S_ε, such that every ball belongs to only one candidate pair per fiber pair, see Section 4.4.1.1. In this configuration, we iteratively apply the force

$$F_{\text{total, c}}(b) = \sum_{\substack{c \in \mathcal{B}_S \\ c \neq b}} F_r(b,c) + \rho_R \left(F_a(b) + \sum_{\{b,c\} \in \mathcal{F}_S} F_s(b,c) \right) + \rho_C \sum_{\{b,c\} \in \mathcal{S}_\varepsilon} F_c(b,c), \tag{4.4.9}$$

to every ball $b \in \mathcal{F}_S$ until convergence. The stop criterion is specified in Section 4.4.4. Note that $\rho_R, \rho_C \in [0,1]$ are factors modulating the composition of forces analogously to ρ in Section 4.2.

Some shortlisted candidates $(b,c) \in \mathcal{S}_\varepsilon$ can cause conflicting forces in the fiber system even after fiber packing. This can, for example, happen in denser fiber systems when the contact forces in different contact components "pull" fibers in directions that conflict unresolvably with their repulsion and recovery forces. Note that a similar phenomenon has already been observed by Altendorf & Jeulin [57], where they compare it with the jammed state [75]. We remove such shortlisted candidates and apply the force again iteratively until termination. If this does not achieve the desired amount of contact, we can repeat the procedure with an increased interaction distance ε. Shortlisted candidates are classified as causing conflicting forces if for $a = b$ or $a = c$ the force length $\|F_{\text{total, c}}(b)\|$ exceeds a specified threshold $t > 0$.

The same scheme can be applied to the bundle packing approach in Section 4.3. Here, contact should only be established between single fibers: Contact between fibers within the fiber bundle exists per definition of the fiber bundle. Creating more contact between single fibers and bundles would require further work to calculate contact areas appropriately, which is outside the scope of this thesis.

4.4.4 Implementational Details

The original fiber packing by Altendorf & Jeulin [57] stops when the sum of total forces $\left\| \sum_{b \in \mathcal{B}_S} F_{\text{total}}(b) \right\|$ falls below a certain threshold. For the contact-modified fiber packing, however, we decided to stop the packing when the sum of total forces decreases by less than a specified relative amount. This has the advantage of being independent of parameters like the number of fibers or window size, as is the case

Algorithm 8 Contact Packing Scheme

Require: $d_c \geq 0$, interaction distance ε

```
generate a starting configuration of fibers
run the Altendorf-Jeulin fiber packing with F_total
calculate the contact candidates E_ε
calculate the shortlist S_ε
while !(stop criterion) do
    run fiber packing with F_total, mod
end while
if some candidates in S_ε cause conflicting forces then
    remove candidates from S_ε
    while !(stop criterion) do
        run fiber packing with F_total, c
    end while
end if
```

in the implementation by Altendorf & Jeulin [57]. We chose a limit of 0.001% in the present thesis. To ensure termination, we stop the packing when the number of iterations exceeds 1 000.

As a reminder, one iteration of fiber packing classicly encompasses the calculation of forces on the fiber system and, subsequently, the corresponding repositioning of balls. In this thesis, we choose $t = 0.1$ to remove shortlisted candidates that cause unresolvable forces in the fiber system, as it provides a trade-off between accuracy of the fibers' curvature by removing unresolvable forces on the one hand and achieving high contact on the other hand. It is justified by the sensitivity study reported in Section 4.5.6. Alternatively, the interaction distance could be chosen higher to achieve the same amount of contact, but this would cause a higher runtime in return.

For the realizations in this thesis, we use $\rho = \rho_R = \rho_C = 0.5$, indicating equal strength for both recovery and contact forces. For the spring force, we use $\alpha_s = 0.05$ and $\alpha_e = 0.1$. Unless indicated otherwise, the softcore ratio is $\tau = 0$ and the contact distance $d_c = 0$. This conforms to the parameters used by Altendorf & Jeulin [57],

thus allowing for direct comparison.

To detect contact candidates and intersecting balls, we follow Altendorf & Jeulin [12] and use the particularly fast implementation by Mościński et al. [100]. They divide the window into subwindows with a side length (s_x, s_y, s_z). To find contact or intersection candidates faster, every subwindow is given a list of balls. Notably, a subwindow's list contains both the balls whose center is in the subwindow and the balls whose center is in the subwindow's neighboring subwindows. This way, only balls in a subwindow's list need to be checked for contact candidacy or overlap. For a maximal interaction distance of $\varepsilon_{\max}$, we use a subwindow size of at least $\max(2.5r, (2 + \varepsilon_{\max})r)$. We calculate the connected components of $(\mathcal{B}_S, \bar{\mathcal{E}}_\varepsilon)$ using UnionFind [101].

4.5 Experimental Validation

In this section, we examine the performance of our packing scheme regarding the features of the fiber system when increasing contact. We implemented the scheme in C++ using and extending the library MAVIlib [45], which Fraunhofer ITWM develops and maintains. For further speed-up, we parallelized the calculation of forces using OpenMP. Experiments were run on the ITWM Beehive Cluster using an Intel(R) Xeon(R) CPU E5-2670 0 @ 2.60GHz, 125 GiB RAM, and the GNU compiler GCC 11.5.

4.5.1 Experimental Setup

For Boolean models, the intensity of inter-fiber contacts depends on the fibers' length, radius, intensity, and direction distribution, see Eq. 2.2.10. We expect a similar dependency for non-overlapping fibers. Therefore, we vary these parameters in our experimental setup as well. For image sizes of 64 to 640 voxels per edge, we study

- short, medium, and long fibers, namely fibers with an aspect ratio $a := \frac{\ell}{2r}$ of $a = 10, 30, 50$; the radius stays constant at $r = 2$.

- low, medium, and high volume fractions, namely $V_V = 10\%, 20\%, 30\%$. Note

that fiber systems with even higher intensities will be packed quite densely already; in this case, increasing the contact density is less meaningful.

- the direction distribution from aligned over the uniform distribution to girdle distributions, namely we use the Schladitz distribution with $\beta = 0.1, 0.5, 1.0, 2.0, 3.0$.

As a packing parameter, we choose the interaction distances $\varepsilon = 0.1, 0.2, ..., 0.5, 1.0$.

In this setup, we use a medium curvature of $\kappa_1 = 10, \kappa_2 = 100$, the softshell ratio $\tau = 0$, and the contact distance $d_c = 0$ as default parameters. To study the scheme's accuracy when varying these parameters, we further study the cases of low curvature, namely $\kappa_1, \kappa_2 = 100$, high curvature, namely $\kappa_1, \kappa_2 = 10$, and very high curvature, namely $\kappa_1, \kappa_2 = 1$, for medium aspect ratio and medium volume fraction. Note that varying these parameters for all parameter combinations discussed above would result in three times the runtime and computing resources, which is not merely tedious but also unsustainable given the necessary energy consumption. All used parameter combinations can be found in Table A.1.1 in the Appendix.

4.5.2 Representative Volume Element and Runtime

The representative volume element (RVE) of a microstructure is the volume V that is considered large enough to be statistically representative. Note that the RVE depends not only on the microstructure, but also on the investigated property Z. This means, for example, that the RVE for the volume fraction and the thermal conductivity can differ for the same microstructure. Moreover, it is not always computationally feasible to generate a microstructure that is large enough. Therefore, the concept is generalized to a combination of the size and number of realizations to be representative of the underlying microstructure, where a notion of precision describes the degree of representativity. This way, it can be calculated, for example, how many small realizations are necessary when large realizations are computationally prohibitive. The following computations are based on the assumption of ergodicity [102].

In the present work, we are interested in the properties that describe the phenomenon of forming contact and clotting. We denote by λ_c the mean number of inter-fiber contact points per unit volume, i.e., the intensity of inter-fiber contacts.

For Boolean models with (fiber) intensity λ_F, this corresponds to the intersection intensity as

$$\lambda_c \approx 4\lambda_F^2 r\ell \left[\ell f_\psi + \pi r(g_\psi + 1)\right], \tag{4.5.1}$$

see Eq. 2.2.10. The expected number of contacts per fiber is $\lambda_{cF} = 2\frac{\lambda_c}{\lambda_F}$. Analogously, the mean number of clots per fiber $\lambda_{clF} = 2\frac{\lambda_{cl}}{\lambda_F}$, where λ_{cl} is the expected number of clots per unit volume. For algorithms whose runtime depends on the volume, the decision on the chosen size and the corresponding number, or vice versa, to achieve an RVE is a tradeoff depending on the runtime. In the following, we will refer to this as the (RVE) size-number combination. To make the decision based on runtime considerations, we will not only carry out an RVE estimation following Kanit et al. [102], but we will also report the observed runtime to justify our chosen size-number combination. More precisely, we carry it out on the 'most average' case of our experimental setup (see Section 4.5.1), namely medium fiber aspect ratio $a = 30$, volume fraction $V_V = 20\%$, isotropic orientation ($\beta = 1.0$), and a curvature of $\kappa_1 = 10, \kappa_2 = 100$ under the interaction distance $\varepsilon = 0.3$. We generate 50 realizations each for the window edge lengths $s = 64, 128, 256, 384, 512, 640$, yielding the volumes $V = 64^3, 128^3, ..., 640^3$. For each parameter combination, we estimate the expected number of contacts per fiber[1] λ_{cF}, and the expected number of clots per fiber λ_{clF}. For each property $Z = \lambda_{cF}, \lambda_{clF}$, we fit a model of the variance $D_Z^2(V)$ as

$$D_Z^2(V) = KV^{-\alpha}, \quad K, \alpha > 0, \tag{4.5.2}$$

see also Dirrenberger et al. [103]. The factor $K^{\frac{1}{3}}$ is a multiple of the generalized integral range, which can be interpreted as the scale of the phenomenon [102], which in our case is forming contact and clotting. Define the relative precision φ for the estimation of Z as $\varphi = \frac{2D_Z(V)}{\bar{Z}\sqrt{n}}$. For a given φ, we can estimate the required number of simulations when using volume V to get overall representative information, short RVE number as [103]:

$$n_{\mathrm{RVE}}(Z, V) = \frac{4}{\varphi \bar{Z}} \frac{K}{V^\alpha}. \tag{4.5.3}$$

[1]The contact intensity λ_c is, in this case, only a scaled version of the expected number of contacts per fiber λ_{cF}; therefore, we omit it here.

The runtime of the contact packing is proportional to the volume, see Fig. 4.5.1 with a slope of 1.641×10^{-7}min/voxel. It has a runtime of roughly 10 min for size 384, which is acceptable when considering 'many' parameters in a simulation study, as we do in this section 4.5. Note that this runtime increases with the volume fraction, or rather, the number of fibers in a window of constant size.

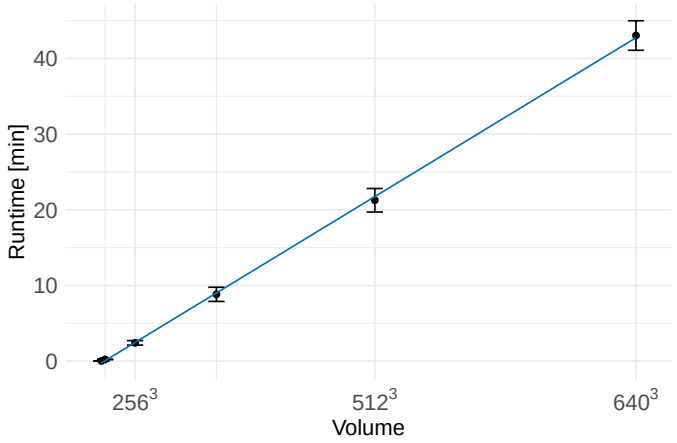

Figure 4.5.1: Plot for the runtime depending on the window size for medium fiber length and volume fraction, $\beta = 1.0$ and the curvature $\kappa_1 = 10, \kappa_2 = 100$. The scale of the window size is transformed cubically (corresponding to the volume). Bars indicate the standard deviation, the line in blue indicates a fitted model.

For each characteristic Z and volume V, we fit a model of the variance D_Z^2 to the simulation results and report the RVE number in Table 4.5.1 using a relative precision of 1%. For the expected number of contacts per fiber λ_{cF}, we found $K_{cF}^{\frac{1}{3}} \simeq 51.65$ and $\alpha_{cF} \simeq -0.9954$. For the the expected number of clots per fiber λ_{clF}, we found $K_{clF}^{\frac{1}{3}} \simeq 14.91$ and $\alpha_{clF} \simeq -1.0020$. Notably, both $K_{cF}^{\frac{1}{3}}$ and $K_{cl}^{\frac{1}{3}}$ are smaller than the fiber length of 120. Plots of $D_Z^2(V)$ can be found in Fig. A.2.1 in the Appendix.

In the following, we will generate 4 realizations on a window size of 384 for each parameter combination: As Table 4.5.1 shows, only 4 realizations of window size 384 are necessary to achieve a relative precision of 1%. This yields the lowest runtime, see Fig. 4.5.1, in comparison to the other RVE size-number combinations, while having a larger window size than the longest fiber length $\ell = 200$.

Table 4.5.1: The number of realizations necessary for a given volume and characteristic for a relative precision of 1%.

Volume	λ_{cF}	λ_{cl}
64^3	420	797
128^3	46	87
256^3	6	11
384^3	2	4
512^3	1	2
640^3	1	1

4.5.3 Contact Intensity Achieved Depending on the Interaction Distance

The contact packing does not contain the contact intensity as a direct input parameter; instead, it contains the interaction distance, which does not directly translate to the contact intensity. Therefore, we investigate the relationship between the interaction distance and contact intensity in this subsection. Results are given in Fig. 4.5.2.

The contact intensity is not quite linear w.r.t. the interaction distance, but Fig. 4.5.2 provides an indication of what to expect for similar setups. For each parameter combination, the contact intensity is relatively constant for $\beta \geq 1.0$ but generally smaller for $\beta < 1.0$. A likely reason for this is that for isotropic and girdle distributions, i.e., $\beta \geq 1.0$, there are more balls of different fibers in the neighborhood of each ball. For more aligned distributions, i.e., $\beta < 1.0$, the neighboring balls are more likely to belong to the same fiber, which yields larger contact areas instead. Validating this conjecture will be part of future work. Notably, this effect reverses for low volume fractions, short fibers, and high interaction distances. Since the fibers are smaller, the likelihood that balls belong to different fibers increases again. This translates to more fibers clustering, as is shown in Fig. 4.5.3.

For long fibers and low volume fraction, the chosen interaction distance barely achieves an increase in contact intensity. This is most likely due to the distance between single fibers. This also conforms with the high parameter accuracy in this

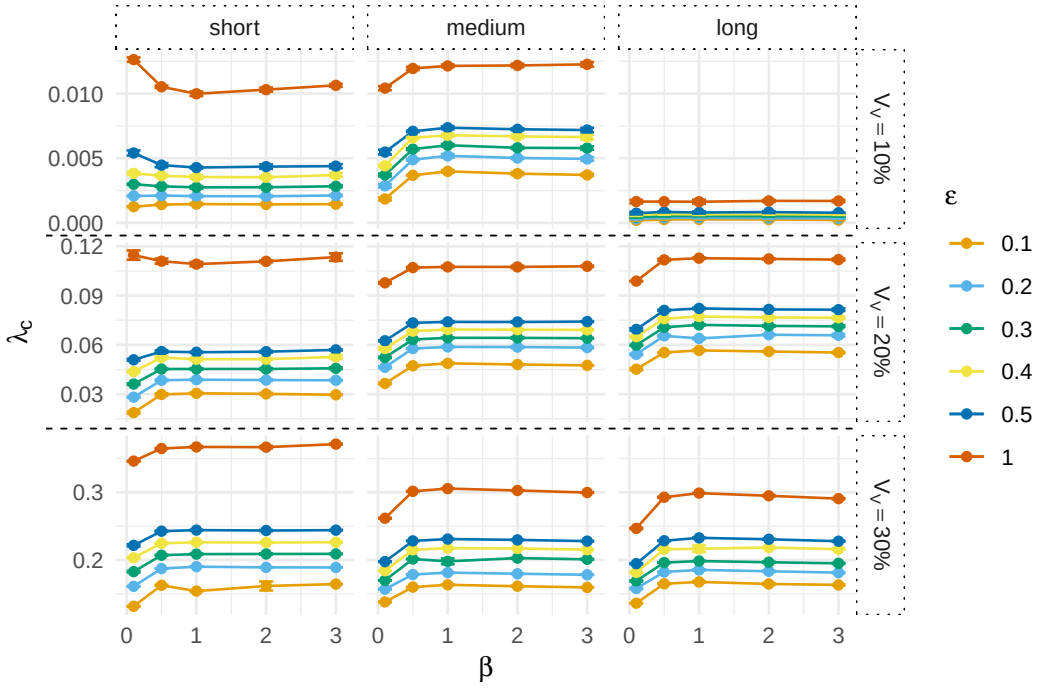

Figure 4.5.2: Plot of the contact intensity λ_c w.r.t. the parameter of the orientation distribution for varying interaction distance ε (in colour) for the experimental setup described in Section 4.5.1. Note that $\kappa_1 = 10, \kappa_2 = 100$.

case, see Section 4.5.5. Similarly, curvy fibers result in slightly higher contact and clot densities than their straighter counterparts, see Fig. A.3.1 and A.3.2. Very curvy fibers, on the other hand, yield far lower contact and clot densities, see Fig. A.3.3. A possible explanation is that the high curvature leads to more ball intersections when fibers do intersect, thus creating stronger repulsion forces.

4.5.4 Achieved Contact Intensity Compared to Toll's Formula

In order to compare the contact intensity between both packing algorithms and Toll's formula [20], see Eq. 2.2.10, we study the realizations for each parameter combination proposed in the section above with the interaction distance $\varepsilon = 1.0$. We estimate their contact intensity $\hat{\lambda}_c$, both after the Altendorf-Jeulin packing and the contact packing.

Fig. 4.5.4 shows the results for the intensities. The already low contact intensities

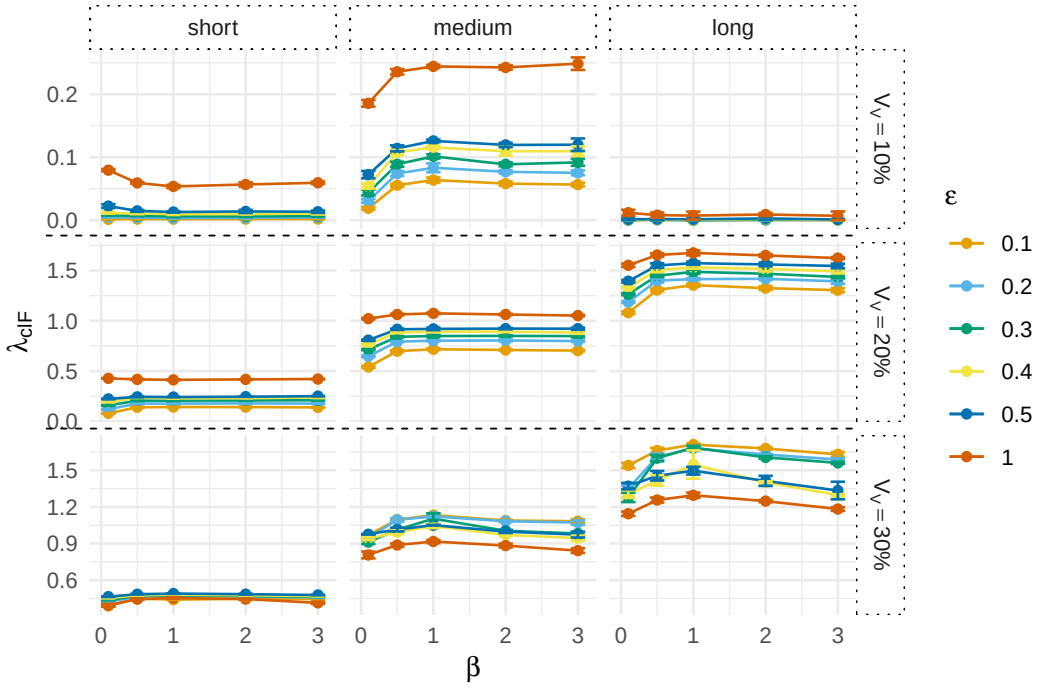

Figure 4.5.3: Plot of the clot density λ_{cl} w.r.t. the parameter of the orientation distribution for varying interaction distance ε (in colour) for the experimental setup described in Section 4.5.1. Note that $\kappa_1 = 10, \kappa_2 = 100$.

for the low volume fraction mostly stay below Toll's intersection intensity. This may be improved by omitting the prepacking in the Altendorf-Jeulin model. Yet for most other cases, the contact intensity can be raised above Toll's intensity. For high volume fraction and at least medium aspect ratio, the contact intensity even exceeds Toll's intensity after the Altendorf-Jeulin packing.

The probability distribution for the number of contacts per fiber is represented in Fig. 4.5.5 for the medium aspect ratio $a = 30$, a volume fraction $V_V = 20\%$, an isotropic orientation distribution, and an interaction distance of $\varepsilon = 1.0$. Results obtained for the Altendorf-Jeulin and our contact models are compared with the distribution obtained for the Toll model (2.2.10). This distribution is obtained in a similar way as the mean number of contact points and follows a Poisson law in the case of an isotropic distribution of orientation [58]. Furthermore, we fit the numerical results obtained for the Altendorf-Jeulin and contact models with Poisson laws.

The Toll model gives a Poisson distribution with a mean of 6.6 contacts per fiber.

In the AJ model, it has a mean of roughly 5 contact points and is very close to a Poisson distribution. In the contact model, the mean is about 8.2, which is much higher. Furthermore, the contact distribution is more narrow than in a Poisson distribution. Note, however, that the Toll model gives relevant estimates for intersecting fibers. The absence of interpenetrations in the contact model is a considerable constraint that induces in particular repulsion effects and anti-correlations not taken into account in the Toll model.

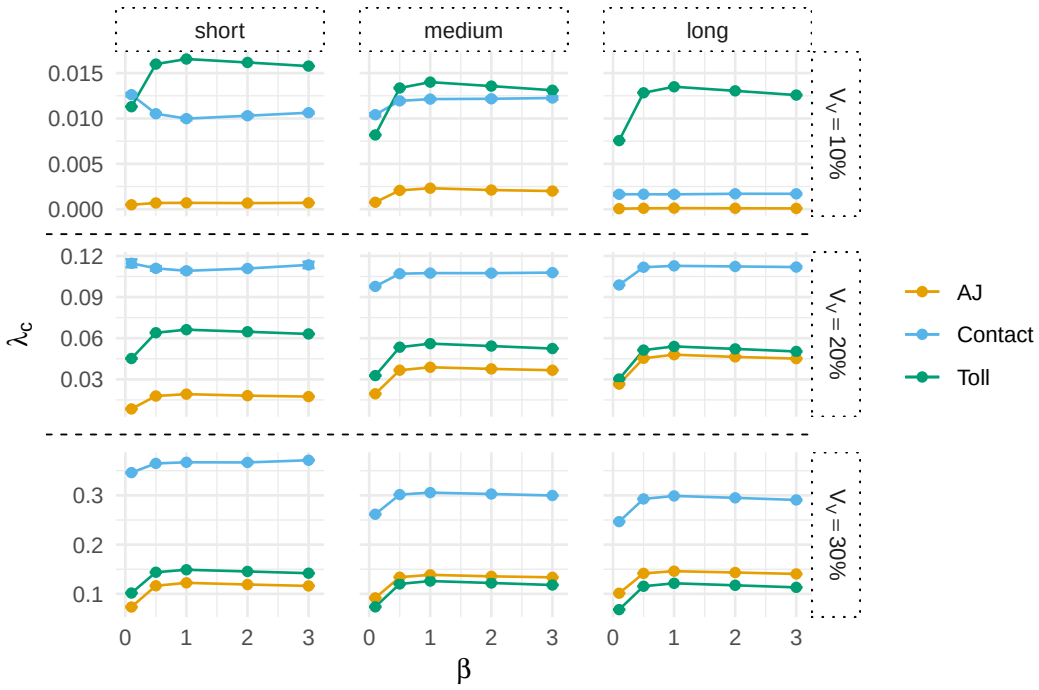

Figure 4.5.4: Plot of the contact intensity of the Altendorf-Jeulin model, the contact model, and the analytically determined formula by Toll. Note that $\kappa_1 = 10, \kappa_2 = 100$.

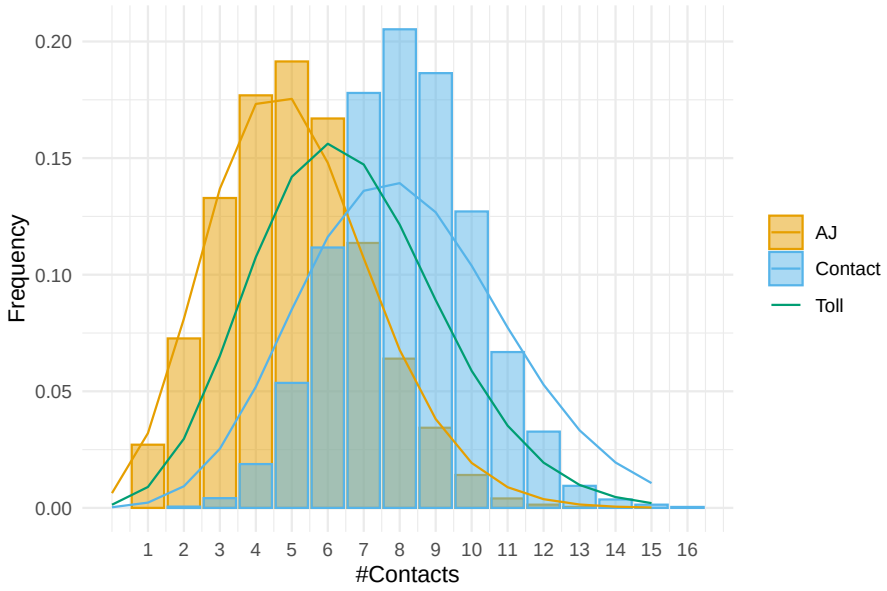

Figure 4.5.5: Plot of the distribution of the number of contacts of individual fibers for the Altendorf-Jeulin model and the contact model (colored bars). Solid lines represent Poisson distributions with the same mean as that of the two models (left and right) as well as that predicted by the Toll model (in-between). Note that $\kappa_1 = 10, \kappa_2 = 100$.

We additionally tested the contact positions for complete spatial randomness (CSR). For testing, we use the global envelope test [104], [105] with 99 Monte-Carlo simulations of point patterns, $\alpha = 0.05$, and the K- and G-function [106]. CSR is rejected for both the contact positions after Altendorf-Jeulin packing and after contact packing. The corresponding plots do not give a clear indication whether the contact positions form a regular or clustered process, see Fig. 4.5.6, Fig. 4.5.7, and Fig. A.3.8. This behavior barely changes for different lengths, volume fractions, or direction distributions. We would have expected a regular process, where there can be no contact areas closer than the fiber radius. Yet surprisingly, this case does occur, see Fig. 4.5.6. Such cases are expected to become rarer with stricter stop criteria, yet at the expense of higher runtimes.

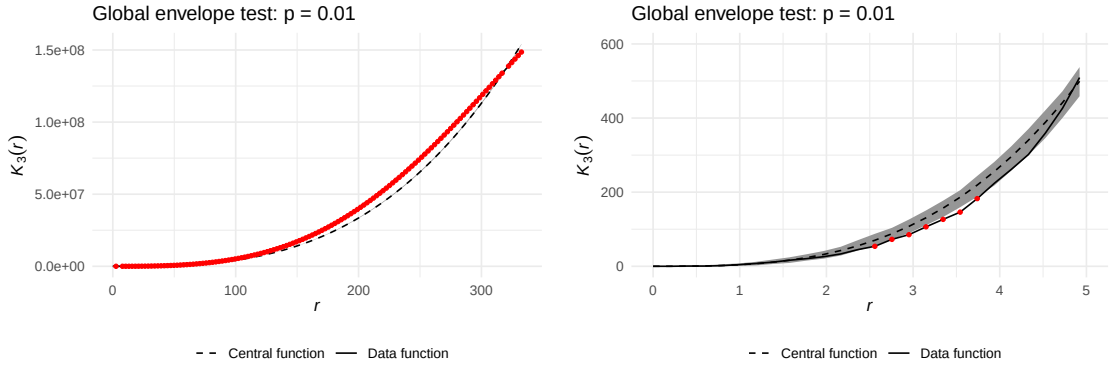

Figure 4.5.6: Plot of the spatial statistic K regarding the contact positions in the Altendorf-Jeulin model. The right plot reveals the behavior for $r \leq 5$, i.e., the order of magnitude of the fiber thickness. The gray area indicates the global envelope of the test statistic. Red dots indicate function points that lie outside the envelope. Note that $\kappa_1 = 10, \kappa_2 = 100$.

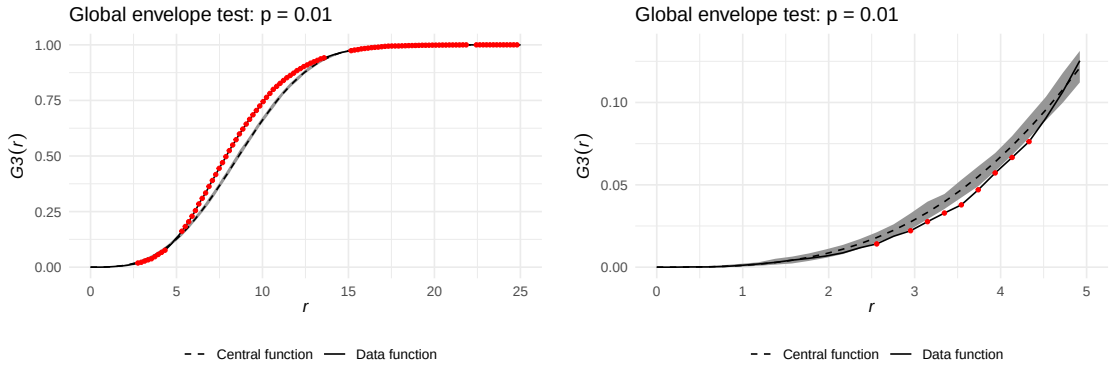

Figure 4.5.7: Plot of the spatial statistic G regarding the contact positions in the Altendorf-Jeulin model. The right plot reveals the behavior for $r \leq 5$, i.e., the order of magnitude of the fiber thickness. The gray area indicates the global envelope of the test statistic. Red dots indicate function points that lie outside the envelope. Note that $\kappa_1 = 10, \kappa_2 = 100$.

4.5.5 Accuracy Results

In order to evaluate the accuracy of our packing scheme, we estimate the direction parameter $\hat{\beta}$ and the curvature parameters $\hat{\kappa}_1$ and $\hat{\kappa}_2$ as proposed and implemented by Altendorf [57]. We do this both after fiber generation but before packing, after packing with the Altendorf-Jeulin method, and after contact packing with interaction distance $\varepsilon = 0.1$. We report their relative deviation from the original input parameters as an indicator of accuracy. Note that 0 indicates high accuracy due to no deviation, and 1 indicates low accuracy due to high deviation. Being particularly interested in any possible inaccuracy introduced by the contact packing steps, we also compare the deviation between the Altendorf-Jeulin packing and the contact packing.

All methods (fiber generation, Altendorf-Jeulin packing, contact packing) show acceptable accuracy for the fiber direction parameter β for values of $\beta \geq 0.5$, see Fig. 4.5.8: The relative deviation from the input parameter is below 0.1. For smaller values, the relative deviation rises up to 0.6, even more so for shorter fibers. In absolute terms, $\beta = 0.1$ only deviates up to 0.06 (units), which is acceptable. The estimated value of the curvature parameters κ_1 and κ_2, however, shows rather high inaccuracy: Whereas κ_2 has a relative deviation from the input parameter below just 0.2, the relative deviation can even rise up to even 0.75 for the parameter κ_1, see Fig. 4.5.9. This is especially pronounced for shorter fibers. Curiously, the parameter estimations are more accurate after packing. This phenomenon has already been observed by Altendorf&Jeulin [57]. Note that it is already alluded to in previous works that the curvature parameters are qualitatively meaningful, but their quantitative estimation is "not highly accurate" [12]. Interpreting the estimated curvature parameters qualitatively, the parameter deviation does not change the fiber shape drastically, see Table 4.2.1.

Fig. 4.5.10 shows the relative deviation of the contact packing to the Altendorf-Jeulin packing. Whereas the direction parameter β shows only very small deviation, i.e., it stays highly consistent, one can observe higher deviation for the local curvature κ_2. This is an intuitive result considering that the contact packing creates contact by attracting balls of fibers that are close to each other, which likely increases local curvature (corresponding to lower values). Nevertheless, the deviation of the

curvature parameters should be taken with a grain of salt, given the inaccuracy of their estimation observed above. Fig. A.3.4 presents the mean absolute angular error (MAAE, see Section 3.2) between original angles of incident edges and the angles after packing. With a maximum of 2°, they indicate high accuracy independent of the estimation of the parameters κ_1, κ_2.

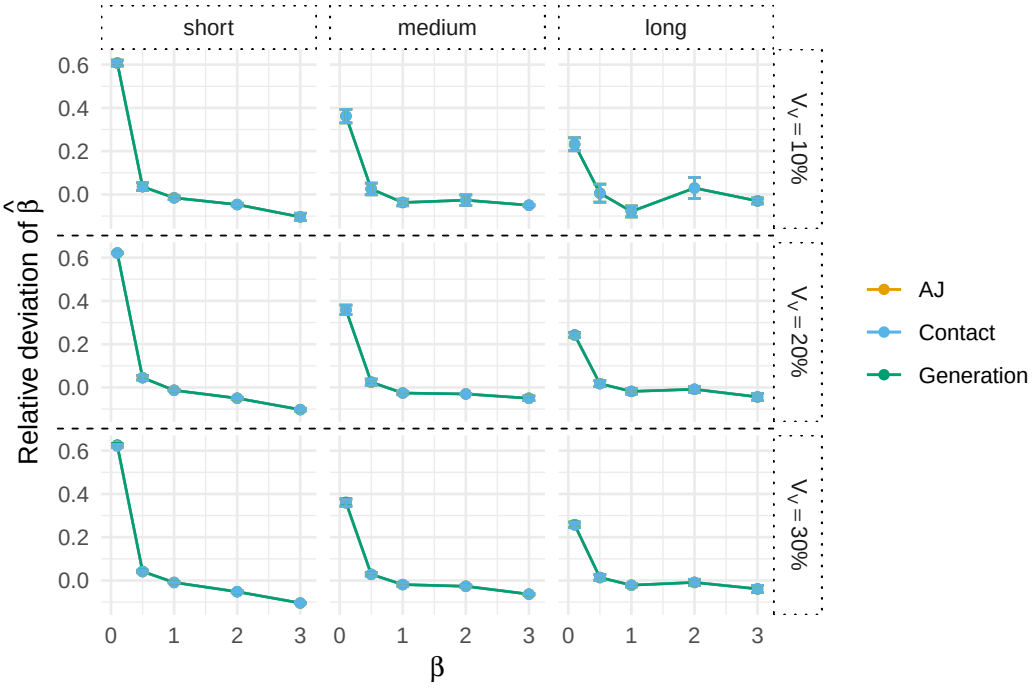

Figure 4.5.8: Plots of the deviation from the direction parameter β relative to the input value. The estimated values of β for the contact packing and the Altendorf-Jeulin packing correspond so closely to the values upon fiber generation that the plots overlay each other. Bars indicate standard deviations, but are often not visible because they are so low. Note that low deviation around 0 indicates high accuracy, whereas high values indicate low accuracy. Note that $\kappa_1 = 10, \kappa_2 = 100$.

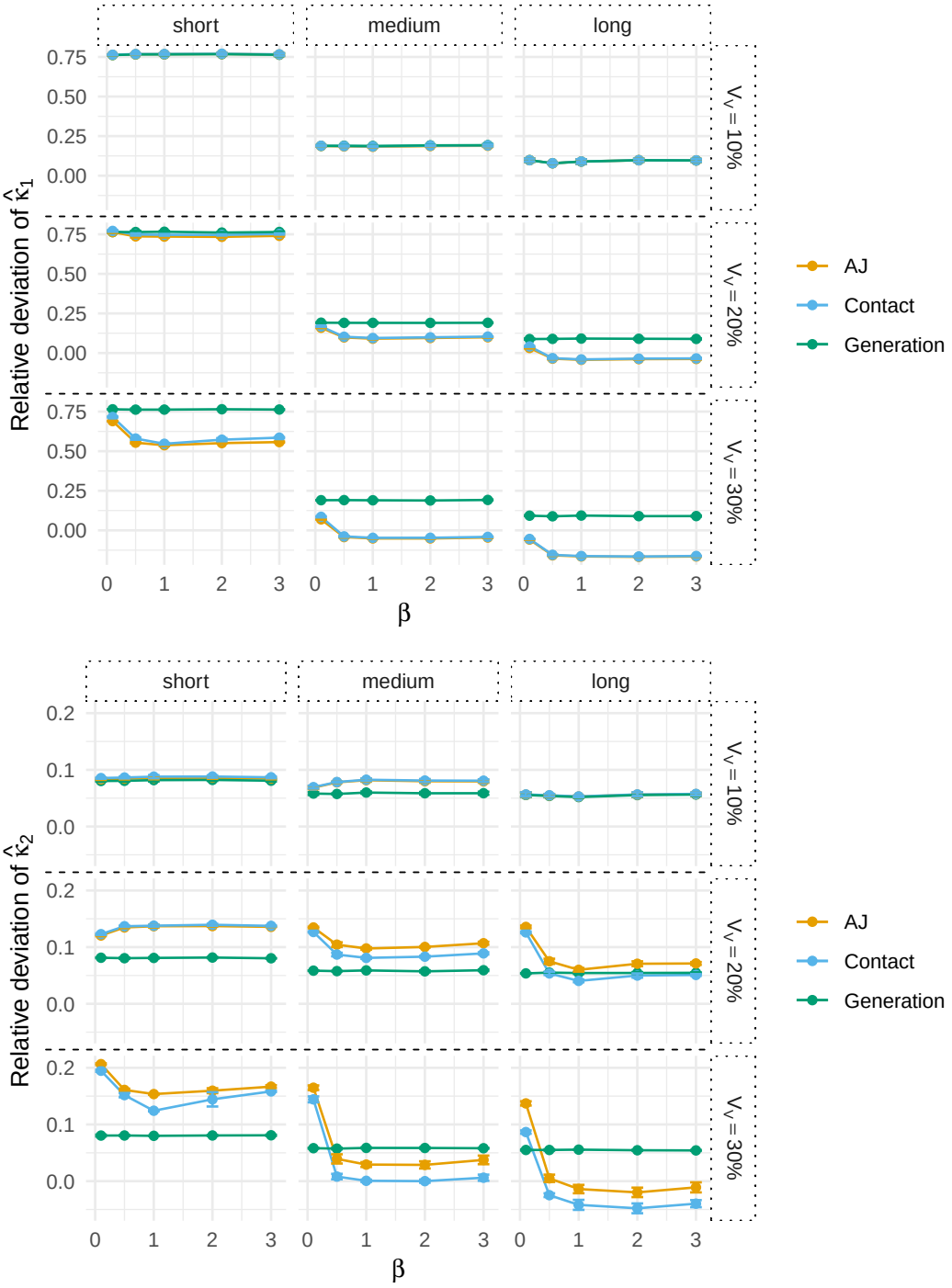

Figure 4.5.9: Plots of the deviation of the curvature parameters $\kappa_1 = 10$ and $\kappa_2 = 100$ relative to the input values after fiber generation, Altendorf-Jeulin packing, and contact packing each. Bars indicate standard deviations, but are often not visible because they are so low. Note that low values for the absolute deviation around 0 indicate high accuracy, whereas high values indicate low accuracy.

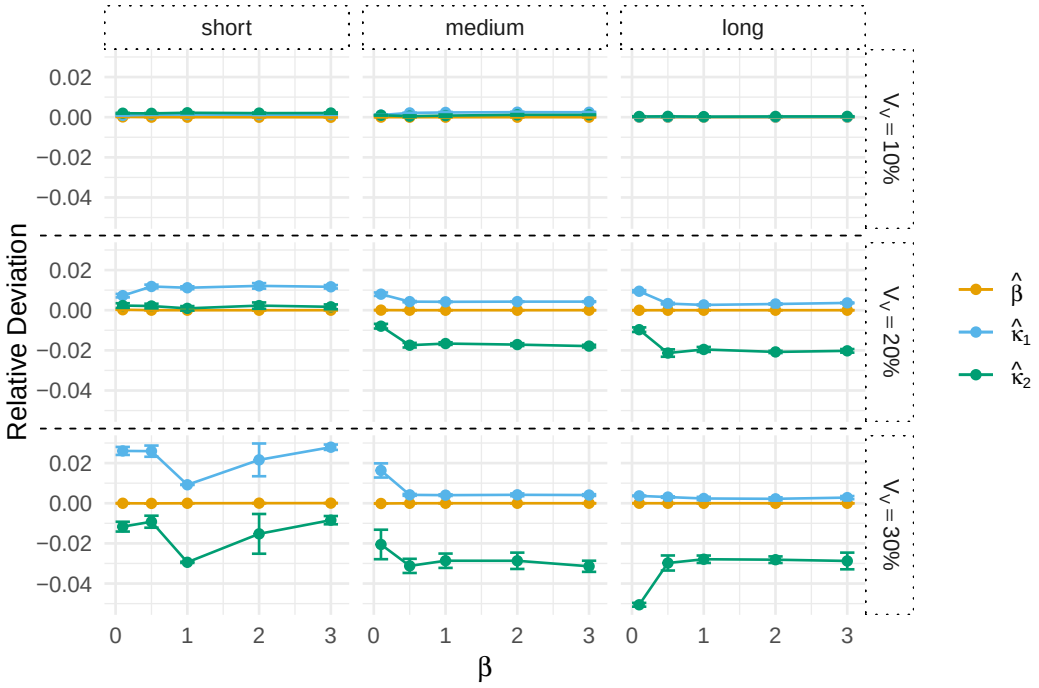

Figure 4.5.10: Deviation of the estimated parameter values of the contact model relative to the Altendorf-Jeulin model. Bars indicate standard deviations, but are often not visible because they are so low. Note that low values for the absolute deviation around 0 indicate high accuracy, whereas high values indicate low accuracy. In this setup, the curvature parameters are $\kappa_1 = 10, \kappa_2 = 100$.

4.5.6 Sensitivity of the Threshold Parameter t

As stated in Section 4.4.4, we use a threshold of $t = 0.1$ to remove shortlisted candidates that cause conflicting forces. Long fibers ($a = 50$) in high volume fractions ($V_V = 30\%$) are most likely to contain such due to the amount of available contact candidates and conflicts within the same fiber. Hence, we choose this case and $\beta = 1.0$ as the test case of a sensitivity study for the threshold.

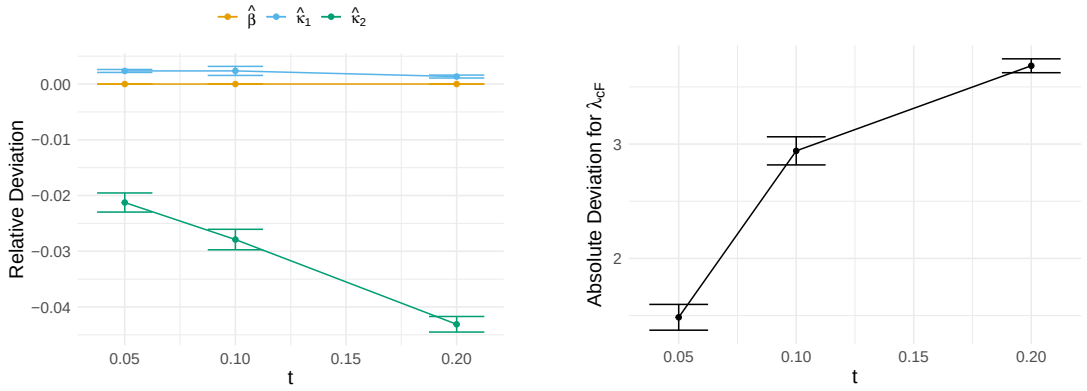

(a) Deviation of the estimated parameter values of the contact model relative to the Altendorf-Jeulin model.

(b) Plot of the difference between the number of contacts per fiber λ_{cF} between the contact packing and the preceding Altendorf-Jeulin packing.

Figure 4.5.11: Sensitivity study of the threshold t to remove shortlisted candidates. Bars indicate standard deviations. Note that low values for the absolute deviation around 0 indicate high accuracy, whereas high values indicate low accuracy. In this setup, the aspect ratio is $a = 50$, the volume fraction $V_V = 30\%$, $\beta = 1.0$, $\varepsilon = 0.1$, and the curvature parameters are $\kappa_1 = 10, \kappa_2 = 100$.

The influence of the choice of t on the deviation of the direction and curvature, as well as the difference of λ_{cF} for the contact model to λ_{cF} for the Altendorf-Jeulin model are represented in Fig. 4.5.11. The strongest relative deviation is visible for the curvature parameter κ_2. For $t = 0.05, 0.1$, this deviation is kept below $3\,\%$, whereas for $t = 0.2$, it rises above $4\,\%$. For λ_{cF}, on the other hand, we observe that the contact packing increases λ_{cF} by roughly 3 contacts in comparison to the preceding Altendorf-Jeulin packing for $t = 0.1$, while it does not increase by more

than 4 contacts for $t = 0.2$. For $t = 0.05$, λ_{cF} increases only by roughly 1.5 contacts, which indicates a slower increase for $t > 0.1$ than for $t < 0.1$. Overall, this shows that $t = 0.1$ indeed allows for a trade-off between the accuracy of parameters, which stays below 3 % of deviation, and maximizing λ_{cF}.

4.6 Discussion and Conclusion

Despite the relevance of inter-fiber contacts when simulating physical properties of fiber systems, there exists little research on parametrically modelling fiber systems including inter-fiber contact. Therefore, we extend the force-biased model by Altendorf & Jeulin [57] to a model where the contact between fibers can be explicitly increased. For this, we have developed algorithmic notions of contact and closeness. To increase the number of contacts, we have added another force to the model by Altendorf & Jeulin that creates contact between fibers that are close enough.

We have shown that our model indeed increases the number of contacts in comparison to the Altendorf-Jeulin model while maintaining similar accuracy to other parameters of the fiber system. Moreover, we compared the number of contacts in the algorithmic hardcore models with the intersection intensity of the Boolean model, finding that the contact intensity of the contact model exceeds the intersection intensity of the Boolean model for volume fractions above 20 %.

Studying the accuracy of the curvature parameter was severely limited since, to our knowledge, no accurate estimators for the parameters κ_1 and κ_2 exist [57]. We employed the measure of MAAE to study the deviation of the fiber curvature in comparison to the originally generated fibers. This measure has the advantage of being independent of the random walk used to generate the fibers.

The runtime of the present model is proportional to the volume, see Section 4.5.2. For a window size of 2048^3, which is typical in industrial settings, we expect a runtime of roughly 22 h in our setup. In comparison, the conductivity solver implemented in the commercial product GeoDict [107] has a runtime of 16 h using 4 threads on the same image size to calculate thermal or electrical conductivity [108]. This indicates that, even though the fiber model does not scale very well having a runtime

proportional to the volume, its runtime is still in the same range as that of physical computations.

To show the relevance of the models introduced in this section for real-world applications, we will apply them to real data in the following chapter. In particular, we simulate physical properties for Boolean models, for the original Altendorf-Jeulin model, the bundle model from Section 4.3, and the contact model from Section 4.4 in Section 5.3 to compare the influence of model decisions on simulation results.

Chapter 5

Applications of Fiber Models

While the fiber models in Chapter 4 have already been motivated by applications, the focus of that chapter was on the underlying algorithms and experimental accuracy. In this chapter, however, we want to present real-world application of the fiber models. In the first section, we present the modeling procedure of a nonwoven material for a biomedical application based on analyzing CT images. Based on the results, we fit an Altendorf-Jeulin model with Easwaran's extension to endless fibers [57], [61]. In Section 5.2, we fit a Boolean model to the solid structure of wood-fiber insulation boards in order to study their behavior regarding thermal conductivity for different microstructural arrangements. Lastly, we study the impact of model decisions on physical simulations: Inspired by wood-fiber boards, we model fiber systems as Boolean models, Altendorf-Jeulin models, the bundle extension, and contact models. After running thermal and mechanical simulations on them, we study the impact of the model decisions on the results.

5.1 Nonwoven Scaffolds

A common injury of the knee joint is the lesion of the meniscus. Especially inner lesions are currently mostly treated by removing the meniscal tissue surgically, which leads to further injury to the surrounding tissue, increasing the likelihood of developing osteoarthritis. Alternatively, the meniscal tissue can regrow within a scaffold that is inserted into the lesion, thus protecting the surrounding tissue

similar to the native meniscus. This treatment is, however, not yet fully restoring the mechanical properties of the meniscus; in addition, it is very expensive. Therefore, we study an alternative scaffold material that consists of fibers, namely a nonwoven. Colleagues model the growth behavior in this material and its biomechanical behavior. To facilitate this, we fit a fiber direction distribution from CT scans of the scaffold material. On that basis, we create a geometric fiber model. Apart from the fiber model, this work has already been published in Surulescu et al. [109]. In this section, we focus on the fiber analysis and modeling of the work. Simulation results can be found in the original paper.

5.1.1 Material & Imaging

The scaffold is a nonwoven made from polyethylene terephthalate (PET) fibers with a diameter of 17 µm and a length of 60 mm. For the fabrication procedure, see the original paper [109].

Six cylindrical scaffold samples were scanned by micro computed tomography using a Skyscan1172 device. A source voltage of 40 kV and a current of 250 µA were used. The angular step width in the rotation was 0.3 degrees, resulting in 1 202 projection images. The voxel spacing is 3.98 µm. These CT images, however, suffered from an artifact as shown in Fig. 5.1.1. Therefore, the scans sufficed for the estimation of fiber directions, but the artifacts' effect on the estimated pore size was unclear.

A cut-out from one of these samples was scanned once more in the Tomo-Scope L 300 and the microfocus X-ray tube µF240T-80 with a voltage of 90 kV, a current of 267 µA, 3 000 projections, and a voxel spacing of 2.45 µm [110]. This scan allows for higher resolution, see Fig. 5.1.2. However, we trade the higher resolution in for the previously large field-of-view. Moreover, this scan contains even stronger, yet more localized artifacts, see Fig. 5.1.3.

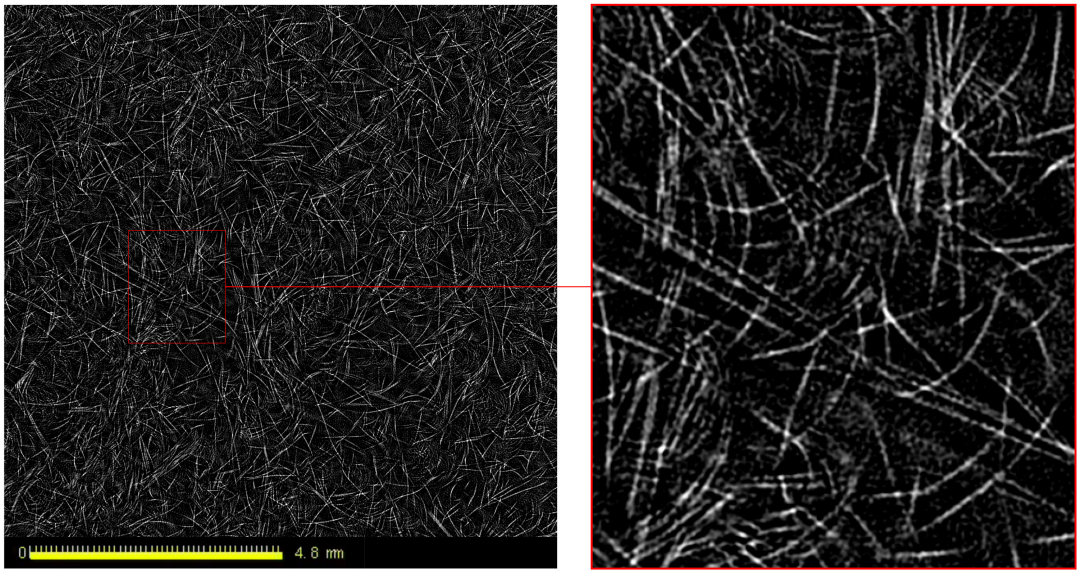

Figure 5.1.1: Sectional image of the CT scan of sample 1 (left) with a size of $2\,600 \times 2\,600$ pixels, i.e., approx. $10.35\,\text{mm} \times 10.35\,\text{mm}$. The area marked by a red box is magnified 5 times (right) to enhance the visibility of the fiber structure.

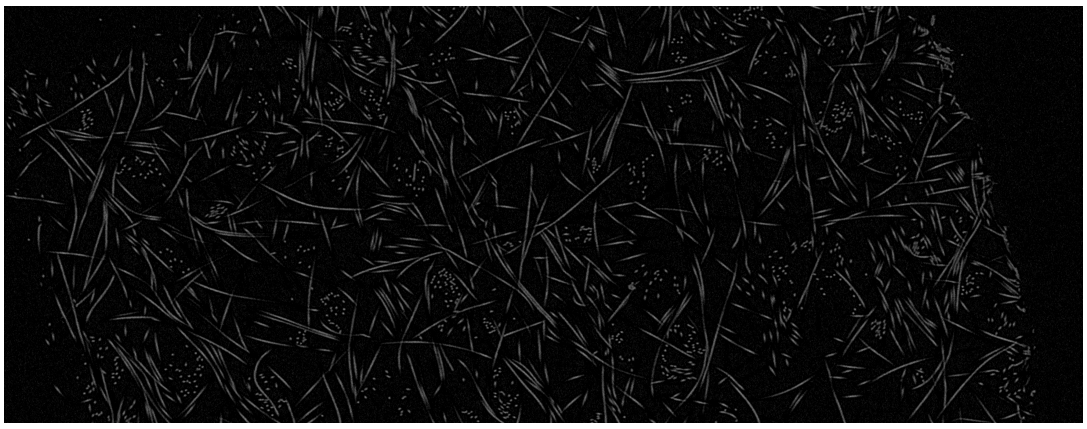

Figure 5.1.2: Sectional image of the CT scan of higher resolution with a size of $3\,535 \times 1\,366$ voxels, i.e., approx. $8.66\,\text{mm} \times 3.35\,\text{mm}$.

5.1.2 Image Segmentation

5.1.2.1 SkyScan

We cropped the images from the SkyScan such that the cuboid field-of-view is entirely inside the cylindrical specimen (approx. $2\,600 \times 2\,600 \times 300$ voxels with a spacing of $3.98\,\mu\text{m}$). A sectional image is shown in Fig. 5.1.1. In a preprocessing step, we smoothed the CT image with a Gaussian filter (filter mask size: $7 \times 7 \times 7$ voxels, blur parameter $\sigma = 6.0$, reflective edge treatment) to remove noise while preserving edges. These parameters were chosen according to the fiber diameter, which corresponds to approximately 6 voxels.

To achieve a coarse segmentation of the fiber system, we deployed Otsu's thresholding method [111] with a factor of 1.25. For further refinement, we applied a median filter (filter mask size: $3 \times 3 \times 3$ voxels, reflective edge treatment), then a morphological closing operation (structuring element size: $5 \times 5 \times 5$ voxels), and, subsequently, the median filter again. Lastly, we removed connected components of sizes smaller than 50 voxels because these are likely too small to constitute single fibers. After segmentation, we observed volume fractions around 13 %.

5.1.2.2 TomoScope

For the part of sample 1 that was scanned with high resolution ($2.45\,\mu\text{m}$), a different type of artifact occurred, see Fig. 5.1.3. This type of artifact may be due to dust. We removed them as follows: We binarized the image with a lower threshold of 2 200, opened it with a cube of size 3 voxels, dilated it further with a ball of diameter 3 voxels, and labeled the result images. We removed the 4 largest connected components and dilated the rest individually. With the complements of these images, we masked the original CT scan. To binarize the fibers from the artifact-free image, we thresholded the image using the Otsu factor [111] multiplied by 1.25. Subsequently, we applied a median filter of size 3 voxels. This yielded a volume fraction of 9.5 %, which is considerably lower than in the SkyScan-scans.

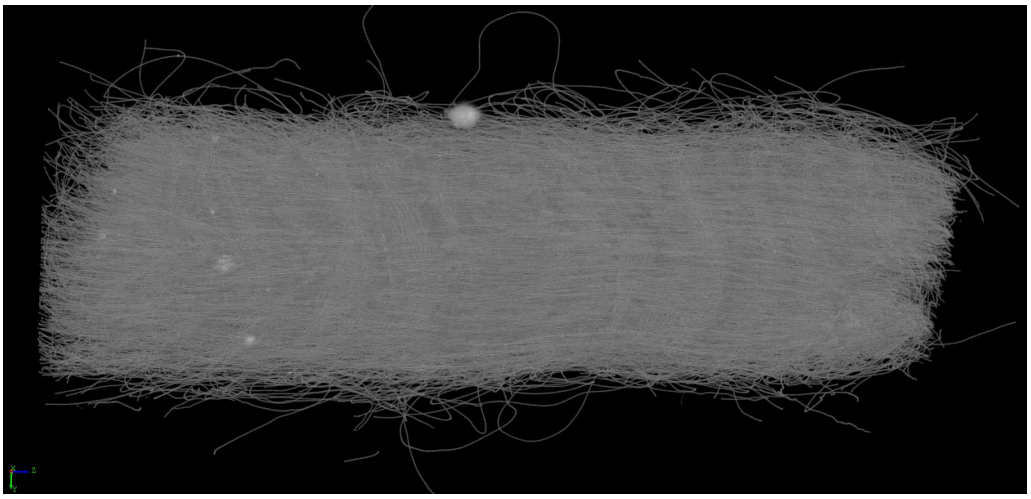

(a) The artifacts in a projection image.

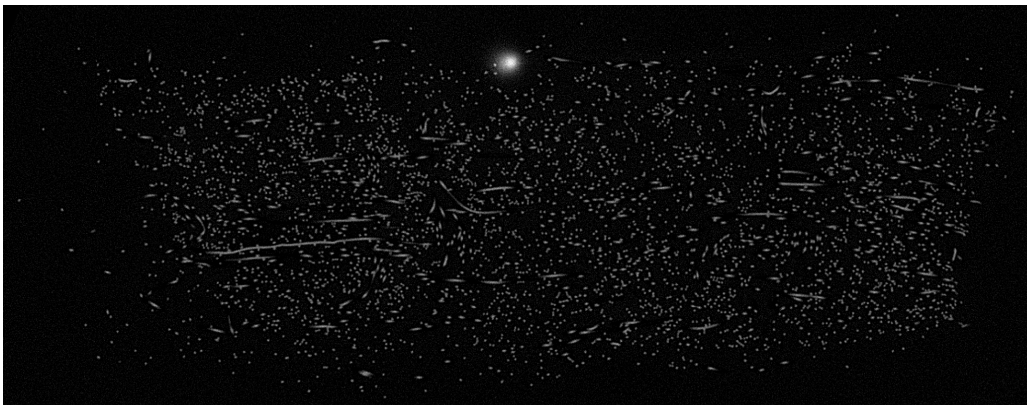

(b) An artifact in sectional x-y-slice 87.

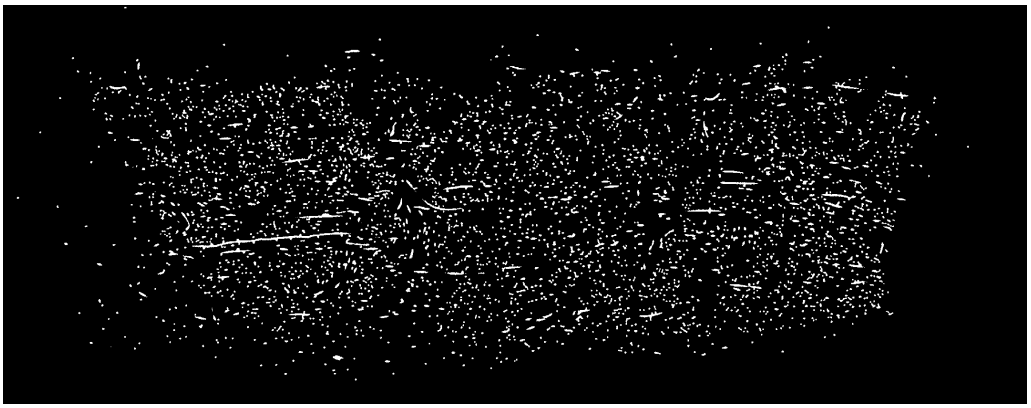

(c) Binarized image with artifact removal in sectional x-y-slice 87.

Figure 5.1.3: The bright spots are artifacts in the high-resolution scan. The sectional images are of size $2\,148 \times 837$ pixels, i.e., $5.26\,\text{mm} \times 2.05\,\text{mm}$.The artifact removal is described in Section 5.1.2.2.

5.1.3 Local Direction Estimation and Distribution Fit

For each fiber voxel, we estimated the fiber orientation with the Hessian matrix of the gray value image [17], [34], see Chapter 3.2. In the next step, the fiber direction in the typical fiber point (in Palm sense, see Stoyan et al. [7]) is modelled by an angular central Gaussian (ACG) distribution, see Chapter 2.1.5. A sample for estimating the parameter matrix A is obtained by the fiber directions of a subsample of foreground (fiber) voxels in the image. Subsampling reduces the amount of data to an acceptable level. Moreover, neighboring voxels are highly dependent as they often belong to the same fiber. By subsampling, we were able to create a nearly independent data set, which is a prerequisite for the parameter estimation. Voxels were sampled by applying independent Bernoulli trials with $p = 1/100\,000$ to all voxels. Prior to the estimation, we rotated the orientations in each sample such that its principal direction was aligned with the x-axis. This way, we ensured comparability between samples.

We calculated the maximum likelihood estimate for the ACG parameter matrix A using the fixed-point algorithm proposed by Tyler [13]. For sample 1, this yielded

$$A = \begin{pmatrix} 1.687 & 0.003 & 0.064 \\ 0.023 & 0.914 & -0.007 \\ 0.064 & -0.007 & 0.399 \end{pmatrix}, \tag{5.1.1}$$

see Fig. 5.1.4 for a visualization. To validate the goodness of fit, we inspected QQ plots for the longitude and colatitude [9]. The model quantiles were obtained by the empirical quantiles of a simulated sample of the fitted ACG model. We validated the goodness-of-fit using QQ plots, see Fig. 5.1.5.

Table 5.1.1 shows the results of the model fit. The results are all sufficiently similar. For all samples, the QQ plots indicate a good fit, see Fig. B.0.1 to Fig. B.0.5.

In the high-resolution scan, the fiber orientation is estimated to be more oriented in the x-direction and less so in the z-direction, see Table 5.1.2. The difference between the estimated A_{11} of both scans is still smaller than the largest difference between samples. Hence, we interpret it as a small improvement due to higher resolution. Again, the QQ plots indicate a good fit, see Fig. 5.1.6

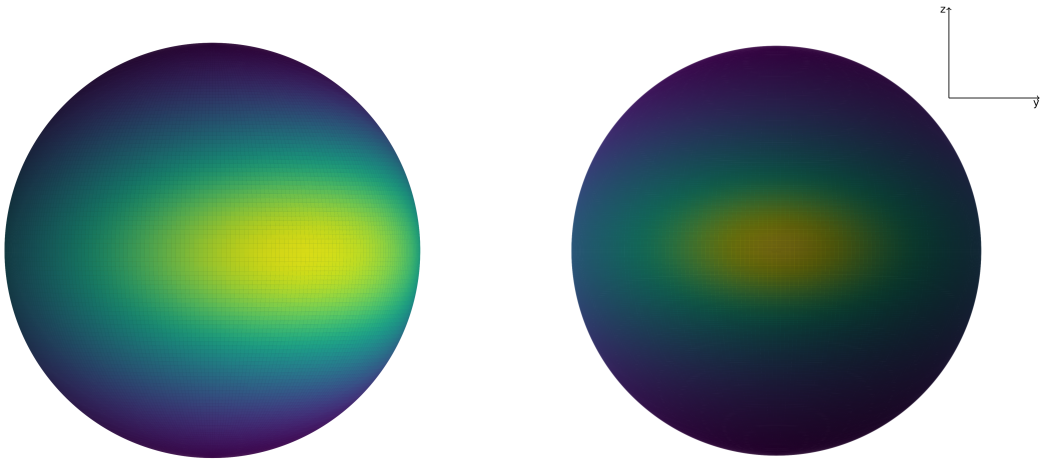

Figure 5.1.4: Spherical density plots of the local fiber orientation distribution for sample 1. The left plot shows the empirical orientation distribution, meaning the distribution that is directly estimated from the observed orientations. The right plot shows the density of the ACG model fitted to the observed orientations. The color scale is the same in both plots. See Fig. 5.1.5 for the validation of the goodness of fit.

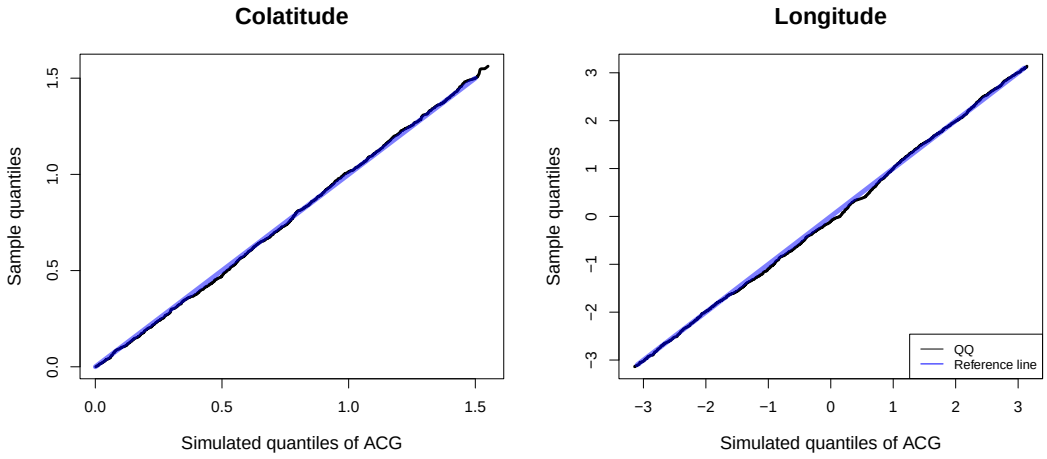

Figure 5.1.5: QQ plots for the ACG parameter estimation of sample 1. Separate plots for colatitude and longitude of the spherical coordinates. Note that the colatitude and longitude are given in radian. The QQ lines are close to the reference line, which indicates a good fit.

Table 5.1.1: ACG parameter estimates for the fiber orientation of the scaffolds.

	A_{11}	A_{12}	A_{13}	A_{22}	A_{23}	A_{33}
Sample 1	1.687	0.003	0.064	0.914	-0.007	0.399
Sample 2	1.483	0.018	0.023	1.077	0.022	0.440
Sample 3	1.341	-0.005	0.158	1.083	0.036	0.576
Sample 4	1.698	0.018	0.016	0.911	-0.001	0.391
Sample 5	1.493	-0.006	-0.010	1.097	-0.011	0.410
Sample 6	1.479	-0.010	0.051	1.067	-0.021	0.454

Table 5.1.2: ACG parameter estimates for the fiber orientation of sample 1.

	A_{11}	A_{12}	A_{13}	A_{22}	A_{23}	A_{33}
Full sample	1.687	0.003	0.064	0.914	-0.007	0.399
High-res section	1.930	-0.018	0.001	0.848	0.019	0.222

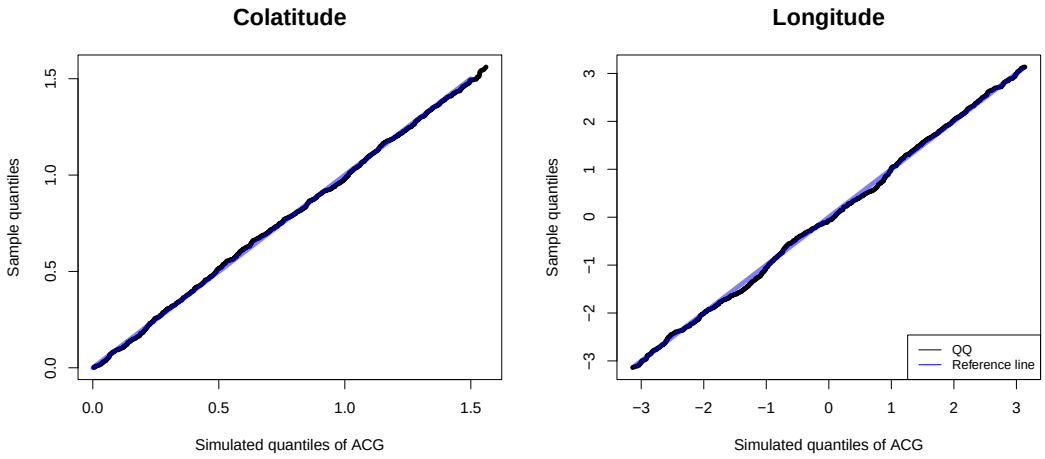

Figure 5.1.6: QQ plots for the ACG parameter estimation of sample 1 scanned in high resolution. Separate plots for colatitude and longitude of the spherical coordinates. Note that the colatitude and longitude are given in radian. The QQ lines are close to the reference line, which indicates a good fit.

5.1.4 Geometric Fiber Model

To give clinicians recommendations on how much a knee joint can be loaded after surgery without breaking the scaffold, colleagues will perform a compression test. As its basis, we generate a geometric fiber model. We choose the Altendorf-Jeulin fiber model as compression depends on the non-overlap condition for fibers. Moreover, we employ endless fibers, see Section 2.2.4 and Section 4.2.3, as the fiber length of 60 mm is by far larger than the window size of 1.85 mm. We use r = 8.5 µm,

$$A = \begin{pmatrix} 1.930 & -0.018 & 0.001 \\ -0.018 & 0.848 & 0.019 \\ 0.001 & 0.019 & 0.222 \end{pmatrix}, \tag{5.1.2}$$

and the expected number of fibers $\gamma = 19741.24$ to yield a volume fraction of 9.5 %, as observed in the high resolution scan. Fig. 5.1.7 shows a visualization of a fiber system realization for these parameters.

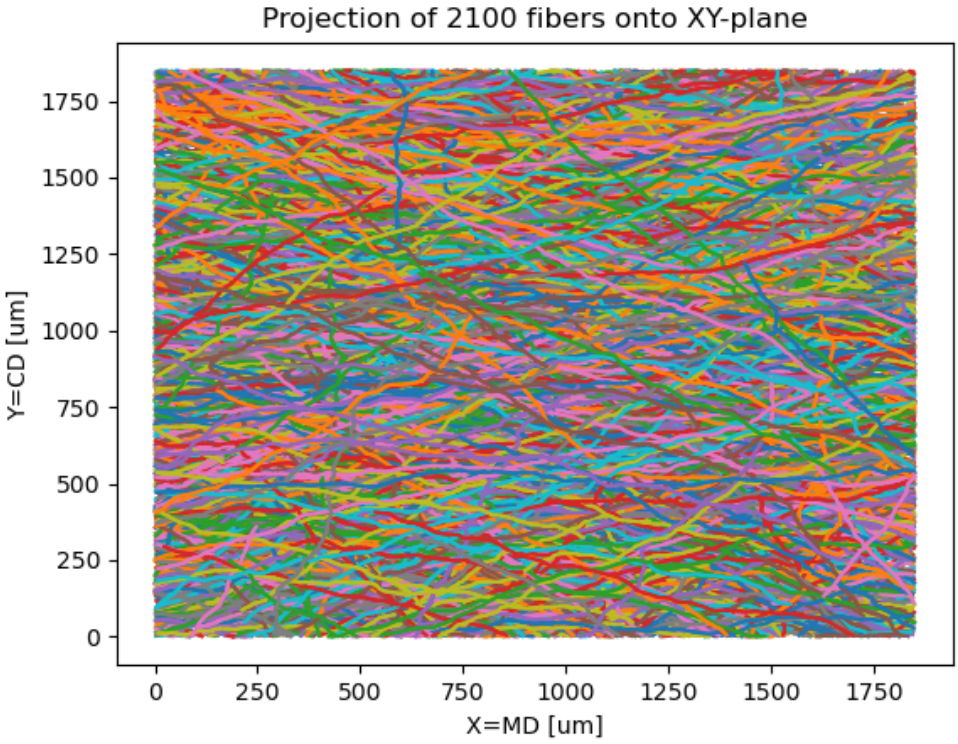

Figure 5.1.7: Visualization of the nonwoven scaffold model using TexMathVisualizer [112].

5.1.5 Discussion and Outlook

In this section, we successfully analyzed the fiber directions in CT images of a nonwoven scaffold material. We used two different CT setups: while the SkyScan allowed for a large field-of-view, the TomoScope allowed for high precision in the segmentation of the fiber system. Both setups caused image artifacts; yet the SkyScan's artifact is more pervasive, hence it has a stronger influence on the estimation of fiber directions and volume fractions.

So far, we calculated local fiber directions using the Hessian matrix. With the high resolution of the TomoScope scans, fiber tracking may also be possible. This could give us access to global direction information and the fiber curvature, which we could use to evaluate the fit of the fiber model.

The fitted direction distributions have already been employed for growth modeling [109]. Mechanical simulations on the geometrical model are under way.

5.2 Wood-fiber Insulation Boards

Studies have found that buildings cause 40 % of energy consumption in the European Union [113]. For climate protection, it is therefore crucial to improve the sustainability of buildings. One approach is to rely on wood as the main construction material since wood is a carbon sink [114]. Yet its thermal conductivity lies with 38 mW/(mK) above the conductivity of traditional material such as mineral wool [4].

Wood-fiber insulation boards consist of single wood fibers (Fig. 5.2.1b) and wood-fiber bundles (Fig. 5.2.1c). Striking features are the square-ish cross-section of the single fiber and the cuboidal shape of the fiber bundle, as well as the tunnel going through these fibers. These tunnels are called the *lumen* of a fiber. Lumen are naturally occurring: This is where the sap of the tree flows. The boards are rather porous (Fig. 5.2.1a), so for the sake of stability, polymer fibers are added that act as glue between different fiber objects. Since the polymer fibers are expected to mainly influence mechanical properties, not thermal conductivity, these fibers are not modeled, neither in previous studies nor in this one.

In a previous study [4], it was found that low thermal conductivity of the wood-based insulation material can be yielded by positioning fibers planarly and aiming for a low volume fraction. We extend the previous study by creating fast simulations with improved representativity for the thermal conductivity simulations. This section aims at modeling fiber systems from available data sets describing the material, simulating fiber geometries efficiently, and simulating thermal conductivity on the geometries. This work has not been published yet.

5.2.1 Estimation of Fiber Length, Single Fiber Thickness, and Fiber Bundle Thickness

In this section, we fit parametric models for the thickness and length of fibers as well as the thickness of fiber bundles. We start off with a data set provided by Fraunhofer WKI, which contains percentiles for the projection area weighted geodesic length and thickness [4] for several commercial products, see Table 5.2.1 and Table 5.2.2. The studied commercial products are named B3, B4, B5, and B6, and they were

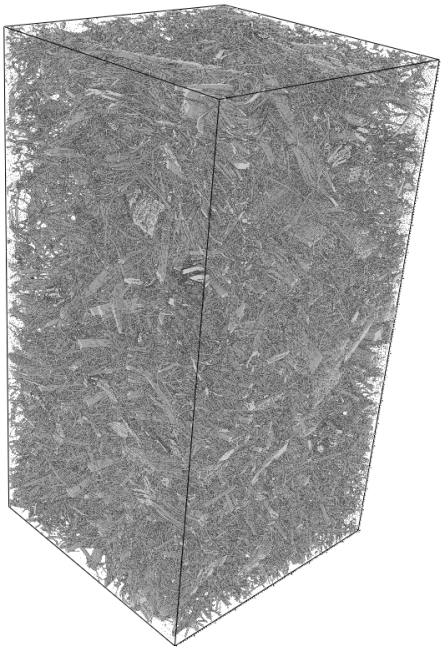

(a) Rendering of a board sample.



(b) Single fiber.

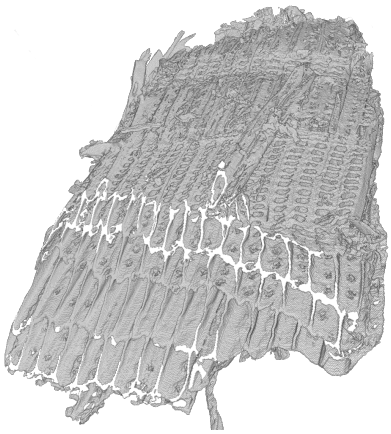

(c) Fiber bundle.

Figure 5.2.1: Rendering of CT images taken from wood-fiber insulation boards.

provided by the company STEICO. Note though that this data should be taken with a grain of salt: The fiber shapes were calculated from the projection area, which can only be a rough estimation of the actual 3D shape. Moreover, only objects with length and thickness above 100 µm were considered. Therefore, we assume that the thickness represents the fiber bundles' thickness. The data is also area-weighted, yet we assume number-weightedness for the sake of simplicity. For more precise estimations, the analysis of CT-scans of the material is under way.

Table 5.2.1: Percentiles of the projection area weighted geodesic length for fiber objects measured by Fraunhofer WKI. B3, B4, B5, and B6 are commercial products.

	p_0	p_5	p_{10}	p_{50}	p_{90}	p_{95}	p_{100}
B3/B4	100 µm	183 µm	342 µm	1 494 µm	3 275 µm	4 158 µm	14 368 µm
B5	100 µm	206 µm	362 µm	1 688 µm	4 233 µm	6 215 µm	19 996 µm
B6	100 µm	256 µm	433 µm	1 666 µm	3 810 µm	4 922 µm	13 445 µm

Table 5.2.2: Percentiles of the projection area weighted geodesic thickness for fiber objects measured by Fraunhofer WKI.

	p_0	p_5	p_{10}	p_{50}	p_{90}	p_{95}	p_{100}
B3/B4	100 µm	102 µm	104 µm	133 µm	367 µm	448 µm	730 µm
B5	100 µm	102 µm	106 µm	160 µm	554 µm	650 µm	1 573 µm
B6	100 µm	103 µm	107 µm	180 µm	397 µm	544 µm	841 µm

The distribution for the length seems rather skewed to the left and takes positive values. Therefore, we model it as a lognormal distribution $\log\mathcal{N}$, which has the density

$$f_{\log\mathcal{N}}(x) = \frac{1}{\sqrt{2\pi\sigma}}\frac{1}{x}\exp\left[-\frac{(\log(x)-\nu)^2}{2\sigma^2}\right], \quad x > 0, \tag{5.2.1}$$

see Shao [115]. We estimate $\hat{\nu}_\ell, \hat{\sigma}_\ell$ for the fiber length and $\hat{\nu}_b, \hat{\sigma}_b$ for the bundle thickness for each dataset by optimizing for parameters ν, σ which minimize the difference between the observed quantiles and the quantiles of the lognormal distribution. The results can be found in Table 5.2.3. There, we also provide the corresponding mean

$\hat{\nu}' = \exp\left(\hat{\nu} + \frac{\hat{\sigma}^2}{2}\right)$ and standard deviation $\hat{\sigma}' = \sqrt{\exp\left(2\hat{\nu} + \hat{\sigma}^2\right)\left(\exp(\hat{\sigma}^2) - 1\right)}$ as these are more intuitively interpretable.

Table 5.2.3: Estimated parameters for the lognormal distributions of the length $(\hat{\nu}_\ell, \hat{\sigma}_\ell)$ and bundle thickness $(\hat{\nu}_b, \hat{\sigma}_b)$. $\hat{\nu}'$ and $\hat{\sigma}'$ are the corresponding mean and standard deviation.

	$\hat{\nu}_\ell$	$\hat{\nu}'_\ell$	$\hat{\sigma}_\ell$	$\hat{\sigma}'_\ell$	$\hat{\nu}_b$	$\hat{\nu}'_b$	$\hat{\sigma}_b$	$\hat{\sigma}'_b$
B3/B4	7.15	1 662.50	0.73	1 383.94	5.17	206.37	0.56	125.43
B5	7.27	2 112.83	0.88	2 293.66	5.36	271.27	0.69	212.45
B6	7.29	1 934.68	0.74	1 646.18	5.30	236.71	0.59	151.31

Further, we rescanned a sample of the wood fiber insulation board product B5, which was already used in previous work [4], at ID19 of the European Synchrotron Radiation Facility (ESRF). Colleagues segmented and labeled single fibers within the image. For each single fiber, the thickness was estimated [116]. Following Andrä et al. [4], we assume a normal distribution for the fiber thickness. To fit a normal distribution to the thickness data, we use the function fitdistr in the R-package MASS [117], yielding a mean $\hat{\nu}_t = 33.89\,\mu m$ and a standard deviation $\hat{\sigma}_t = 8.36\,\mu m$.

5.2.2 Geometric Fiber Models

To model the fiber system in an insulation board geometrically, we employ a Boolean model with cuboids as grains, as this allows for fast simulation. The cuboids represent single fibers and fiber bundles and have length ℓ and thickness t_1, t_2 for the remaining two edges. For a single fiber, the cuboid length $\ell \sim \log\mathcal{N}(\nu_\ell, \sigma_\ell)$. The thickness $t_1 = t_2 \sim \mathcal{N}(\nu_t, \sigma_t)$. For a fiber bundle, the cuboid length $\ell \sim \log\mathcal{N}(\nu_\ell, \sigma_\ell)$, as well. The thickness parameters t_1 and t_2 are sampled separately though, namely as $t_1, t_2 \sim \log\mathcal{N}(\nu_b, \sigma_b)$. For their orientation in space, the direction of the longitudinal axis follows a Schladitz distribution with parameter β, see Section 2.1.5. The rotation around the longitudinal axis follows a uniform distribution $\mathrm{Unif}(0, 180°)$.

Thermal conductivity is largely influenced by the volume fraction. A volume fraction of 4 % was already observed as well-performing by Andrä et al. [4]. Since we

neglect the lumen of the fibers in this model, i.e., the naturally occuring tunnels in wood fibers, we use 8 % as the volume fraction V_V of the fiber system. This conforms to the observation from CT images that fibers have a wall-thickness of roughly 0.125 times the fiber thickness. We denote the volume fraction considering only single fibers as V_{VS} and the one for fiber bundles as V_{VB}, where $V_V = V_{VS} + V_{VB}$. To calculate the corresponding intensities λ_S and λ_B of the germs for single fibers and for fiber bundles, resp., we use Miles' formula, see Section 2.2.3.

We discretize the results in images of size 512^3 with a voxel size of 12.5 µm. For each parameter combination, we generate 10 realizations. As edge treatment, we use plus-sampling: The fiber lengths' 90%-percentile in product B5 is at 4 233 µm, i.e., 339 voxels. Therefore, we plus-sample with half the fiber length (170 voxels) in each direction.

Based on the estimated parameters for B5, we consider the default case of our simulation as $\nu_\ell = 7.27$, $\sigma_\ell = 0.88$, $\nu_b = 5.36$, $\sigma_b = 0.69$, $\nu_t = 33.89$, $\sigma_t = 8.36$, $\beta = 2$, $V_{VS} = 5.6\,\%$, and $V_{VB} = 2.4\,\%$. We systematically study the behavior under variation of these parameters by varying each parameter separately. For the lognormal distribution, we vary the mean and standard deviation for better interpretability. In particular, we aim for relatively small variation from the observed parameters. Tables C.0.3 - C.0.1 give an overview of the parameter choices for the grain shapes. Further, we vary $\beta = 1, 2, 3$, and $V_{VB} = 0.8\,\%, 1.6\,\%, 2.4\,\%, 3.2\,\%, 4\,\%$. Fig. 5.2.2 shows a rendering of a realization for the default case.

5.2.3 Thermal Simulation

Colleagues at Fraunhofer ITWM simulate thermal conductivity on the geometric model realizations described above with the exact same setup as in Andrä et al. [4] using GeoDict [108]. For this, they use the LIR solver [118] with periodic boundary conditions in x- and y-direction, while the temperature difference is applied in z-direction. They combine periodic boundaries in the solver with plus-sampling for the fiber geometries, as this is known to have a negligible effect for conductivity simulations [119]. For the parameter settings, see Andrä et al. [4]. The thermal conductivity $k_{\text{therm}}(T)$ of the structures is obtained through homogenization.

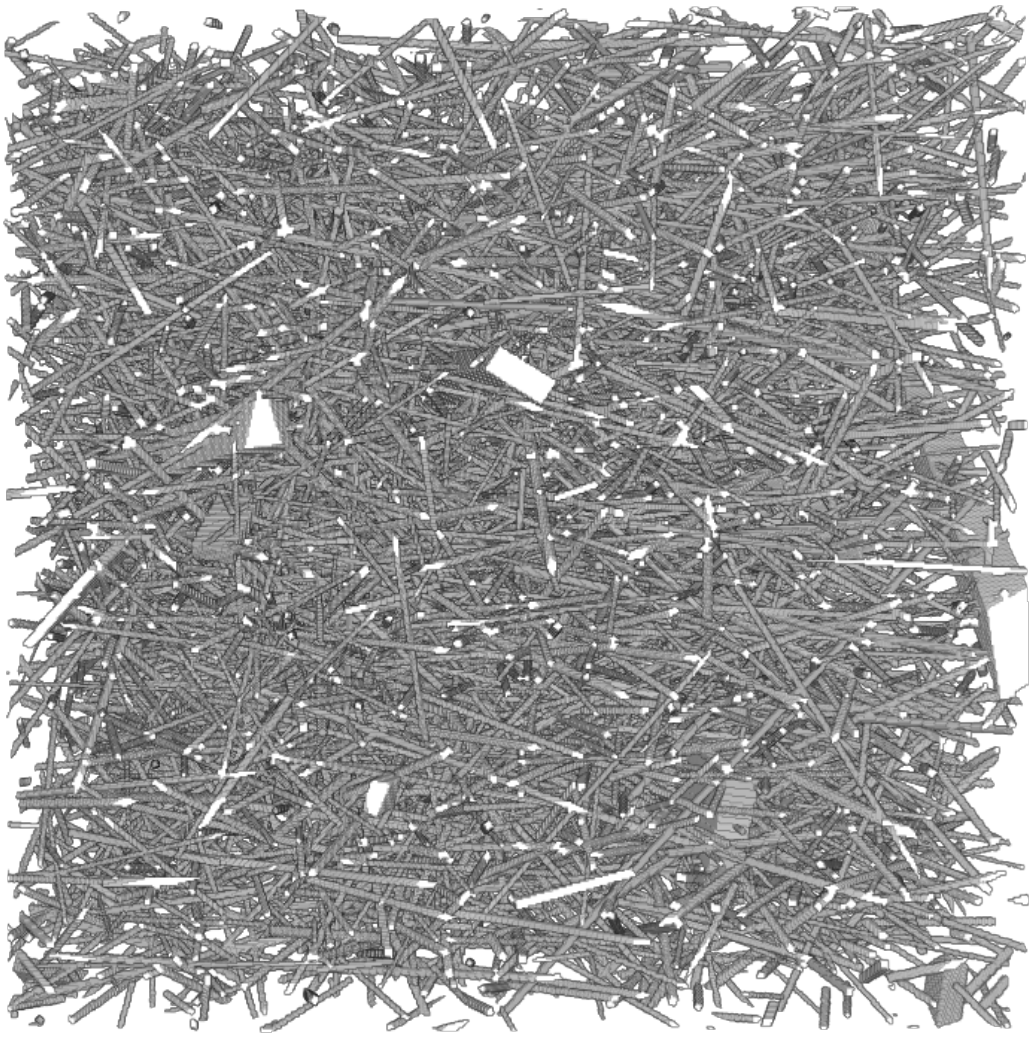

Figure 5.2.2: Rendering of a Boolean model realization with default parameters ($\nu_\ell = 7.27$, $\sigma_\ell = 0.88$, $\nu_b = 5.36$, $\sigma_b = 0.69$, $\nu_t = 33.89$, $\sigma_t = 8.36$, $\beta = 2$, $V_{VS} = 5.6\,\%$, and $V_{VB} = 2.4\,\%$).

In addition, they calculate the radiative conductivity in the pore space based on the Stefan-Boltzmann law for thermal radiation [120]. More precisely, they calculate the pores' mean chord length $\bar{\ell}_c$ in z-direction, which yields the radiative conductivity $k_{\text{rad}}(T) = 4c_{\text{SB}}T^3\bar{\ell}_c$, where T is the temperature and c_{SB} is the Stefan-Boltzmann constant. The effective radiation is then

$$k_{\text{rad, eff}}(T) = \left(\frac{V_V}{k_{\text{solid}}} + \frac{1 - V_V}{k_{\text{rad}}(T)}\right)^{-1}, \tag{5.2.2}$$

where k_{solid} is the conductivity of wood. We report the total conductivity $k_{\text{total}}(T) = k_{\text{therm}}(T) + k_{\text{rad, eff}}(T)$.

The results in Fig. 5.2.3 show a trend of improved insulation for large values of β, i.e., planar orientation distribution of the fiber, a small fiber thickness, and a low volume fraction of the fiber bundles. This replicates the results observed by Andrä et al. [4].

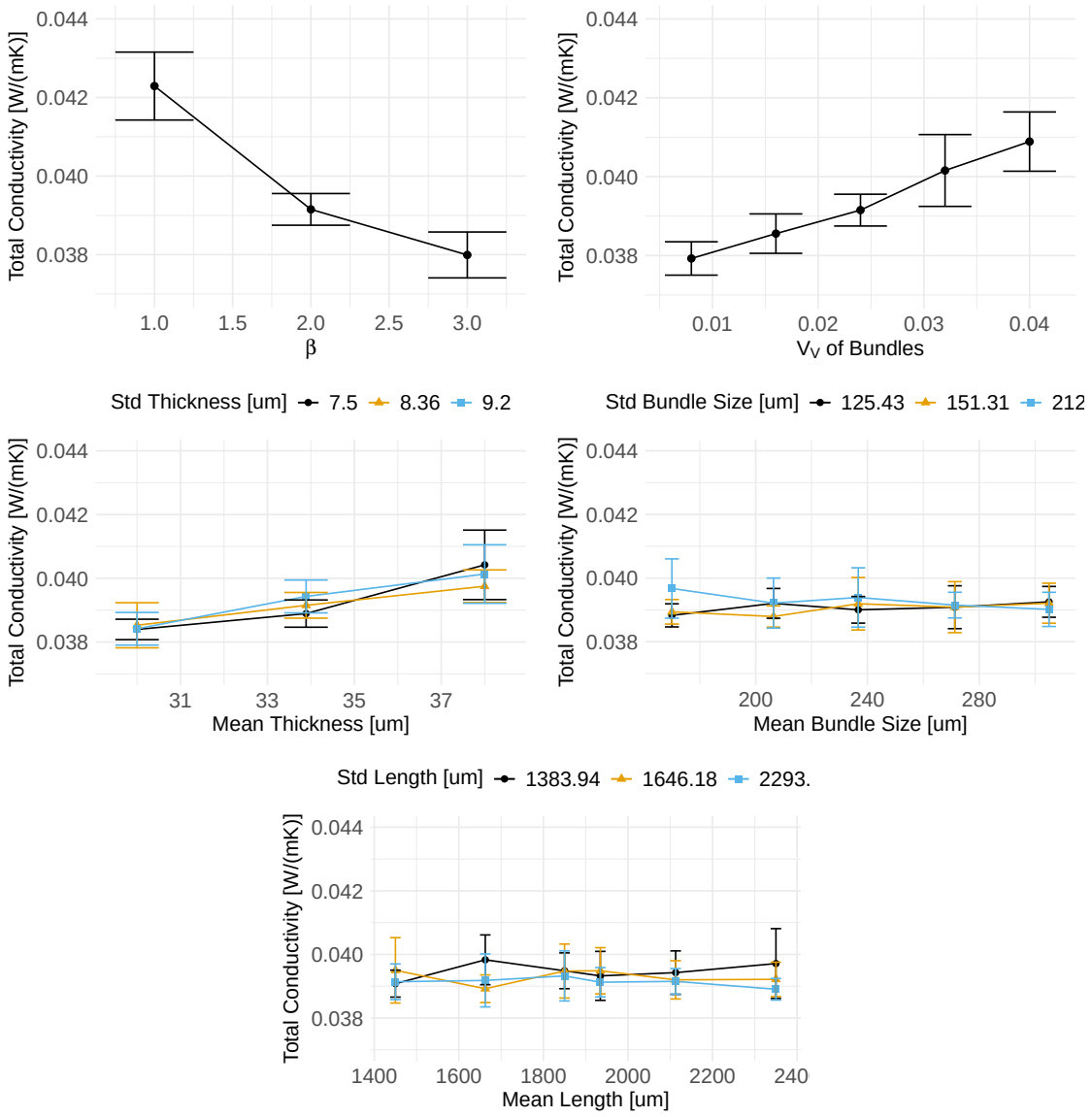

Figure 5.2.3: Simulated thermal conductivities for the Boolean model realizations. The plots are grouped according to the varied parameter sets. The plot points indicate the mean value, bars indicate the standard deviation.

Since we have not estimated the RVE size-number as in Chapter 4.5.2, we justify our choice of image size and number in hindsight by calculating the estimated

precision of the observed conductivities per parameter combination. Since we do not estimate K and α, we replace the term $KV^{-\alpha}$ by the observed standard deviation as

$$\hat{\varphi} = \frac{2\text{std}_C}{\sqrt{n}\text{mean}_C}, \tag{5.2.3}$$

where mean_C is the mean value and std_C is the standard deviation of the simulated thermal conductivity. For each parameter combination, $\hat{\varphi}$ lies below 2 %, which justifies our choice of size and number as representative under a precision of 2 %.

5.2.4 Discussion

In this section, we studied the conductivity of wood-fiber insulation mats under different parameters for their fiber orientation, thickness, length, their bundle thickness and fraction. As comparison to the material as is, we fitted distributions of the fiber thickness, the fiber length, and the bundle thickness to real-world data. We varied the parameters close to the estimated values and confirmed the results in Andrä et al. [4]. This is only a visual analysis; a formal optimization of the parameters will be performed by colleagues and published in a paper that is currently in preparation.

The Boolean model is advantageous for such simulation studies as it allows for fast generation of realizations. At the same time, the Boolean model is only a simplification of a fiber board. It allows for intersections between fiber objects, which is unrealistic. This model also does not contain the lumen, i.e., the naturally occurring tunnels in wood fibers. In the following section, we will investigate the impact of such model decisions on the simulations of total conductivity. Moreover, it may be of interest to study the correspondence of other relevant microstructure characteristics to CT images of the material, e.g., constrictivity or tortuosity [5].

5.3 Impact of Model Decisions

In Section 5.2, we employed a Boolean model as it is fast to generate. In Chapter 4, on the other hand, we claimed that the Altendorf-Jeulin model yields more realistic results as it avoids inter-fiber intersections, and that its extension to the contact model offers the possibility to accurately model inter-fiber contacts, which strongly impact physical properties such as thermal conductivity and stiffness. In this section, we investigate the influence of such model decisions on simulation results. This work is not published yet.

5.3.1 Model Selection

We select the following models for comparison[1]:

- The Boolean model with cylinders as fibers, cuboids as fibers, and cuboids as fibers and fiber bundles,



- the Altendorf-Jeulin model with circular cross-section, with square cross-section, and with square cross-section but hollowed as to simulate the lumen,

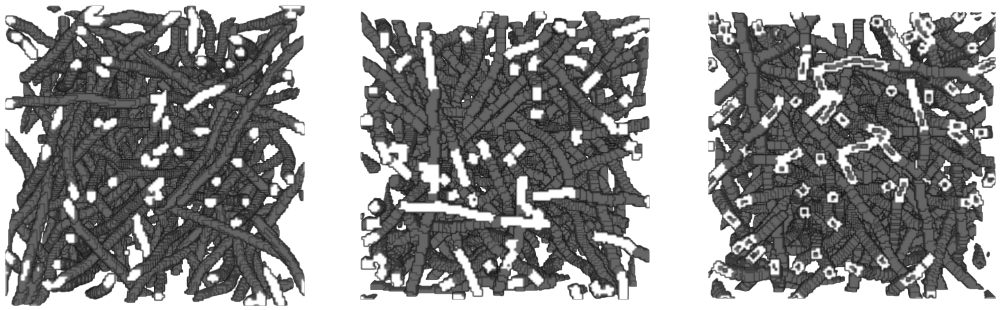

[1]Except for the contact models, we show renderings of an extracted part of a realization for each model. We do not show the full rendering for the sake of visibility of the cross-sections.

- the contact model with circular cross-section, with square cross-section, and with square cross-section but hollowed as to simulate the lumen,
- and the bundle model with square cross-section, with square cross-section but hollowed as to simulate the lumen, and with square cross-section but hollowed as to simulate the lumen as well as contact forces.

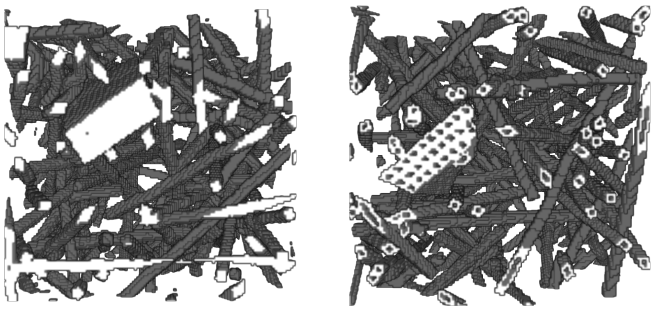

The fibers are assigned a constant length of 200 voxels. For the cylinder/circular cases, the radius is 2 voxels, and for the cuboid/square cases, the edge length is 4 voxels. This results in different areas for the cross-sections; however, the space between chain links in the Altendorf-Jeulin model stays constant. The fiber bundles are assigned a length of 200 voxels, a width of 40 voxels, and a height of 12 voxels. For the Altendorf-Jeulin bundle model, see Chapter 4.3, this allows us to set the number of fibers in a bundle to the constant numbers $n_1 = 3$ fibers, $n_2 = 10$ fibers, and the bundle radius to a constant $r_B = 23.41$ voxels, which ensures some spacing between different bundles. The total volume fraction is 10 % as to stay consistent with the setup in Chapter 4.5. When fiber bundles are part of a model, they account for 2 % of the volume fraction; the remaining 8 % of the volume fraction consist of single fibers, thus yielding a volume fraction of 10 % too. To keep the volume fraction constant, we adapt the number of objects/intensities accordingly. In the case of hollow fibers, we consider the volume fraction of non-hollow fibers. The fiber-wall thickness is 0.25 times the fiber thickness, i.e., 1 voxel. If we chose half the wall thickness as assumed in the previous chapter, this would require us to also choose a different fiber thickness. However, we chose this as a trade-off with the runtime required for RVEs, which is discussed in the following section. As edge-treatment, we use periodic boundary conditions as this is known to reduce image-size dependent

biases [119].

For each of the generated geometries, colleagues at ITWM simulate the thermal and radiative conductivity as in Chapter 5.2. For the sake of comparability, we use a voxel size of 6.25 µm for the radiation, even though the experiments were otherwise set up as dimensionless. In addition, they simulate the stiffness using ConductoDict [108] with an elasticity module of 12 GPa and a Poisson number of 0.3.

5.3.2 RVE Study

In this section, we study the necessary number and size of images to gain representative results for the simulated thermal and radiative conductivity as well as the simulated stiffness. As a baseline model, we use the Boolean model with cylinders as grains and generate 25 realizations each for the image sizes $s = 256, 384, ..., 1\,408$. Fig. 5.3.4, Fig. 5.3.5, and Fig. 5.3.6 show the results for each physical property. The increase in the thermal conductivity and the stiffness with increasing image size are due to an image-size dependent bias. This is known to be a problem for mechanical simulations but negligible for thermal conductivity simulation [119]. For size $1\,024$, i.e., 5 times the fiber length, the bias disappears. For radiative conductivity, this bias seems to disappear for images with a volume larger than 512^3; the variance seems to change its behavior around the volume $1\,024^3$, just like the other physical properties.

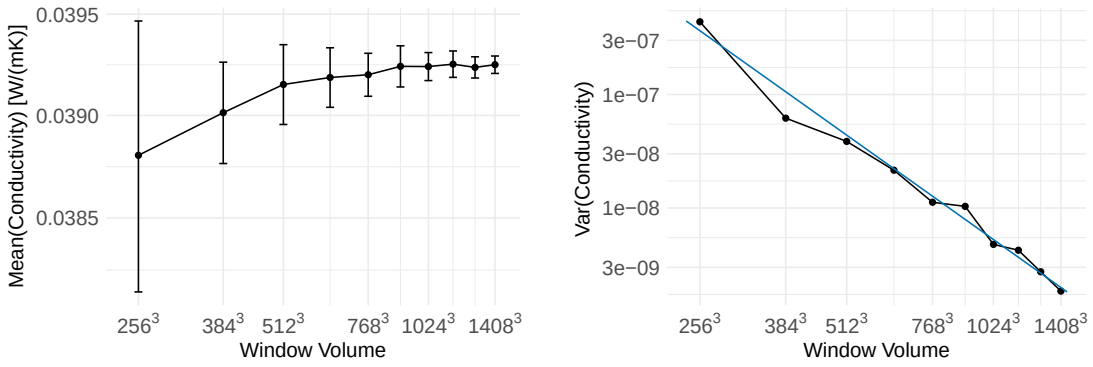

Figure 5.3.4: Plots of the mean and variance of the thermal conductivity w.r.t. the window volume. The line in blue indicates the fitted model for image volumes larger or equal to $1\,024^3$ with $K = 8.37$ and $\alpha = 1.02$.

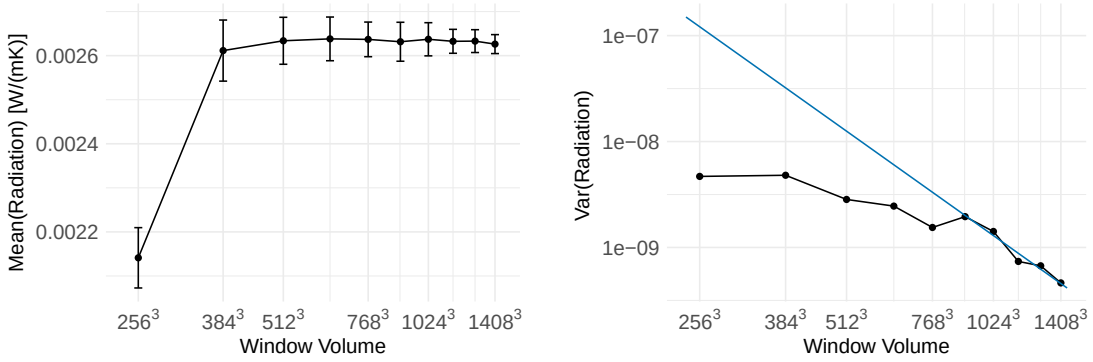

Figure 5.3.5: Plots of the mean and variance of the radiative conductivity w.r.t. to the window volume. The line in blue indicates the fitted model for image volumes larger or equal to $1\,024^3$ with $K = 9.32$ and $\alpha = 1.09$.

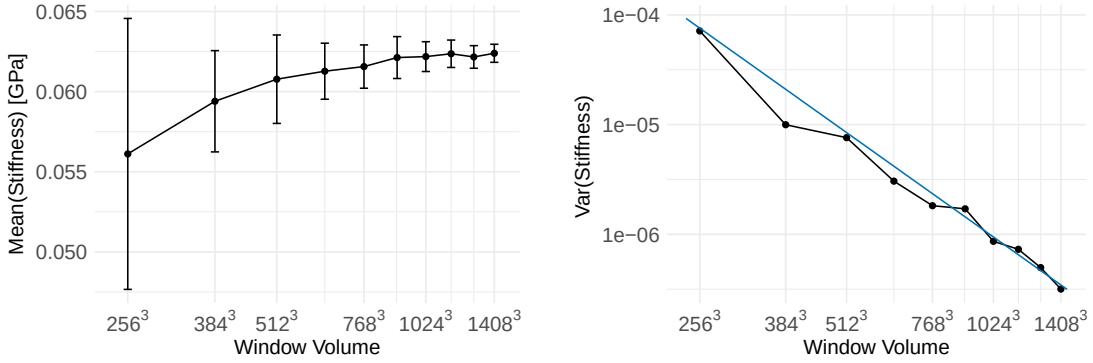

Figure 5.3.6: Plots of the mean and variance of the stiffness w.r.t. to the window volume. The line in blue indicates the fitted model for image volumes larger or equal to $1\,024^3$ with $K = 3\,102.07$ and $\alpha = 1.05$.

For image volumes above $1\,024^3$, the variance of the conductivity and the stiffness are already considerably low, while the runtime for the discretization of the Boolean model already exceeds 2 h. For variants of the Altendorf-Jeulin model, which is algorithmically far heavier than the Boolean model, we can expect considerably higher runtimes when generating geometric realizations for the actual study. In particular for an image size of 1 408, discretization takes up to 16 h, and simulating the stiffness requires 8 h. Therefore, we choose an image size of 1 024. Employing formula (4.5.3) with an accuracy of 1 % and an image size of 1 024, we yield one image for thermal conductivity, eight images for radiative conductivity, and 10 images for the stiffness. See Fig. 5.3.4, Fig. 5.3.5, and Fig. 5.3.6 for the fitted values α, K and

the corresponding variance plots.

5.3.3 Results

Fig. 5.3.7 shows the thermal conductivity for the different models. The effect of hollow fibers is the strongest as it reduces the volume fraction, one of the strongest predictors of thermal conductivity. Further, there is a considerable difference within the fiber-packing methods regarding the fiber cross-section; the increase of contact is comparably small. Interestingly, the conductivity for the Boolean model lies between the results for hardcore-packing and shows little dependence on the cross-section. This indicates robustness of the Boolean model for thermal conductivity.

The radiation paints a rather different picture, see Fig. 5.3.8: Here, every method behaves rather differently depending on the cross-section; especially the bundle models increase the radiation, which is likely due to the fibers clustering in the bundles, resulting in larger pores between all objects. Hollow fibers have a rather small effect in lowering the radiation, and the increase of contact is negligible. This pattern is not surprising considering the driving force of radiation is the pore size distribution, not the volume fraction or contact as for thermal conductivity.

The plot for the total conductivity, see Fig. 5.3.9, combines both effects of thermal and radiative conductivity, which sets the effect of both types of conductivity in relation. While the effect of thermal conductivity has the major influence on model decisions related to the Altendorf-Jeulin model, the Boolean model appears less robust than solely for the thermal conductivity. The radiative effect indicates the relevance of modeling bundles explicitly.

Fig. 5.3.10 shows the stiffness for different models. Here, we observe the strongest variation between models so far, e.g., Boolean cylinders yield 6 times the stiffness for hollow square fibers that were packed with the Altendorf-Jeulin model. For stiffness, the effect of cross-sections is strongest for the Boolean model. The stiffness clearly increases together with contact - compare the Altendorf-Jeulin and the contact models. For the Altendorf-Jeulin model, the stiffness is higher for the square-ish cross-section than for the circular one; for the contact model, on the other hand, this effect is not visible. This may be attributed to the implementation of the square

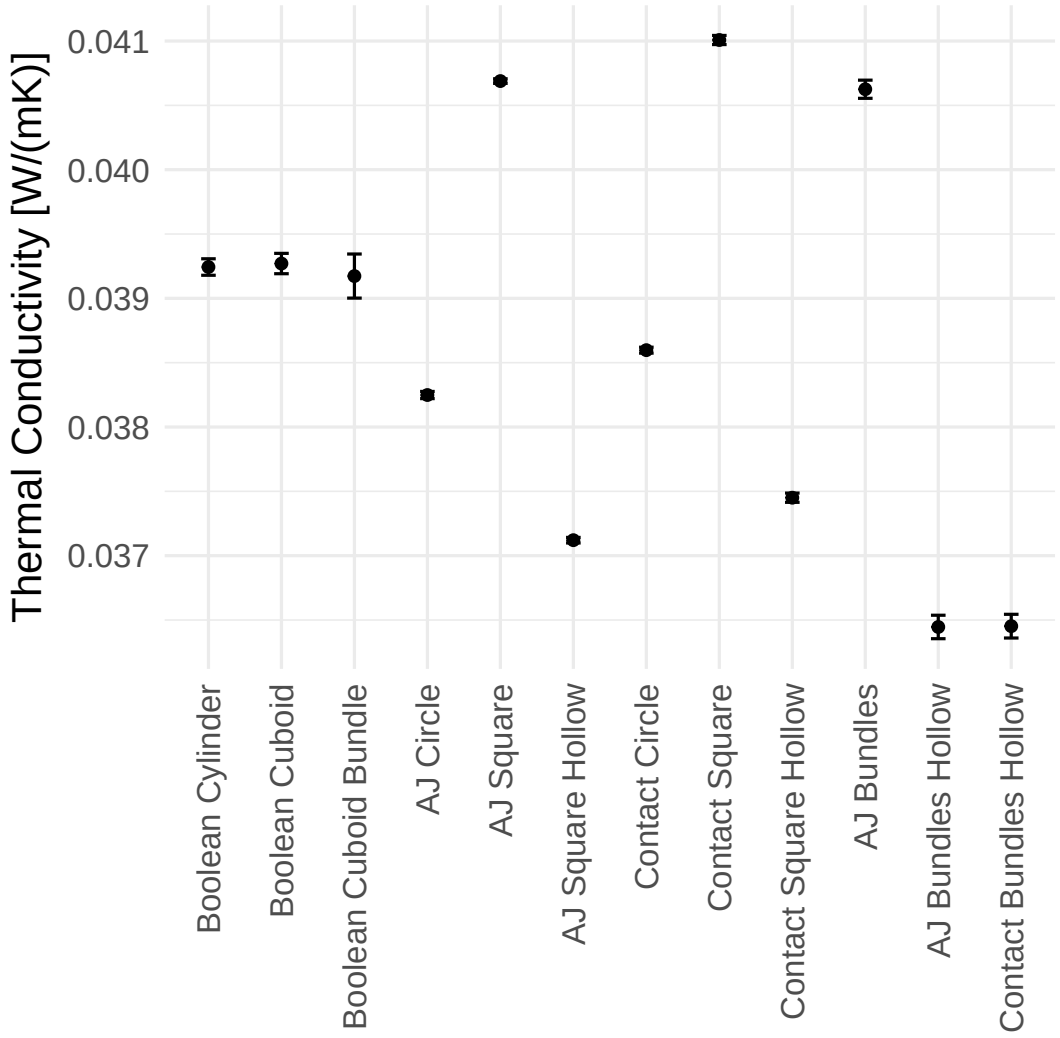

Figure 5.3.7: Plots of the mean thermal conductivity for each model. Bars indicate the standard deviation; however, they may not be visible because they are so low.

cross-section, namely, that the avoidance of intersection and the increase of contact are merely based on balls that are inscribed in the square-ish cross-section. Hence, the square-ish cross-section for the Altendorf-Jeulin may already have a higher amount of contact due to intersection of edges, whereas the contact within the contact model is barely changed anymore. Hollow fibers yield lower stiffness, which is not surprising.

5.3.4 Discussion

In this section, we studied the impact of model decisions on physical simulations. The results for stiffness were highly dependent on model decisions. In particular,

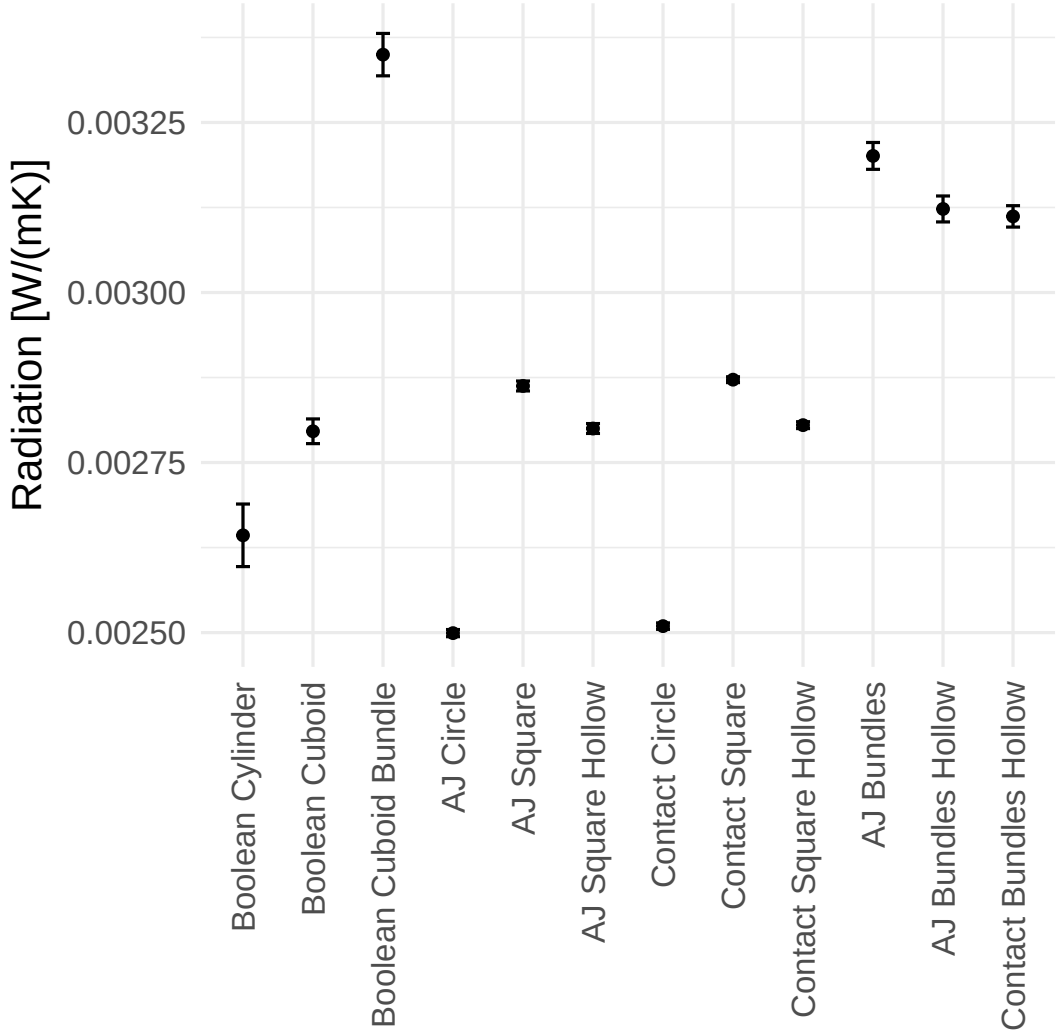

Figure 5.3.8: Plots of the mean radiative conductivity for each model. Bars indicate the standard deviation; however, they may not be visible because they are so low.

decisions impacting the amount of contact had a strong influence on the stiffness, which highlights the relevance of the contact model in Section 4.4. Yet, not only the explicit increase of contact had an influence, also decisions on the cross-section of fibers influenced the inter-fiber contact/intersections and thus the stiffness.

Thermal conductivity shows rather low sensitivity of up to 10 %. Considering Section 5.2, the Boolean model shows high robustness together with low runtimes, which justifies the model decision in the previous section. We have shown that the modeling of bundles is highly relevant for the radiation. Even though the bundle size did not show a strong influence on the total conductivity in Chapter 5.2, our

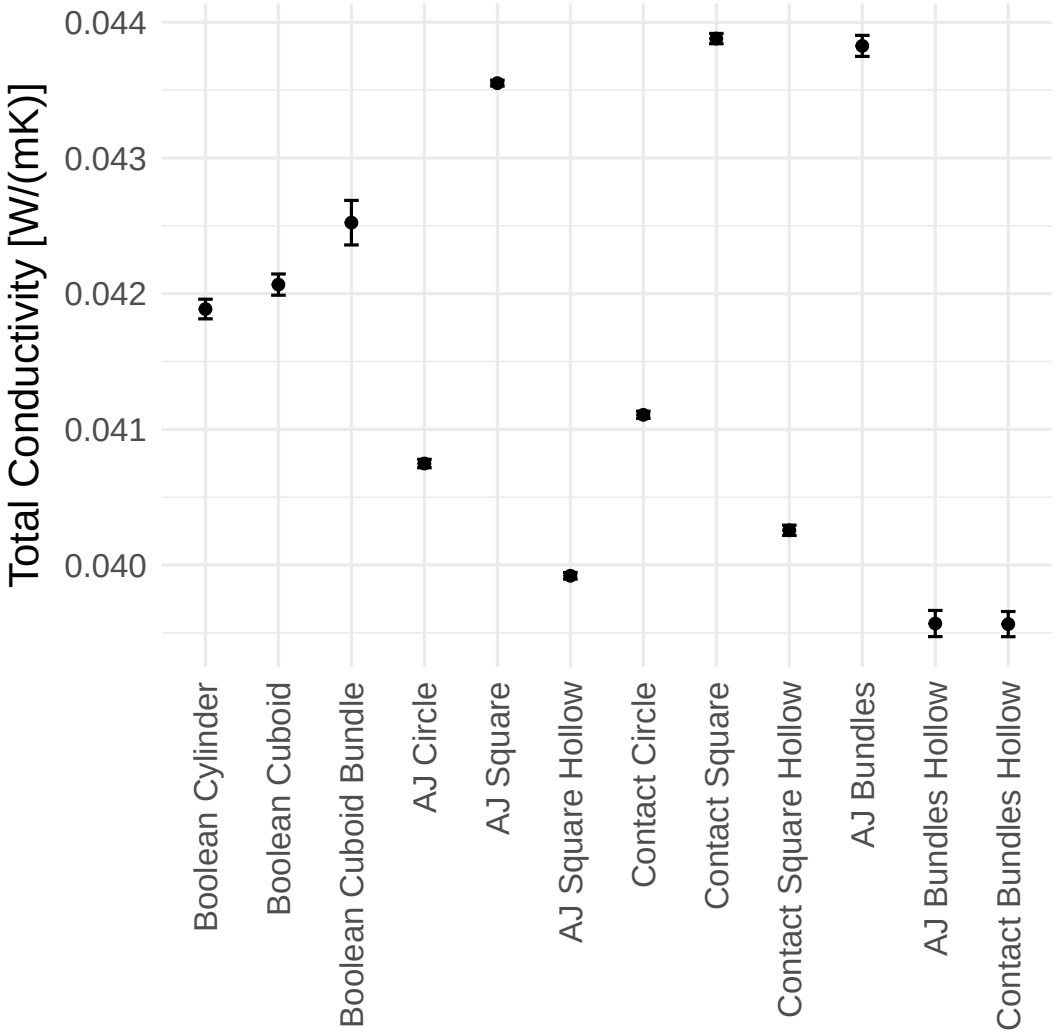

Figure 5.3.9: Plots of the mean total conductivity for each model. Bars indicate the standard deviation; however, they may not be visible because they are so low.

results in this section demonstrate the importance of modeling bundles explicitly. Especially for thermal conductivity but also for stiffness, hollow fibers performed strongly different than their full counterparts. Still, we were able to compare model performances within the groups of full and hollow fibers. If one is interested in the exact values for thermal conductivity, correction for hollow fibers may be reasonable. Nonetheless, this study shows that Boolean models are well-suited to study the impact of parameter variations.

In this study, we employed commonly used methods for thermal and mechanical simulations as implemented in GeoDict. These results are not necessarily generalizable

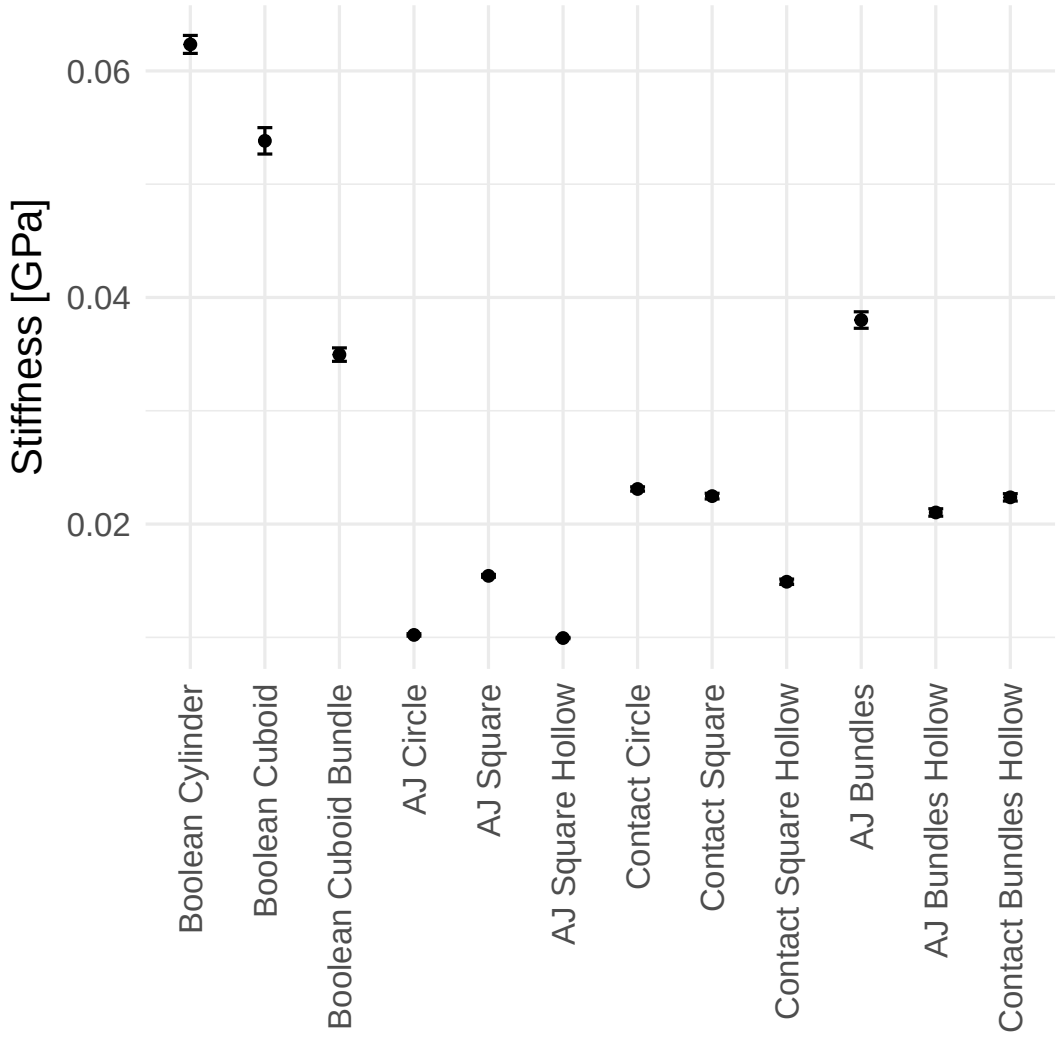

Figure 5.3.10: Plots of the mean stiffness for each model. Bars indicate the standard deviation; however, they may not be visible because they are so low..

to other methods. In particular, these methods are voxel-based, which makes them scale-dependent. Further, this study has been limited by the necessary image size and, thus, runtime to reach the necessary representativity.

To gain further insights into how much is gained by using the hollow bundle model as proposed in Chapter 4.3 over a Boolean model in Section 5.2, further simulations could be performed on smaller image sizes at the cost of a small bias in the estimated conductivity. For example, it would be interesting to further study how much the variation of results between different models is impacted by planar fibers, as well as the effect of scaling. In the present study, we further made the

model decision to adapt the cross-section area such that the chain link size in the Altendorf-Jeulin model stays constant. In a smaller setup, we could investigate the impact of this decision by choosing a constant cross-section area instead.

Future work could further study the difference between the original Altendorf-Jeulin model and the contact model in mechanical simulations by employing graph-based fiber models as input [121]. This way, the results are independent of voxelization. Moreover, the study can be applied to a different use-case, namely textile materials such as nonwovens, see Section 5.1.

Chapter 6

Conclusion

The main achievement of this thesis is the development of a fiber model in which inter-fiber contact is explicitly modeled and can be increased parametrically. We ensure the accuracy of the model and show that it is capable of generating inter-fiber contact that exceeds analytical results. We further provide evidence of the relevance of this model by applying mechanical simulations on wood-fiber models where the inter-fiber contact is either increased or not. Research opportunities include the modification of the fiber model to other types of fiber generation, such as endless fibers, different random walks, or different cross-sections. Future work will apply this model to nonwovens and study the impact on mechanical simulations.

Further, we extend the Altendorf-Jeulin fiber model such that it allows for modeling wood fiber bundles. This provides a possibility to compare different fiber models for modeling wood-fiber materials in the context of mechanical simulations and study the impact of such model decisions. In addition to justifying our own model decisions for an application case, it may serve as a decision aid for future modeling endeavors.

With the development of an image similarity measure for directional data, we tackle a problem of registering multimodal image data: To validate a novel imaging method, such as a polarization camera for carbon sheet molding compounds (C-SMC), either a ground truth or a reliable alternative method should be given. However, the established procedure to take CT scans struggles with artifacts and the difficulty of low contrast and low resolution, thus making established methods struggle to estimate

fiber directions. We are able to overcome this problem using anisotropic Gaussian filters; nonetheless, a fair comparison between the CT-based orientation images and polarization images is still to be found. Established methods for orientational data are optimized for other use-cases such as tensor data. Therefore, the image similarity measure we propose is a first step to validate polarization imaging and study its unique artifacts.

By providing a real-world application to nonwovens, we give examples on the pipeline from image analysis to models of fiber-based microstructures. For the wood-fiber insulation boards, we even go a step further and showcase data-driven modeling of fiber systems as a basis for the simulation of physical properties. In ongoing work, we use the simulation results for microstructure optimization. Moreover, we were able to showcase the relevance of the methodological research.

Bibliography

[1] C. Gaunand, Y. De Wilde, A. François, V. Grigorova-Moutiers, and K. Joulain, "Modeling conductive thermal transport in three-dimensional fibrous media with fiber-to-fiber contacts," *Physical Review Applied*, vol. 23, 2025. DOI: 10.1103/PhysRevApplied.23.034084.

[2] V. A. Yastrebov, *Numerical Methods in Contact Mechanics*. John Wiley & Sons, 2013.

[3] L. Orgéas and P. J. Dumont, "Sheet molding compounds," in *Wiley Encyclopedia of Composites*, John Wiley & Sons Inc, 2012, pp. 1–36.

[4] H. Andrä, D. Dobrovolskij, M. Engelhardt, *et al.*, "Image-based microstructural simulation of thermal conductivity for highly porous wood fiber insulation boards: 3D imaging, microstructure modeling, and numerical simulations for insight into structure–property relation," *Wood Science and Technology*, vol. 57, 2023. DOI: 10.1007/s00226-022-01434-6.

[5] B. Prifling, M. Röding, P. Townsend, M. Neumann, and V. Schmidt, "Large-Scale Statistical Learning for Mass Transport Prediction in Porous Materials Using 90,000 Artificially Generated Microstructures," *Frontiers in Materials*, vol. 8, 2021. DOI: 10.3389/fmats.2021.786502.

[6] OpenAI, *GPT o4-mini*.

[7] S. N. Chiu, D. Stoyan, W. S. Kendall, and J. Mecke, Eds., *Stochastic Geometry and Its Applications* (Wiley Series in Probability and Statistics), 3rd ed. Wiley, 2013, ISBN: 978-0-470-66481-0.

[8] K. V. Mardia and P. E. Jupp, *Directional Statistics* (Wiley Series in Probability and Statistics). Wiley, 2000, ISBN: 978-0-471-95333-3.

[9] N. I. Fisher, T. Lewis, and B. J. J. Embleton, *Statistical Analysis of Spherical Data*. Cambridge University Press, 1987, ISBN: 978-0-521-24273-8.

[10] A. Pewsey and E. García-Portugués, "Recent advances in directional statistics," 2021. DOI: 10.1007/s11749-021-00759-x.

[11] K. V. Mardia, "Fisher's legacy of directional statistics, and beyond to statistics on manifolds," *Journal of Multivariate Analysis*, vol. 207, 2025. DOI: 10.1016/j.jmva.2024.105404.

[12] H. Altendorf, "3D Morphological Analysis and Modeling of Random Fiber Networks," TU Kaiserslautern, Kaiserslautern, Germany, 2011.

[13] D. E. Tyler, "Statistical Analysis for the Angular Central Gaussian Distribution on the Sphere," 1987.

[14] K. Schladitz, S. Peters, D. Reinel-Bitzer, A. Wiegmann, and J. Ohser, "Design of acoustic trim based on geometric modeling and flow simulation for non-woven," *Computational Materials Science*, vol. 38, 2006. DOI: 10.1016/j.commatsci.2006.01.018.

[15] J. Franke, C. Redenbach, and N. Zhang, "On a Mixture Model for Directional Data on the Sphere: A mixture model for directional data," *Scandinavian Journal of Statistics*, vol. 43, 2016. DOI: 10.1111/sjos.12169.

[16] R. Schneider and W. Weil, *Stochastic and Integral Geometry* (Probability and Its Applications), J. Gani, C. Heyde, P. Jagers, and T. G. Kurtz, red. Springer, 2008, ISBN: 978-3-540-78858-4 978-3-540-78859-1. DOI: 10.1007/978-3-540-78859-1.

[17] J. Ohser and K. Schladitz, *3D Images of Materials Structures: Processing and Analysis*, 1st ed. Wiley, 2009, ISBN: 978-3-527-31203-0 978-3-527-62830-8. DOI: 10.1002/9783527628308.

[18] C. Peyrega, D. Jeulin, C. Delisée, and J. Malvestio, "3D Morphological Modelling of a Random Fibrous Network," *Image Analysis & Stereology*, vol. 28, 2011. DOI: 10.5566/ias.v28.p129-141.

[19] S. Toll, "Note: On the tube model for fiber suspensions," *Journal of Rheology*, vol. 37, 1993. DOI: 10.1122/1.550460.

[20] S. Toll, "Packing mechanics of fiber reinforcements," *Polymer Engineering & Science*, vol. 38, 1998. DOI: 10.1002/pen.10304.

[21] R. V. Ambartzumian, *Factorization Calculus and Geometric Probability*. Cambridge University Press, 1990.

[22] H. P. Keeler, *Simulating a Poisson line process*, 2020. [Online]. Available: hpaulkeeler.com/simulating-a-poisson-line-process/.

[23] G. A. Atkinson and J. Ernst, "High-sensitivity analysis of polarization by surface reflection," *Machine Vision and Applications*, vol. 29, 2018.

[24] J. Ernst, S. Junger, and W. Tschekalinskij, "Messung einer Faserrichtung eines Kohlefaserwerkstoffes und Herstellung eines Objekts in Kohlefaserverbundbauweise," German pat. Patent, 10 2012 220 923.9.

[25] J. Ernst, S. Junger, and W. Tschekalinskij, "Measurement of a fiber direction of a carbon fiber material and fabrication of an object in carbon fiber composite technique," U.S. Patent Patent 9,234,836.

[26] M. Schöberl, K. Kasnakli, and A. Nowak, "Measuring Strand Orientation in Carbon Fiber Reinforced Plastics (CFRP) with Polarization," *World conference on non-destructive testing*, 2016.

[27] A. Keilmann, M. Godehardt, A. Moghiseh, C. Redenbach, and K. Schladitz, "Improved Anisotropic Gaussian Filters," *Image Analysis and Stereology*, vol. 43, 2024. DOI: 10.5566/ias.3023.

[28] M. Duhovic, A. Keilmann, D. Schommer, C. Redenbach, and K. Schladitz, "Quantitative fiber orientation analysis of carbon fiber sheet molding compounds using polarization imaging and X-ray computed tomography," *Com-*

posites Part B: Engineering, vol. 295, 2025. DOI: 10.1016/j.compositesb.2025.112146.

[29] K. Robb, O. Wirjadi, and K. Schladitz, "Fiber Orientation Estimation from 3D Image Data: Practical Algorithms, Visualization, and Interpretation," in *7th International Conference on Hybrid Intelligent Systems (HIS 2007)*, IEEE, 2007. DOI: 10.1109/HIS.2007.26.

[30] T. Lindeberg, "On the axiomatic foundations of linear scale-space: Combining semi-group structure with causality vs. scale invariance," in *Gaussian Scale-Space Theory: Proc. PhD School on Scale-Space Theory*, Kluwer Academic Publishers, 1996.

[31] F. G. A. Faas and L. J. van Vliet, "3D-Orientation Space; Filters and Sampling," in *Image Analysis*, J. Bigun and T. Gustavsson, Eds., red. by G. Goos, J. Hartmanis, and J. van Leeuwen, vol. 2749, Springer, 2003, ISBN: 978-3-540-40601-3 978-3-540-45103-7. DOI: 10.1007/3-540-45103-X_6.

[32] G. Yang, P. Burger, D. Firmin, and S. Underwood, "Structure adaptive anisotropic image filtering," *Image and Vision Computing*, vol. 14, 1996. DOI: 10.1016/0262-8856(95)01047-5.

[33] G. Treece, "Morphology-Based Noise Reduction: Structural Variation and Thresholding in the Bitonic Filter," *IEEE Transactions on Image Processing*, vol. 29, 2020. DOI: 10.1109/TIP.2019.2932572.

[34] D. Eberly, R. Gardner, B. Morse, S. Pizer, and C. Scharlach, "Ridges for image analysis," *Journal of Mathematical Imaging and Vision*, vol. 4, 1994. DOI: 10.1007/BF01262402.

[35] A. F. Frangi, W. J. Niessen, K. L. Vincken, and M. A. Viergever, "Multiscale vessel enhancement filtering," in *Medical Image Computing and Computer-Assisted Intervention — MICCAI'98*, W. M. Wells, A. Colchester, and S. Delp, Eds., vol. 1496, Springer, 1998. DOI: 10.1007/BFb0056195.

[36] L. Haglund, "Adaptive Multidimensional Filtering," Linköping University, 1992.

[37] J. Weickert, "Coherence-Enhancing Diffusion Filtering," *International Journal of Computer Vision*, no. 32, 1999.

[38] M. Krause, J. M. Hausherr, B. Burgeth, C. Herrmann, and W. Krenkel, "Determination of the fibre orientation in composites using the structure tensor and local X-ray transform," *Journal of Materials Science*, vol. 45, 2010. DOI: 10.1007/s10853-009-4016-4.

[39] O. Wirjadi, K. Schladitz, A. Rack, and T. Breuel, "Applications of Anisotropic Image Filters for Computing 2D and 3D-Fiber Orientations," *Stereology and Image Analysis*, 2009.

[40] "Estimating Fibre Direction Distributions of Reinforced Composites from Tomographic Images,"

[41] P. Pinter, S. Dietrich, B. Bertram, L. Kehrer, P. Elsner, and K. Weidenmann, "Comparison and error estimation of 3D fibre orientation analysis of computed tomography image data for fibre reinforced composites," *NDT & E International*, vol. 95, 2018. DOI: 10.1016/j.ndteint.2018.01.001.

[42] C. Lampert and O. Wirjadi, "An Optimal Nonorthogonal Separation of the Anisotropic Gaussian Convolution Filter," *IEEE Transactions on Image Processing*, vol. 15, 2006. DOI: 10.1109/TIP.2006.877501.

[43] K. Schladitz, A. Büter, M. Godehardt, *et al.*, "Non-destructive characterization of fiber orientation in reinforced SMC as input for simulation based design," *Composite Structures*, vol. 160, 2017. DOI: 10.1016/j.compstruct.2016.10.019.

[44] H.-O. Georgii, *Stochastics: Introduction to Probability and Statistics* (De Gruyter Textbook), 2., rev. and extended ed. de Gruyter, 2013, ISBN: 978-3-11-029254-1 978-3-11-029360-9. DOI: 10.1515/9783110293609.fm.

[45] F. ITWM, *MAVI - Modular Algorithms for Volume Images*, 2022.

[46] F. ITWM, *ToolIP - Tool for Image Processing*, 2022.

[47] W. Niblack, *An Introduction to Digital Image Processing*. Prentice-Hall, 1986.

[48] R. C. Gonzalez and R. E. Woods, *Digital Image Processing*. Pearson, 2018, ISBN: 978-0-13-335672-4.

[49] S. J. Sheather and M. C. Jones, "A Reliable Data-Based Bandwidth Selection Method for Kernel Density Estimation," *Journal of the Royal Statistical Society Series B: Statistical Methodology*, vol. 53, 1991. DOI: 10.1111/j.2517-6161.1991.tb01857.x.

[50] G. A. Atkinson, S. O'Hara Nash, and L. N. Smith, "Precision Fibre Angle Inspection for Carbon Fibre Composite Structures Using Polarisation Vision," *Electronics*, vol. 10, 2021. DOI: 10.3390/electronics10222765.

[51] L. Chiominto, G. D'Emilia, and E. Natale, "Using Light Polarization to Identify Fiber Orientation in Carbon Fiber Components: Metrological Analysis," *Sensors*, vol. 24, 2024. DOI: 10.3390/s24175685.

[52] J. Hsieh, *Computed Tomography: Principles, Design, Artifacts, and Recent Advances.* 2003.

[53] L. W. Li, N. A. Rubin, M. Juhl, J.-S. Park, and F. Capasso, "Evaluation and characterization of imaging polarimetry through metasurface polarization gratings," *Applied Optics*, vol. 62, 2023. DOI: 10.1364/AO.480487.

[54] Zhou Wang and A. Bovik, "Mean squared error: Love it or leave it? A new look at Signal Fidelity Measures," *IEEE Signal Processing Magazine*, vol. 26, no. 1, pp. 98–117, Jan. 2009, ISSN: 1053-5888. DOI: 10.1109/MSP.2008.930649.

[55] E. Muñoz-Moreno, R. Cárdenes-Almeida, and M. Martin-Fernandez, "Review of Techniques for Registration of Diffusion Tensor Imaging," in *Tensors in Image Processing and Computer Vision*, S. Aja-Fernández, R. De Luis García, D. Tao, and X. Li, Eds., red. by S. Singh, Springer, 2009, ISBN: 978-1-84882-298-6 978-1-84882-299-3. DOI: 10.1007/978-1-84882-299-3_13.

[56] J. Yang, D. Shen, C. Davatzikos, and R. Verma, "Diffusion Tensor Image Registration Using Tensor Geometry and Orientation Features," in *Medical Image Computing and Computer-Assisted Intervention – MICCAI 2008*, D. Metaxas, L. Axel, G. Fichtinger, and G. Székely, Eds., vol. 5242, Springer,

2008, ISBN: 978-3-540-85989-5 978-3-540-85990-1. DOI: 10.1007/978-3-540-85990-1_109.

[57] H. Altendorf and D. Jeulin, "Random-walk-based stochastic modeling of three-dimensional fiber systems," *Physical Review E*, vol. 83, 2011. DOI: 10.1103/PhysRevE.83.041804.

[58] A. Keilmann, C. Redenbach, and F. Willot, "Increasing Inter-Fiber Contact in the Altendorf-Jeulin model," *Computational Materials Science*, vol. 264, 2026. DOI: 10.1016/j.commatsci.2025.114458.

[59] G. Matheron, *Random Sets and Integral Geometry*. John Wiley & Sons, 1975.

[60] O. Wirjadi, "Models and Algorithms for Image-Based Analysis of Microstructures," TU Kaiserslautern, 2009.

[61] P. Easwaran, "Stochastic geometry models for interacting fibers," TU Kaiserslautern, 2017.

[62] M. Faessel, C. Delisée, F. Bos, and P. Castéra, "3D Modelling of random cellulosic fibrous networks based on X-ray tomography and image analysis," *Composites Science and Technology*, vol. 65, 2005. DOI: 10.1016/j.compscitech.2004.12.038.

[63] P. Townsend, E. Larsson, T. Karlson, *et al.*, "Stochastic modelling of 3D fiber structures imaged with X-ray microtomography," *Computational Materials Science*, vol. 194, 2021. DOI: 10.1016/j.commatsci.2021.110433.

[64] G. Gaiselmann, R. Thiedmann, I. Manke, W. Lehnert, and V. Schmidt, "Stochastic 3D modeling of fiber-based materials," *Computational Materials Science*, vol. 59, 2012. DOI: 10.1016/j.commatsci.2012.02.038.

[65] M. Weber, A. Grießer, D. Mosbach, E. Glatt, A. Wiegmann, and V. Schmidt, "Copula-based modeling and simulation of 3D systems of curved fibers by isolating intrinsic fiber properties and external effects," *Scientific Reports*, vol. 13, 2023. DOI: 10.1038/s41598-023-46644-5.

[66] M. Weber, A. Grießer, E. Glatt, A. Wiegmann, and V. Schmidt, "Modeling Curved Fibers by Fitting R-vine Copulas to their Frenet Representations," *Microscopy and Microanalysis*, vol. 29, 2023. DOI: 10.1093/micmic/ozac030.

[67] Y. Pan, L. Iorga, and A. A. Pelegri, "Analysis of 3D random chopped fiber reinforced composites using FEM and random sequential adsorption," *Computational Materials Science*, vol. 43, 2008. DOI: 10.1016/j.commatsci.2007.12.016.

[68] C. Redenbach and I. Vecchio, "Statistical analysis and stochastic modelling of fibre composites," *Composites Science and Technology*, vol. 71, 2011. DOI: 10.1016/j.compscitech.2010.10.014.

[69] W. Tian, L. Qi, J. Zhou, J. Liang, and Y. Ma, "Representative volume element for composites reinforced by spatially randomly distributed discontinuous fibers and its applications," *Composite Structures*, vol. 131, 2015. DOI: 10.1016/j.compstruct.2015.05.014.

[70] N. Provatas, M. Haataja, J. Asikainen, S. Majaniemi, M. Alava, and T. Ala-Nissila, "Fiber deposition models in two and three spatial dimensions," *Colloids and Surfaces A: Physicochemical and Engineering Aspects*, vol. 165, 2000. DOI: 10.1016/S0927-7757(99)00417-3.

[71] K. J. Niskanen and M. J. Alava, "Planar Random Networks with Flexible Fibers," *Physical Review Letters*, vol. 73, 1994. DOI: 10.1103/PhysRevLett.73.3475.

[72] D. Venkateshan, M. Tahir, H. Vahedi Tafreshi, and B. Pourdeyhimi, "Modeling effects of fiber rigidity on thickness and porosity of virtual electrospun mats," *Materials & Design*, vol. 96, 2016. DOI: 10.1016/j.matdes.2016.01.105.

[73] A. Moghadam, S. Yousefi, H. V. Tafreshi, and B. Pourdeyhimi, "Characterizing nonwoven materials via realistic microstructural modeling," *Separation and Purification Technology*, vol. 211, 2019. DOI: 10.1016/j.seppur.2018.10.018.

[74] S. R. Williams and A. P. Philipse, "Random packings of spheres and spherocylinders simulated by mechanical contraction," *Physical Review E*, vol. 67, 2003. DOI: 10.1103/PhysRevE.67.051301.

[75] N. C. Karayiannis and M. Laso, "Dense and Nearly Jammed Random Packings of Freely Jointed Chains of Tangent Hard Spheres," *Physical Review Letters*, vol. 100, 2008. DOI: 10.1103/PhysRevLett.100.050602.

[76] M. Schneider, "The sequential addition and migration method to generate representative volume elements for the homogenization of short fiber reinforced plastics," *Computational Mechanics*, vol. 59, 2017. DOI: 10.1007/s00466-016-1350-7.

[77] M. Schneider, "An algorithm for generating microstructures of fiber-reinforced composites with long fibers," *International Journal for Numerical Methods in Engineering*, vol. 123, 2022. DOI: 10.1002/nme.7110.

[78] A. Mehta and M. Schneider, "A sequential addition and migration method for generating microstructures of short fibers with prescribed length distribution," *Computational Mechanics*, vol. 70, 2022. DOI: 10.1007/s00466-022-02201-x.

[79] C. Lauff, M. Schneider, J. Montesano, and T. Böhlke, "Generating microstructures of long fiber reinforced composites by the fused sequential addition and migration method," *International Journal for Numerical Methods in Engineering*, 2024. DOI: 10.1002/nme.7573.

[80] C. Lauff, M. Schneider, and T. Böhlke, "Microstructure generation of long fiber reinforced hybrid composites using the fused sequential addition and migration method," *Journal of Thermoplastic Composite Materials*, 2025. DOI: 10.1177/08927057251314425.

[81] C. Lauff, M. Krause, M. Schneider, and T. Böhlke, "On the Influence of the Fiber Curvature on the Stiffness of Long Fiber Reinforced Composites," *International Journal for Numerical Methods in Engineering*, vol. 126, 2025. DOI: 10.1002/nme.70094.

[82] A. Klar, "Interacting fiber structures: Mathematical aspects and applications," *Rivista di Matematica della Universita di Parma*, vol. 10, 2019.

[83] R. Borsche, A. Klar, C. Nessler, A. Roth, and O. Tse, "A Retarded Mean-Field Approach for Interacting Fiber Structures," *Multiscale Modeling & Simulation*, vol. 15, 2017. DOI: 10.1137/151005592.

[84] V. Salnikov, D. Choï, and P. Karamian-Surville, "On efficient and reliable stochastic generation of RVEs for analysis of composites within the framework of homogenization," *Computational Mechanics*, vol. 55, 2015. DOI: 10.1007/s00466-014-1086-1.

[85] A. Bezrukov and D. Stoyan, "Simulation and Statistical Analysis of Random Packings of Ellipsoids," *Particle & Particle Systems Characterization*, vol. 23, 2006. DOI: 10.1002/ppsc.200600974.

[86] L. Chapelle, M. Lévesque, P. Brøndsted, M. R. Foldschack, and Y. Kusano, "Generation of Non-overlapping Fiber Architecture," *Proceedings of the 20th International Conference on Composite Materials*, 2015.

[87] A. Kumar, A. DasGupta, and A. Jain, "Microstructure generation algorithm and micromechanics of curved fiber composites with random waviness," *International Journal of Solids and Structures*, vol. 289, 2024. DOI: 10.1016/j.ijsolstr.2023.112625.

[88] G. Gaiselmann, D. Froning, C. Tötzke, *et al.*, "Stochastic 3D modeling of non-woven materials with wet-proofing agent," *International Journal of Hydrogen Energy*, vol. 38, 2013. DOI: 10.1016/j.ijhydene.2013.04.144.

[89] F. Cartenì, A. Deslauriers, S. Rossi, *et al.*, "The Physiological Mechanisms Behind the Earlywood-To-Latewood Transition: A Process-Based Modeling Approach," *Frontiers in Plant Science*, vol. Volume 9, 2018. DOI: 10.3389/fpls.2018.01053.

[90] R. C. Picu, "Mechanics of random fiber networks—a review," *Soft Matter*, vol. 7, 2011. DOI: 10.1039/c1sm05022b.

[91] J. Xie, Z. Guo, M. Shao, *et al.*, "Mechanics of textiles used as composite preforms: A review," *Composite Structures*, vol. 304, 2023. DOI: 10.1016/j.compstruct.2022.116401.

[92] D. Poquillon, B. Viguier, and E. Andrieu, "Experimental data about mechanical behaviour during compression tests for various matted fibres," *Journal of Materials Science*, vol. 40, 2005. DOI: 10.1007/s10853-005-5070-1.

[93] C. M. Van Wyk, "20—NOTE ON THE COMPRESSIBILITY OF WOOL," *Journal of the Textile Institute Transactions*, vol. 37, 1946. DOI: 10.1080/19447024608659279.

[94] D. Durville, "Numerical simulation of entangled materials mechanical properties," *Journal of Materials Science*, vol. 40, 2005. DOI: 10.1007/s10853-005-5061-2.

[95] A. Karakoç, E. Hiltunen, and J. Paltakari, "Geometrical and spatial effects on fiber network connectivity," *Composite Structures*, vol. 168, 2017. DOI: 10.1016/j.compstruct.2017.02.062.

[96] S. Deogekar, Z. Yan, and R. C. Picu, "Random Fiber Networks With Superior Properties Through Network Topology Control," *Journal of Applied Mechanics*, vol. 86, 2019. DOI: 10.1115/1.4043828.

[97] E. M. Huisman, C. Storm, and G. T. Barkema, "Monte Carlo study of multiply crosslinked semiflexible polymer networks," *Physical Review E*, vol. 78, 2008. DOI: 10.1103/PhysRevE.78.051801.

[98] E. M. Huisman, T. Van Dillen, P. R. Onck, and E. Van Der Giessen, "Three-Dimensional Cross-Linked F-Actin Networks: Relation between Network Architecture and Mechanical Behavior," *Physical Review Letters*, vol. 99, 2007. DOI: 10.1103/PhysRevLett.99.208103.

[99] J. M. Benoit, B. Corraze, and O. Chauvet. "Localization, Coulomb interactions and electrical heating in single-wall carbon nanotubes/polymer composites." arXiv: cond-mat/0204520. (2002), pre-published.

[100] J. Mościński, M. Bargieł, Z. A. Rycerz, and P. W. M. Jacobs, "The Force-Biased Algorithm for the Irregular Close Packing of Equal Hard Spheres," *Molecular Simulation*, vol. 3, 1989. DOI: 10.1080/08927028908031373.

[101] R. Sedgewick, *An Introduction to the Analysis of Algorithms*. Pearson Education India, 2013.

[102] T. Kanit, S. Forest, I. Galliet, V. Mounoury, and D. Jeulin, "Determination of the size of the representative volume element for random composites: Statistical and numerical approach," *International Journal of Solids and Structures*, vol. 40, 2003. DOI: 10.1016/S0020-7683(03)00143-4.

[103] J. Dirrenberger, S. Forest, and D. Jeulin, "Towards gigantic RVE sizes for 3D stochastic fibrous networks," *International Journal of Solids and Structures*, vol. 51, 2014. DOI: 10.1016/j.ijsolstr.2013.10.011.

[104] M. Myllymäki, T. Mrkvička, P. Grabarnik, H. Seijo, and U. Hahn, "Global Envelope Tests for Spatial Processes," *Journal of the Royal Statistical Society Series B: Statistical Methodology*, vol. 79, 2017. DOI: 10.1111/rssb.12172.

[105] C. Fend and C. Redenbach, "Testing complete spatial randomness of point processes with Monte Carlo tests: A comparative power study," *Journal of Statistical Computation and Simulation*, 2026. DOI: 10.1080/00949655.2026.2625783.

[106] J. Møller and R. P. Waagepetersen, *Statistical Inference and Simulation for Spatial Point Processes* (Monographs on Statistics and Applied Probability 100). Boca Raton: Chapman & Hall/CRC, 2004, ISBN: 978-1-58488-265-7.

[107] *GeoDict*, Math2Market GmbH, 2025.

[108] *ConductoDict*, Math2Market GmbH, 2021.

[109] C. Surulescu, E. Grosjean, M. Dauner, *et al.*, "An in-silico approach to meniscus tissue regeneration: Modeling, numerical simulation, and experimental analysis," *Applied Mathematical Modelling*, vol. 151, 2026. DOI: 10.1016/j.apm.2025.116535.

[110] *MVT-CT*. [Online]. Available: rptu.de/projekte/mso/ct-lab/mvt-ct.

[111] N. Otsu, "A Threshold Selection Method from Gray-Level Histograms," *IEEE Transactions on Systems, Man, and Cybernetics*, vol. 9, 1979. DOI: 10.1109/TSMC.1979.4310076.

[112] Fraunhofer ITWM, *TexMath*, 2026. [Online]. Available: itwm.fraunhofer.de/texmath.

[113] N. Alaux, C. Marton, J. Steinmann, *et al.*, "Whole-life greenhouse gas emission reduction and removal strategies for buildings: Impacts and diffusion potentials across EU Member States," *Journal of Environmental Management*, vol. 370, 2024. DOI: 10.1016/j.jenvman.2024.122915.

[114] A. Amiri, J. Ottelin, J. Sorvari, and S. Junnila, "Cities as carbon sinks—classification of wooden buildings," *Environmental Research Letters*, vol. 15, 2020. DOI: 10.1088/1748-9326/aba134.

[115] J. Shao, *Mathematical Statistics* (Springer Texts in Statistics). Springer, 1999, ISBN: 978-0-387-98674-6 978-0-387-22759-7. DOI: 10.1007/b98900.

[116] A. Nair, K. Schladitz, C. Redenbach, and M. Kronenberger. "Separation and analysis of wood fibers and their contacts in insulation mats." (In preparation), pre-published.

[117] W. N. Venables and B. D. Ripley, *Modern Applied Statistics with S*, Fourth. New York: Springer, 2002, ISBN: 0-387-95457-0.

[118] S. Linden, A. Wiegmann, and H. Hagen, "The LIR space partitioning system applied to the Stokes equations," *Graphical Models*, vol. 82, 2015. DOI: 10.1016/j.gmod.2015.06.003.

[119] M. Schneider, M. Josien, and F. Otto, "Representative volume elements for matrix-inclusion composites - a computational study on the effects of an improper treatment of particles intersecting the boundary and the benefits of periodizing the ensemble," *Journal of the Mechanics and Physics of Solids*, vol. 158, 2022. DOI: 10.1016/j.jmps.2021.104652.

[120] A. Saggion, R. Faraldo, and M. Pierno, *Thermodynamics: Fundamental Principles and Applications* (UNITEXT for Physics). Springer, 2019, ISBN: 978-3-030-26975-3 978-3-030-26976-0. DOI: 10.1007/978-3-030-26976-0.

[121] V. Shiryaev and J. Orlik, "A one-dimensional computational model for hyperelastic string structures with Coulomb friction," *Mathematical Methods in the Applied Sciences*, vol. 40, 2017. DOI: 10.1002/mma.4005.

List of Tables

2.1.1 The density of the multivariate von Mises-Fisher distribution with concentration parameters κ_1, κ_2 and $\mu' = (1,0,0)^T$ and $\mu'' = (0,1,0)^T$. For each plot, yellow indicates the maximum of the density. Hence, the plots do not use the same color scale for the sake of visibility. . . 10

3.3.1 Mean angular deviation (MAD) and area fractions of deviation categories for the surface layers of each specimen. 40

4.2.1 Fibers generated by the Altendorf-Jeulin model for different concentration parameters κ_1, κ_2. 49

4.5.1 The number of realizations necessary for a given volume and characteristic for a relative precision of 1%. 70

5.1.1 ACG parameter estimates for the fiber orientation of the scaffolds. . 92

5.1.2 ACG parameter estimates for the fiber orientation of sample 1. 92

5.2.1 Percentiles of the projection area weighted geodesic length for fiber objects measured by Fraunhofer WKI. B3, B4, B5, and B6 are commercial products. 97

5.2.2 Percentiles of the projection area weighted geodesic thickness for fiber objects measured by Fraunhofer WKI. 97

5.2.3 Estimated parameters for the lognormal distributions of the length $(\hat{\nu}_\ell, \hat{\sigma}_\ell)$ and bundle thickness $(\hat{\nu}_b, \hat{\sigma}_b)$. $\hat{\nu}'$ and $\hat{\sigma}'$ are the corresponding mean and standard deviation. 98

A.1.1 Overview of parameter combinations used in the experiments in Section 4.5. All parameters were combined with $\beta = 0.1, 0.5, 1.0, 2.0, 3.0$ and $\varepsilon = 0.1, 0.2, 0.3, 0.4, 0.5, 1.0$. Note that the number of fibers depends on the image size s. 140

C.0.1 Parameter choices for the thickness of single fibers. Values in bold were observed for product data, see Section 5.2.1. 152

C.0.2 Parameter choices for the thickness of fiber bundles. Values in bold were observed for product data, see Section 5.2.1. 153

C.0.3 Parameter choices for the length of fibers and fiber bundles. Values in bold were observed for product data, see Section 5.2.1. 154

List of Figures

2.1.1 Sketches of polar coordinates in 2D (left) and 3D (right). 5

2.1.2 Illustration of pitfalls when calculating the mean direction. 7

2.1.3 Density plots for the von Mises-Fisher distribution on the sphere S^2 for varying κ. The mean μ (if existent) is directed out of the paper plane. 8

2.1.4 Plot of the Schladitz-distribution for varying parameters β. 11

2.2.1 Rendering of a Boolean Model realizations with cylinders as grains. . 16

2.2.2 Sketches of edge treatment for Boolean models of cylinders. 17

2.2.3 Poisson Line Process in 2D. 19

3.1.1 3D CT scan sample preparation. 23

3.1.2 Left: Positioning of the C-SMC specimen in the scanning chamber of the Xradia 520 Versa 3D X-ray microscope. Right: µCT scan of the stacked tiles 1-3 of specimen 53. 24

3.2.1 The Gaussian ellipse, i.e., contour line of the Gaussian function with major axis v_1 and minor axis v_2. 26

3.2.2 Visualization of the experimental data set for varying contrast c see Eq. 3.2.7. 29

3.2.3 Error plot for the experimental setup where orientation estimation methods are applied to synthetic fibers that are overlayed with noise. The x-axis depicts the contrast c between noise and the synthetic fibers, see Eq. 3.2.7. The y-axis depicts the MAAE: For each contrast, method, filter condition and fiber diameter and noise image, the maximal angular error was calculated over the fiber directions $\theta = 0°, ..., 179°$. Then, the mean was taken over all 50 noise images. The mean is depicted as a point symbol, the standard deviation is depicted with bars. Note, however, that the standard deviations are small and therefore the bars delimiting the interval are in most cases covered by the symbol for the mean value. 31

3.2.4 Direction estimation of SMC with carbon fibers. The directions are color-coded, see color wheel at the top-right side. 34

3.3.1 Schematic visualization of the registration process. The polarization image is depicted in black-white, whereas the CT image is depicted in shades of blue. For reference between depictions, one shared image edge is depicted in red and another one in dashed green. 35

3.3.2 Surface layer of specimen 19 (µCT scans). 38

3.3.3 Results of the top layer from specimen 19 for both imaging modalities. 39

3.3.4 Kernel density estimates for the fiber orientation distribution of specimen 19 (all 9 tiles combined), calculated from its µCT scans. See Section 3.3.2 for the difference between the orientation distribution as shown here and the local orientation as shown in Fig. 3.3.3a 41

3.3.5 Kernel density estimates for the fiber orientation distributions of the individual tiles of specimen 19, calculated from its µCT scans. See Section 3.3.2 for the difference between the orientation distribution as shown here and the local orientation as shown in Fig. 3.3.3a 42

4.2.1 Sketches of forces in the Altendorf-Jeulin model. 50

4.2.2 Plot of the smoothing factor for $0 < \alpha_s < \alpha_e$. 51

4.3.1 Reference image of a wood fiber bundle. 54

4.3.2 Sketch of a fiber bundle with 4 fibers along ℓ_1 and 3 fibers along ℓ_2. The remaining 6 fibers are omitted for better visibility. 55

4.3.3 Sketch of a cuboidal bundle and a fiber part. The fiber direction $\mu_{\mathcal{F},m}$ is close to v_1, so packing forces will act along v_2 or v_B. Note that the remaining fiber balls are omitted for better visibility. 57

4.4.1 Sketch for the degrees of closeness on the level of balls. 60

4.4.2 Sketch for the contact areas between fibers. Blue indicates the contact between balls as described by $\mathcal{E}_0$. Red indicates the ball chain sections creating the contact as described by $\bar{\mathcal{E}}_0 \backslash \mathcal{E}_0$. The gray area indicates the intuitive contact area. 61

4.4.3 Sketch for the contact candidates (indicated by blue lines) and shortlist (indicated by red lines) for the interaction distance $\varepsilon = \frac{3}{4}r$. 62

4.5.1 Plot for the runtime depending on the window size for medium fiber length and volume fraction, $\beta = 1.0$ and the curvature $\kappa_1 = 10, \kappa_2 = 100$. The scale of the window size is transformed cubically (corresponding to the volume). Bars indicate the standard deviation, the line in blue indicates a fitted model. 69

4.5.2 Plot of the contact intensity λ_c w.r.t. the parameter of the orientation distribution for varying interaction distance ε (in colour) for the experimental setup described in Section 4.5.1. Note that $\kappa_1 = 10, \kappa_2 = 100$. 71

4.5.3 Plot of the clot density λ_{cl} w.r.t. the parameter of the orientation distribution for varying interaction distance ε (in colour) for the experimental setup described in Section 4.5.1. Note that $\kappa_1 = 10, \kappa_2 = 100$. 72

4.5.4 Plot of the contact intensity of the Altendorf-Jeulin model, the contact model, and the analytically determined formula by Toll. Note that $\kappa_1 = 10, \kappa_2 = 100$. 73

4.5.5 Plot of the distribution of the number of contacts of individual fibers for the Altendorf-Jeulin model and the contact model (colored bars). Solid lines represent Poisson distributions with the same mean as that of the two models (left and right) as well as that predicted by the Toll model (in-between). Note that $\kappa_1 = 10, \kappa_2 = 100$. 74

4.5.6 Plot of the spatial statistic K regarding the contact positions in the Altendorf-Jeulin model. The right plot reveals the behavior for $r \leq 5$, i.e., the order of magnitude of the fiber thickness. The gray area indicates the global envelope of the test statistic. Red dots indicate function points that lie outside the envelope. Note that $\kappa_1 = 10, \kappa_2 = 100$. 75

4.5.7 Plot of the spatial statistic G regarding the contact positions in the Altendorf-Jeulin model. The right plot reveals the behavior for $r \leq 5$, i.e., the order of magnitude of the fiber thickness. The gray area indicates the global envelope of the test statistic. Red dots indicate function points that lie outside the envelope. Note that $\kappa_1 = 10, \kappa_2 = 100$. 75

4.5.8 Plots of the deviation from the direction parameter β relative to the input value. The estimated values of β for the contact packing and the Altendorf-Jeulin packing correspond so closely to the values upon fiber generation that the plots overlay each other. Bars indicate standard deviations, but are often not visible because they are so low. Note that low deviation around 0 indicates high accuracy, whereas high values indicate low accuracy. Note that $\kappa_1 = 10, \kappa_2 = 100$. . . . 78

4.5.9 Plots of the deviation of the curvature parameters $\kappa_1 = 10$ and $\kappa_2 = 100$ relative to the input values after fiber generation, Altendorf-Jeulin packing, and contact packing each. Bars indicate standard deviations, but are often not visible because they are so low. Note that low values for the absolute deviation around 0 indicate high accuracy, whereas high values indicate low accuracy. 79

4.5.10 Deviation of the estimated parameter values of the contact model relative to the Altendorf-Jeulin model. Bars indicate standard deviations, but are often not visible because they are so low. Note that low values for the absolute deviation around 0 indicate high accuracy, whereas high values indicate low accuracy. In this setup, the curvature parameters are $\kappa_1 = 10, \kappa_2 = 100$. 80

4.5.11 Sensitivity study of the threshold t to remove shortlisted candidates. Bars indicate standard deviations. Note that low values for the absolute deviation around 0 indicate high accuracy, whereas high values indicate low accuracy. In this setup, the aspect ratio is $a = 50$, the volume fraction $V_V = 30\%$, $\beta = 1.0$, $\varepsilon = 0.1$, and the curvature parameters are $\kappa_1 = 10, \kappa_2 = 100$. 81

5.1.1 Sectional image of the CT scan of sample 1 (left) with a size of 2 600 × 2 600 pixels, i.e., approx. 10.35 mm × 10.35 mm. The area marked by a red box is magnified 5 times (right) to enhance the visibility of the fiber structure. 87

5.1.2 Sectional image of the CT scan of higher resolution with a size of 3 535 × 1 366 voxels, i.e., approx. 8.66 mm × 3.35 mm. 87

5.1.3 The bright spots are artifacts in the high-resolution scan. The sectional images are of size 2 148 × 837 pixels, i.e., 5.26 mm × 2.05 mm.The artifact removal is described in Section 5.1.2.2. 89

5.1.4 Spherical density plots of the local fiber orientation distribution for sample 1. The left plot shows the empirical orientation distribution, meaning the distribution that is directly estimated from the observed orientations. The right plot shows the density of the ACG model fitted to the observed orientations. The color scale is the same in both plots. See Fig. 5.1.5 for the validation of the goodness of fit. . . 91

5.1.5 QQ plots for the ACG parameter estimation of sample 1. Separate plots for colatitude and longitude of the spherical coordinates. Note that the colatitude and longitude are given in radian. The QQ lines are close to the reference line, which indicates a good fit. 91

5.1.6 QQ plots for the ACG parameter estimation of sample 1 scanned in high resolution. Separate plots for colatitude and longitude of the spherical coordinates. Note that the colatitude and longitude are given in radian. The QQ lines are close to the reference line, which indicates a good fit. 92

5.1.7 Visualization of the nonwoven scaffold model using TexMathVisualizer [112]. 93

5.2.1 Rendering of CT images taken from wood-fiber insulation boards. . . 96

5.2.2 Rendering of a Boolean model realization with default parameters ($\nu_\ell = 7.27$, $\sigma_\ell = 0.88$, $\nu_b = 5.36$, $\sigma_b = 0.69$, $\nu_t = 33.89$, $\sigma_t = 8.36$, $\beta = 2$, $V_{VS} = 5.6\,\%$, and $V_{VB} = 2.4\,\%$). 100

5.2.3 Simulated thermal conductivities for the Boolean model realizations. The plots are grouped according to the varied parameter sets. The plot points indicate the mean value, bars indicate the standard deviation. 101

5.3.4 Plots of the mean and variance of the thermal conductivity w.r.t. the window volume. The line in blue indicates the fitted model for image volumes larger or equal to $1\,024^3$ with $K = 8.37$ and $\alpha = 1.02$. 105

5.3.5 Plots of the mean and variance of the radiative conductivity w.r.t. to the window volume. The line in blue indicates the fitted model for image volumes larger or equal to $1\,024^3$ with $K = 9.32$ and $\alpha = 1.09$. 106

5.3.6 Plots of the mean and variance of the stiffness w.r.t. to the window volume. The line in blue indicates the fitted model for image volumes larger or equal to $1\,024^3$ with $K = 3\,102.07$ and $\alpha = 1.05$. 106

5.3.7 Plots of the mean thermal conductivity for each model. Bars indicate the standard deviation; however, they may not be visible because they are so low. 108

5.3.8 Plots of the mean radiative conductivity for each model. Bars indicate the standard deviation; however, they may not be visible because they are so low. 109

5.3.9 Plots of the mean total conductivity for each model. Bars indicate the standard deviation; however, they may not be visible because they are so low. 110

5.3.10 Plots of the mean stiffness for each model. Bars indicate the standard deviation; however, they may not be visible because they are so low.. 111

A.2.1 Plots of the variance of properties w.r.t. the window volume. The line in blue indicates the fitted model. 141

A.3.1 Plot of the contact intensity λ_c and the expected number of clots per fiber λ_{clF} w.r.t. the parameter of the orientation distribution for varying interaction distance ε (in color) for straight fibers with $\kappa_1, \kappa_2 = 100$, see Section 4.5.3. 141

A.3.2 Plot of the contact intensity λ_c and the expected number of clots per fiber λ_{clF} w.r.t. the parameter of the orientation distribution for varying interaction distance ε (in color) for curvy fibers with $\kappa_1, \kappa_2 = 10$, see Section 4.5.3. 142

A.3.3 Plot of the contact intensity λ_c and he expected number of clots per fiber λ_{clF} w.r.t. the parameter of the orientation distribution for varying interaction distance ε (in color) for very curvy fibers with $\kappa_1, \kappa_2 = 1$, see Section 4.5.3. 142

A.3.4 Mean absolute angular error (MAAE) of the angles of incident edges for the Altendorf-Jeulin model and the contact model compared to the original fiber model. Bars indicate standard deviations, but are often not visible because they are so low. In this setup, the curvature parameters are $\kappa_1 = 10, \kappa_2 = 100$. 143

A.3.5 Accuracy plots for the contact model relative to the Altendorf-Jeulin model for the special case of straight fibers ($\kappa_1, \kappa_2 = 100$). Bars indicate standard deviations. 144

A.3.6 Accuracy plots for the contact model relative to the Altendorf-Jeulin model for the special case of curvy fibers ($\kappa_1, \kappa_2 = 10$). 144
A.3.7 Accuracy plots for the contact model relative to the Altendorf-Jeulin model for the special case of very curvy fibers ($\kappa_1, \kappa_2 = 1$). 145
A.3.8 Plot of the spatial statistics regarding the contact positions in the contact model. The gray area indicates the global envelope of the test statistic. Red dots indicate function points that lie outside the envelope. Note that $\kappa_1 = 10, \kappa_2 = 100$. 145

B.0.1 QQ plots for the ACG parameter estimation of sample 2. Separate plots for colatitude and longitude of the spherical coordinates. The QQ lines are close to the reference line, which indicates a good fit. . . 147
B.0.2 QQ plots for the ACG parameter estimation of sample 3. Separate plots for colatitude and longitude of the spherical coordinates. The QQ lines are close to the reference line, which indicates a good fit. . . 148
B.0.3 QQ plots for the ACG parameter estimation of sample 4. Separate plots for colatitude and longitude of the spherical coordinates. The QQ lines are close to the reference line, which indicates a good fit. . . 148
B.0.4 QQ plots for the ACG parameter estimation of sample 5. Separate plots for colatitude and longitude of the spherical coordinates. The QQ lines are close to the reference line, which indicates a good fit. . . 149
B.0.5 QQ plots for the ACG parameter estimation of sample 6. Separate plots for colatitude and longitude of the spherical coordinates. The QQ lines are close to the reference line, which indicates a good fit. . . 149

Appendix A

Appendix to Section 4.5

A.1 Parameter combinations

In Section 4.5.1, we explained the experimental setup for validating the contact model rather illustratively, omitting exact parameters. Here, in Table A.1.1, we provide detailed input parameters for the Altendorf-Jeulin and the contact model.

Aspect ratio	Radius	Length	V_V	#fibers	κ_1	κ_2	τ	d_c
10	2	40	$\sim 10\%$	$400s^3$	10	100	0.0	0
10	2	40	$\sim 20\%$	$800s^3$	10	100	0.0	0
10	2	40	$\sim 30\%$	$1\,200s^3$	10	100	0.0	0
30	2	120	$\sim 10\%$	$133s^3$	10	100	0.0	0
30	2	120	$\sim 20\%$	$266s^3$	10	100	0.0	0
30	2	120	$\sim 30\%$	$400s^3$	10	100	0.0	0
50	2	200	$\sim 10\%$	$80s^3$	10	100	0.0	0
50	2	200	$\sim 20\%$	$160s^3$	10	100	0.0	0
50	2	200	$\sim 30\%$	$240s^3$	10	100	0.0	0
30	2	120	$\sim 20\%$	$266s^3$	10	10	0.0	0
30	2	120	$\sim 20\%$	$266s^3$	100	100	0.0	0
30	2	120	$\sim 20\%$	$266s^3$	1	1	0.0	0

Table A.1.1: Overview of parameter combinations used in the experiments in Section 4.5. All parameters were combined with $\beta = 0.1, 0.5, 1.0, 2.0, 3.0$ and $\varepsilon = 0.1, 0.2, 0.3, 0.4, 0.5, 1.0$. Note that the number of fibers depends on the image size s.

A.2 Fitted Model for the Representative Volume Element

Fig. A.2.1 shows the variance plots w.r.t. the volume window, which is used in Section 4.5.2, together with their fitted models. These are used for the RVE size-number estimation. Note that we only present the plot for $Z = \lambda_{cF}, \lambda_{clF}$ as λ_c is a multiple of λ_{cF} in this case due to a constant λ_F. Note that the fitted models correspond closely to the observed variances.

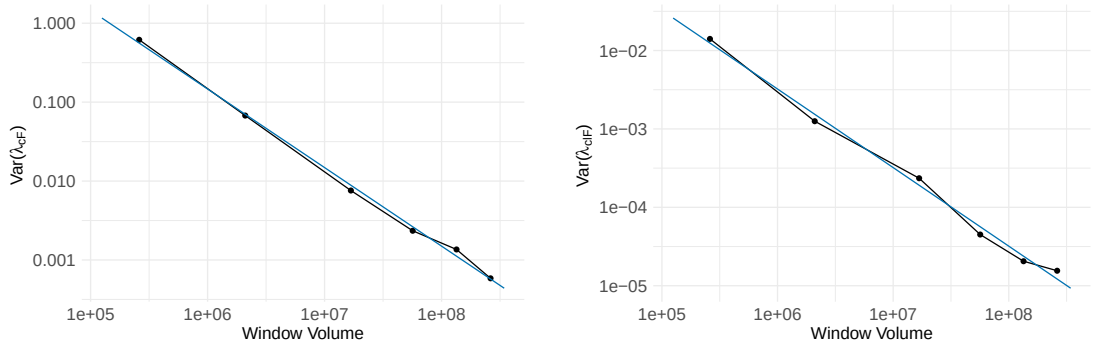

Figure A.2.1: Plots of the variance of properties w.r.t. the window volume. The line in blue indicates the fitted model.

A.3 Validation Plots

In Section 4.5, the simulation results were shown for the main setup of moderate fiber curvature $\kappa_1 = 10, \kappa_2 = 100$. Fig. A.3.1 shows the impact of contact distance ε on both the contact intensity λ_c and the expected number of clots per fiber λ_{clF} for straight fibers, so curvature parameters $\kappa_1, \kappa_2 = 100$. Fig. A.3.2 shows these results for curvy fibers, meaning curvature parameters $\kappa_1, \kappa_2 = 10$, and Fig. A.3.3 shows these results for very curvy fibers, meaning curvature parameters $\kappa_1, \kappa_2 = 1$. Their behavior is similar to fibers with moderate curvature $\kappa_1 = 10, \kappa_2 = 100$, yet differ in the specific values and observed variance of λ_c and λ_{clF}.

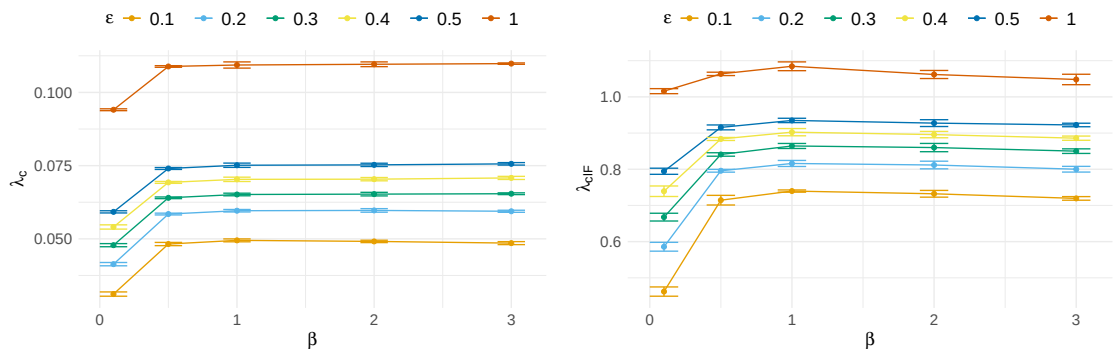

Figure A.3.1: Plot of the contact intensity λ_c and the expected number of clots per fiber λ_{clF} w.r.t. the parameter of the orientation distribution for varying interaction distance ε (in color) for straight fibers with $\kappa_1, \kappa_2 = 100$, see Section 4.5.3.

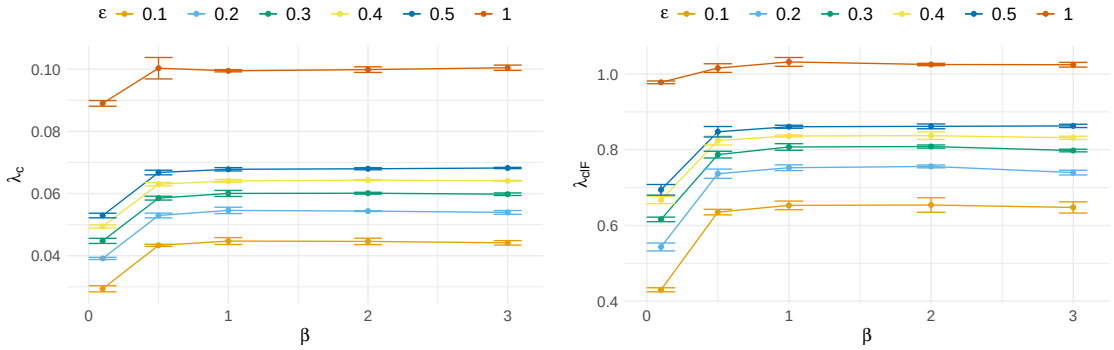

Figure A.3.2: Plot of the contact intensity λ_c and the expected number of clots per fiber λ_{clF} w.r.t. the parameter of the orientation distribution for varying interaction distance ε (in color) for curvy fibers with $\kappa_1, \kappa_2 = 10$, see Section 4.5.3.

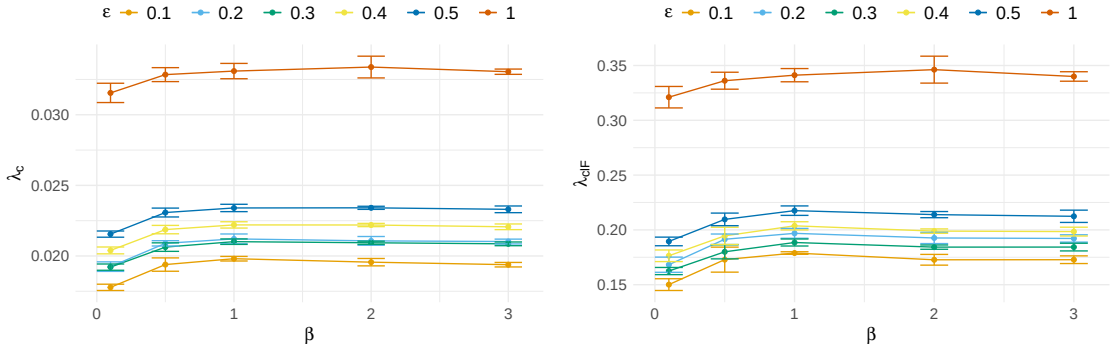

Figure A.3.3: Plot of the contact intensity λ_c and he expected number of clots per fiber λ_{clF} w.r.t. the parameter of the orientation distribution for varying interaction distance ε (in color) for very curvy fibers with $\kappa_1, \kappa_2 = 1$, see Section 4.5.3.

Fig. A.3.5 presents relative deviation of estimated parameters for rather straight fibers ($\kappa_1, \kappa_2 = 100$) relative to the corresponding Altendorf-Jeulin model and their MAAE for the fiber curvature. Fig. A.3.5 shows the analogous plot for curvy fibers ($\kappa_1, \kappa_2 = 10$) and Fig. A.3.7 for very curvy fibers ($\kappa_1, \kappa_2 = 1$). For very curvy fibers, the MAAE is surprisingly high after the Altendorf-Jeulin packing. This is likely due to the strong crimping of these fibers yielding self-overlaps. Here, the MAAE does not seem to be a helpful parameter. For the relative deviation to the input values, all fibers show acceptable deviation. Notably, there is smaller deviation for curvy fibers after contact packing, possibly because contact packing introduces needs to

introduce more curvature to straight fibers in order to yield the contact areas.

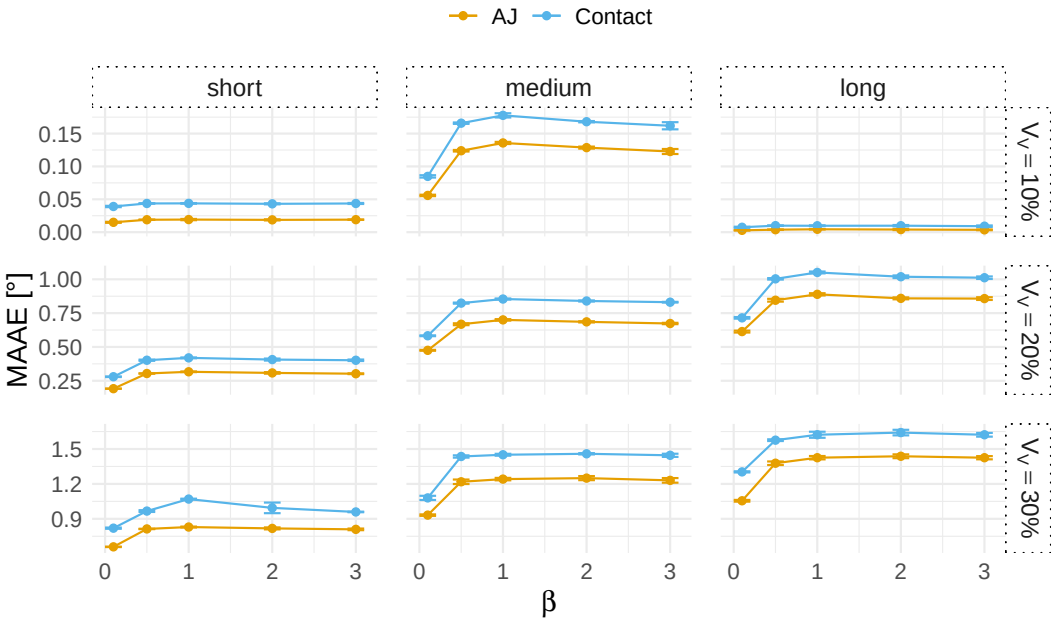

Figure A.3.4: Mean absolute angular error (MAAE) of the angles of incident edges for the Altendorf-Jeulin model and the contact model compared to the original fiber model. Bars indicate standard deviations, but are often not visible because they are so low. In this setup, the curvature parameters are $\kappa_1 = 10, \kappa_2 = 100$.

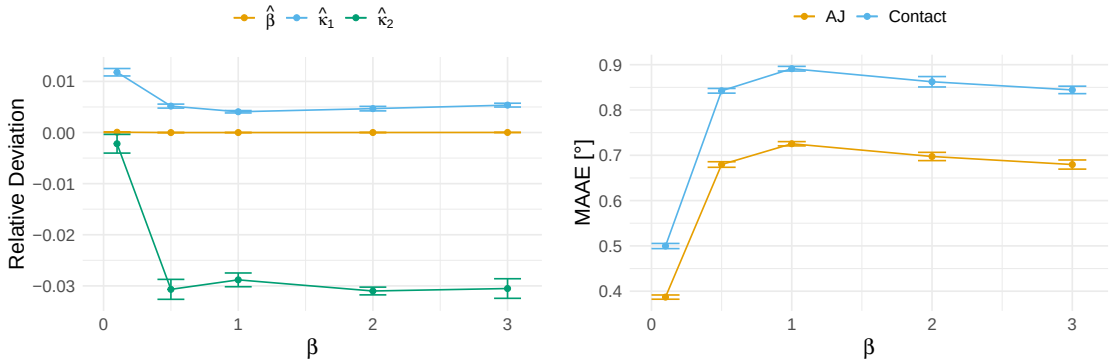

(a) Relative deviations of input parameter values.

(b) Mean absolute angular error (MAAE) of the angles of incident edges for the Altendorf-Jeulin model and the contact model compared to the original fiber model.

Figure A.3.5: Accuracy plots for the contact model relative to the Altendorf-Jeulin model for the special case of straight fibers ($\kappa_1, \kappa_2 = 100$). Bars indicate standard deviations.

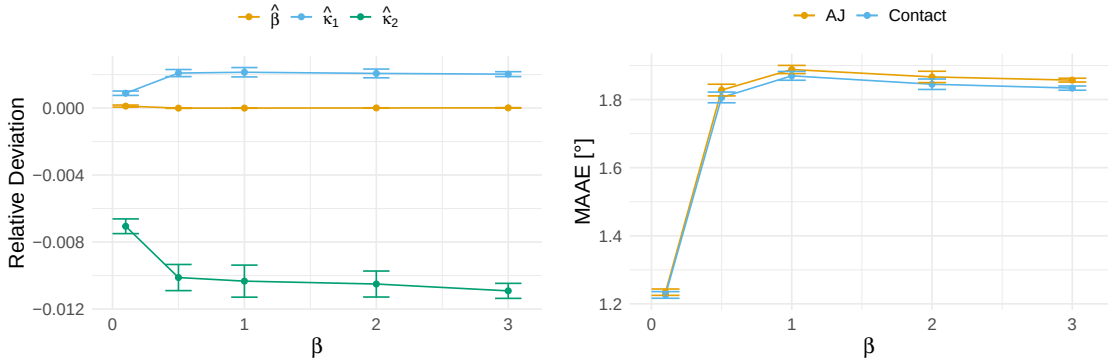

(a) Relative deviations of input parameter values.

(b) Mean absolute angular error (MAAE) of the angles of incident edges for the Altendorf-Jeulin model and the contact model compared to the original fiber model.

..

Figure A.3.6: Accuracy plots for the contact model relative to the Altendorf-Jeulin model for the special case of curvy fibers ($\kappa_1, \kappa_2 = 10$).

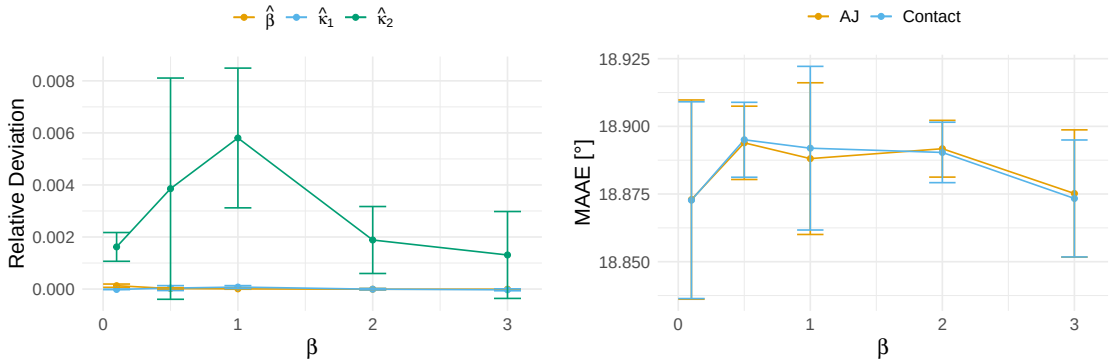

(a) Relative deviations of input parameter values.

(b) Mean absolute angular error (MAAE) of the angles of incident edges for the Altendorf-Jeulin model and the contact model compared to the original fiber model.

Figure A.3.7: Accuracy plots for the contact model relative to the Altendorf-Jeulin model for the special case of very curvy fibers ($\kappa_1, \kappa_2 = 1$).

Fig. A.3.8 shows the K- and G-Test for the default setup after contact packing.

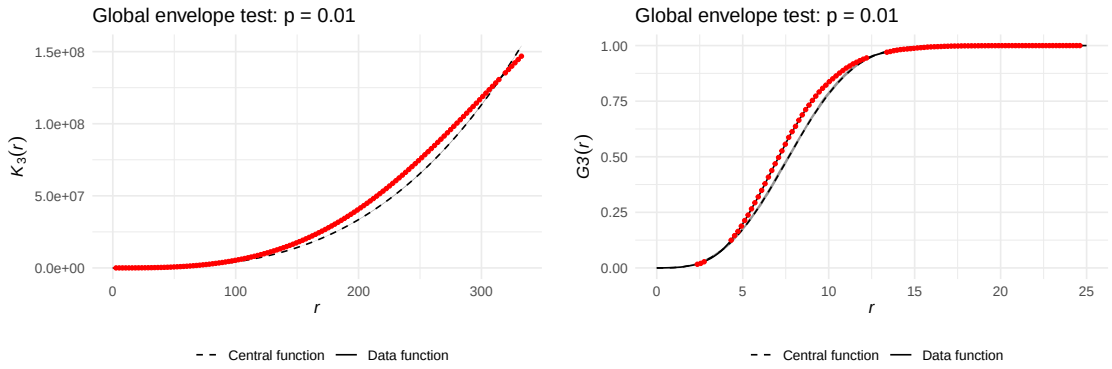

Figure A.3.8: Plot of the spatial statistics regarding the contact positions in the contact model. The gray area indicates the global envelope of the test statistic. Red dots indicate function points that lie outside the envelope. Note that $\kappa_1 = 10, \kappa_2 = 100$.

Appendix B

Appendix to Section 5.1

Fig. B.0.1 to Fig. B.0.5 depict the QQ plots for the corresponding fitted distributions in Section 5.1. Each of them indicate a good fit as their lines are close to the reference line.

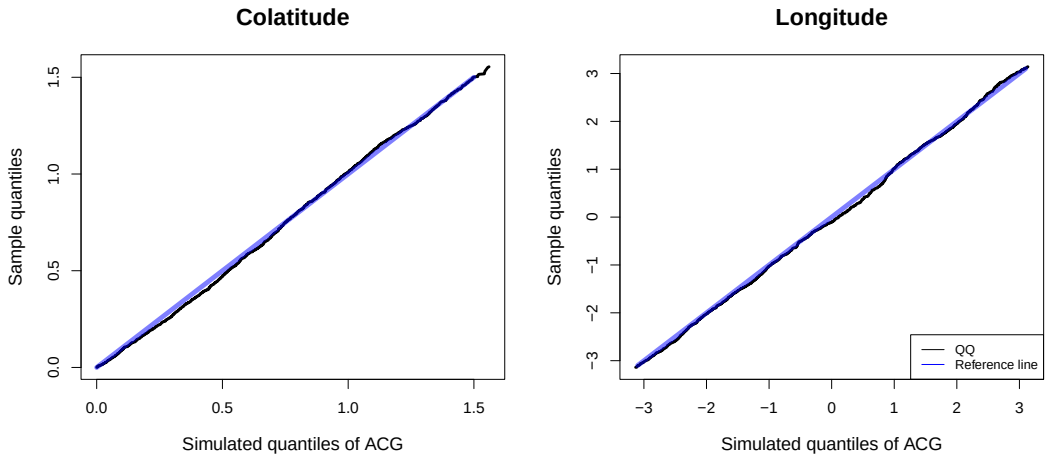

Figure B.0.1: QQ plots for the ACG parameter estimation of sample 2. Separate plots for colatitude and longitude of the spherical coordinates. The QQ lines are close to the reference line, which indicates a good fit.

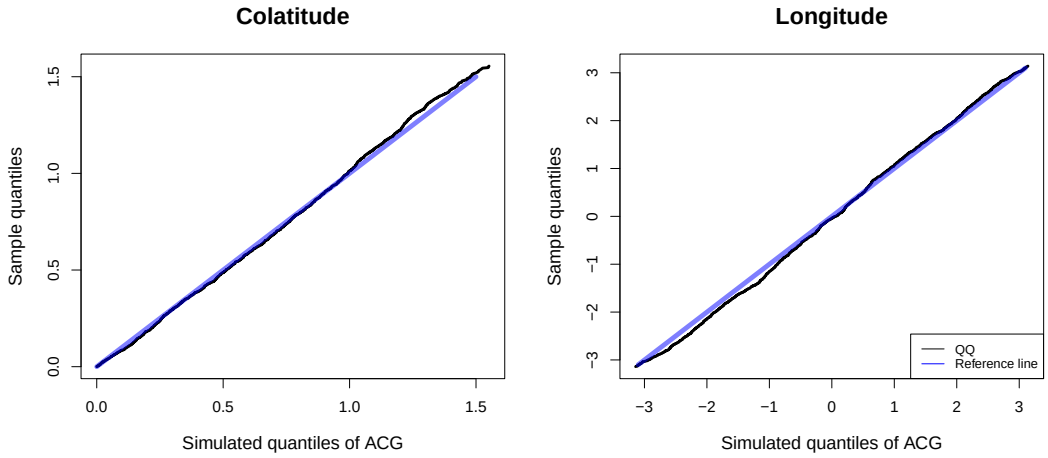

Figure B.0.2: QQ plots for the ACG parameter estimation of sample 3. Separate plots for colatitude and longitude of the spherical coordinates. The QQ lines are close to the reference line, which indicates a good fit.

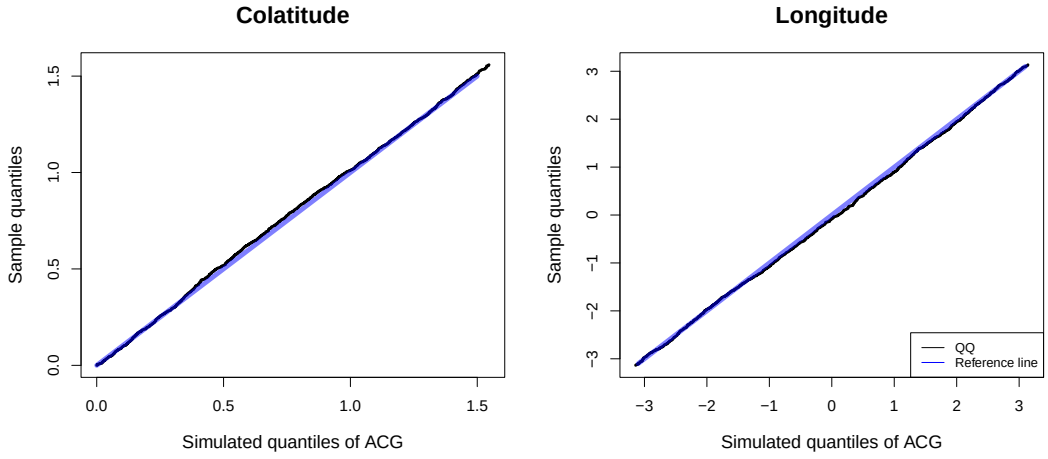

Figure B.0.3: QQ plots for the ACG parameter estimation of sample 4. Separate plots for colatitude and longitude of the spherical coordinates. The QQ lines are close to the reference line, which indicates a good fit.

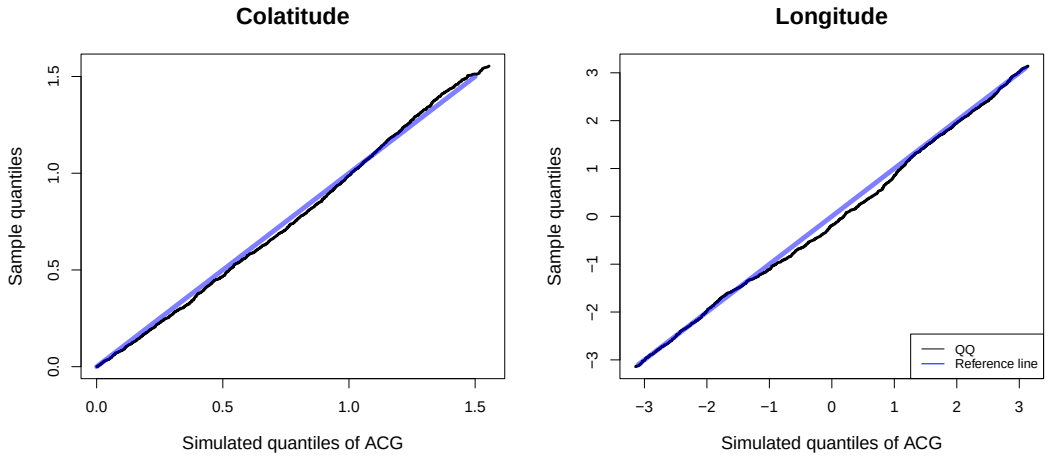

Figure B.0.4: QQ plots for the ACG parameter estimation of sample 5. Separate plots for colatitude and longitude of the spherical coordinates. The QQ lines are close to the reference line, which indicates a good fit.

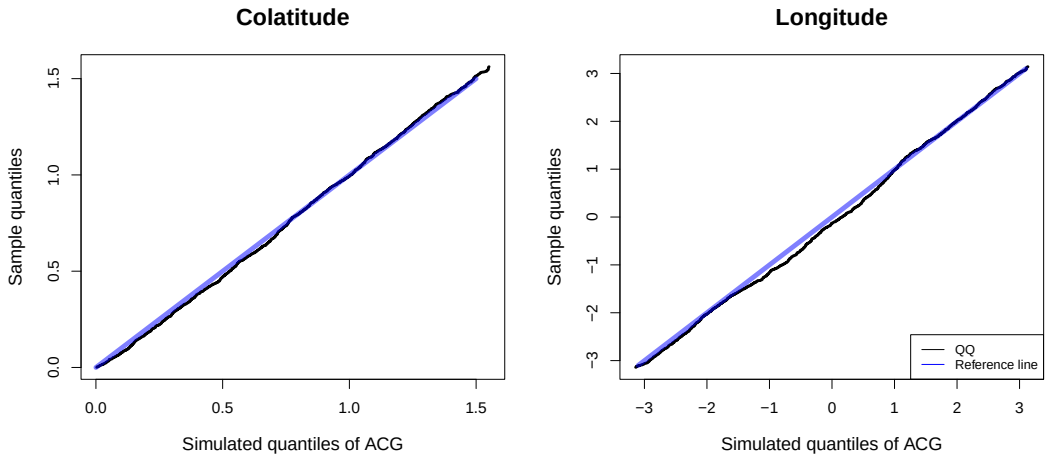

Figure B.0.5: QQ plots for the ACG parameter estimation of sample 6. Separate plots for colatitude and longitude of the spherical coordinates. The QQ lines are close to the reference line, which indicates a good fit.

Appendix C

Appendix to Section 5.2

Section 5.2.2 describes the parameter choice for realizations of a Boolean model representing wood fiber insulation mats. On these, thermal conductivity is simulated. The parameters are varied systematically, and the Table C.0.1 - C.0.3 give an overview over the parameter choices for the grain shapes.

Table C.0.1: Parameter choices for the thickness of single fibers. Values in bold were observed for product data, see Section 5.2.1.

ν_t	σ_t
30	7.5
30	8.36
30	9.2
33.89	7.5
33.89	**8.36**
33.89	9.2
38	7.5
38	8.36
38	9.2

Table C.0.2: Parameter choices for the thickness of fiber bundles. Values in bold were observed for product data, see Section 5.2.1.

ν_b	ν_b'	σ_b	σ_b'
4.92	170	0.66	125.43
4.84	170	0.76	151.31
4.67	170	0.97	212.45
5.17	**206.37**	**0.56**	**125.43**
5.11	206.37	0.66	151.31
4.97	206.37	0.85	212.45
5.34	236.71	0.50	125.43
5.30	**236.71**	**0.59**	**151.31**
5.17	236.71	0.77	212.45
5.51	271.27	0.44	125.43
5.47	271.27	0.52	151.31
5.36	**271.27**	**0.69**	**212.45**
5.64	305	0.40	125.43
5.61	305	0.47	151.31
5.52	305	0.63	212.45

Table C.0.3: Parameter choices for the length of fibers and fiber bundles. Values in bold were observed for product data, see Section 5.2.1.

ν_ℓ	ν'_ℓ	σ_ℓ	σ'_ℓ
6.96	1 450	0.80	1 383.94
6.87	1 450	0.91	1 646.18
6.65	1 450	1.12	2 293.66
7.15	**1 662.50**	**0.73**	**1 383.94**
7.07	1 662.50	0.83	1 646.18
6.88	1 662.50	1.03	2 293.66
7.3	1 850	0.67	1 383.94
7.23	1 850	0.76	1 646.18
7.06	1 850	0.96	2 293.66
7.36	1 934.68	0.64	1 383.94
7.29	**1 934.68**	**0.74**	**1 646.18**
7.13	1 934.68	0.94	2 293.66
7.48	2 112.83	0.60	1 383.94
7.41	2 112.83	0.69	1 646.18
7.27	**2 112.83**	**0.88**	**2 293.66**
7.61	2 350	0.55	1 383.94
7.56	2 350	0.63	1 646.18
7.43	2 350	0.82	2 293.66

List of Publications

1. **A. Keilmann**, M. Godehardt, A. Moghiseh, C. Redenbach, and K. Schladitz, "Improved Anisotropic Gaussian Filters," *Image Analysis and Stereology*, vol.43, 2024.

2. H. Jäger, E. Grosjean, S. Plunder, C. Redenbach, **A. Keilmann**, B. Simeon, and C. Surulescu, "Cell seeding dynamics in a porous scaffold material designed for meniscus tissue regeneration," *PAMM*, 2024.

3. M. Duhovic, **A. Keilmann**, D. Schommer, C. Redenbach, and K. Schladitz, "Quantitative fiber orientation analysis of carbon fiber sheet molding compounds using polarization imaging and X-ray computed tomography," *Composites Part B: Engineering*, vol. 295, 2025.

4. H. Grimm-Strele, F. B. Albizuri, M. Irasarri, **A. Keilmann**, R. L. Bañobre, D. Niedziela, K. Schladitz, K. Steiner, A. de la Vauvre, V. V. Louzao, and H. Andrä, "SMC process simulation validated by image analysis," *Composites Part A: Applied Science and Manufacturing*, 2025.

5. C. Surulescu, E. Grosjean, M. Dauner, M. Doser, H. Jäger, **A. Keilmann**, C. Linti, S. C. Mohanan, G. Q. Teixeira, C. Redenbach, L. de Roy, A. M. Seitz, and B. Simeon, "An in-silico approach to meniscus tissue regeneration: Modeling, numerical simulation, and experimental analysis," *Applied Mathematical Modelling*, vol. 151, 2026.

6. **A. Keilmann**, C. Redenbach, and F. Willot, "Increasing inter-fiber contact in the Altendorf-Jeulin model," *Computational Materials Science*, vol. 264, 2026.

Academic Curriculum Vitae

Since 12/22	**PhD in Mathematics**
	RPTU Kaiserslautern-Landau, Germany
	Thesis Title: Analysis and Modeling of Fiber-based Microstructures
	Supervisor: Prof. Dr. Claudia Redenbach, Dr. Katja Schladitz
04/24–07/24	**Research Stay**
	Center for Mathematical Morphology (CMM), Mines Paris,
	PSL University, Fontainebleau, France
	Supervisor: Dr. François Willot
04/19–10/22	**M.Sc. in Mathematics**
	TU Kaiserslautern, Germany
	Thesis Title: Estimating Fiber Directions in Sheet Molding Compounds using Maximum Response of Anisotropic Gaussian Filters
	Supervisor: Dr. Katja Schladitz, Prof. Dr. Claudia Redenbach
10/14–08/18	**B.Sc. in Mathematics**
	TU Braunschweig, Germany
	Thesis Title: Discrete Least Square Reprojection Methods for the Resolution of the Gibbs Phenomenon
	Supervisor: Dr. Jan Glaubitz
07/14–04/18	**B.Sc. in Psychology**
	FernUni Hagen, Germany
	Thesis Title: Strategies and Performance in Informed and Uninformed Search
	Supervisor: PD Dr. Tobias Meilinger

Akademischer Lebenslauf

Seit 12/22	**Promotion in Mathematik** *RPTU Kaiserslautern-Landau, Deutschland* Titel: Analysis and Modeling of Fiber-based Microstructures Betreuung: Prof. Dr. Claudia Redenbach, Dr. Katja Schladitz
04/24–07/24	**Forschungsaufenthalt** *Center for Mathematical Morphology (CMM), Mines Paris, PSL University, Fontainebleau, Frankreich* Betreuung: Dr. François Willot
04/19–10/22	**M.Sc. in Mathematik** *TU Kaiserslautern, Deutschland* Titel: Estimating Fiber Directions in Sheet Molding Compounds using Maximum Response of Anisotropic Gaussian Filters Betreuung: Dr. Katja Schladitz, Prof. Dr. Claudia Redenbach
10/14–08/18	**B.Sc. in Mathematik** *TU Braunschweig, Deutschland* Titel: Discrete Least Square Reprojection Methods for the Resolution of the Gibbs Phenomenon Betreuung: Dr. Jan Glaubitz
07/14–04/18	**B.Sc. in Psychologie** *FernUni Hagen, Deutschland* Titel: Strategies and Performance in Informed and Uninformed Search Betreuung: PD Dr. Tobias Meilinger